NUMERICAL SIMULATION OF THE TATARA BRIDGE AND ITS AERODYNAMIC STABILITY OPTIMIZATION

by

Sen Wang

B.S. Engineering, China University of Geoscience (Beijing), 2013

Submitted to the Graduate Faculty of

The Swanson School of Engineering in partial fulfillment

of the requirements for the degree of

Master of Science in Civil Engineering

University of Pittsburgh

2015

UNIVERSITY OF PITTSBURGH

SWANSON SCHOOL OF ENGINEERING

This thesis was presented

by

Sen Wang

It was defended on

March 27, 2015

and approved by

Jeen-Shang Lin, ScD, Associate Professor,
Department of Civil and Environmental Engineering

Thesis Co-advisor: John Brigham, PhD, Assistant Professor,
Department of Civil and Environmental Engineering

Thesis Advisor: Qiang Yu, PhD, Assistant Professor,
Department of Civil and Environmental Engineering

NUMERICAL SIMULATION OF THE TATARA BRIDGE AND ITS AERODYNAMIC STABILITY OPTIMIZATION

Sen Wang, M.S.

University of Pittsburgh, 2015

The importance of bridge aerodynamic stability was immediately realized after the catastrophic failure of the Tacoma Narrows Bridge in 1940. Since then aerodynamic control system that using moveable flaps to increase the aerodynamic stability of bridge has been attracting increasing interests and become an important aspect in bridge aerodynamic designs. In last two decades, a significant growth in bridge span and structural complexity has been witnessed. This means that aerodynamic control system is an indispensable part for modern large-span bridge, and the active control system appears as a promising solution to improve the aerodynamic stability when bridge main span exceeds 3000 m. The purpose of this thesis is to study the effect of active aerodynamic control system with two sharp shape control devices installed on the edges of bridge decks by FEM simulation. Here, the Tatara Bridge is analyzed via FEM software ABAQUS and SOLIDWORKS. This study consists of FEM modal analysis of the bridge, wind tunnel test simulation and wind effect test modeling for the entire bridge under wind blowing from inclined directions. In the bridge modal analysis, the first 400 vibration mode shapes and their corresponding frequencies are calculated through Lanczos method solver in ABAQUS and the first order mode shape is found to be lateral bending of the deck. Therefore, the target is to optimize the deck shape to reduce the lateral aerodynamic force. To achieve this goal, 9 deck shapes are designed and tested under wind load from 15 different directions in the wind tunnel test simulation through SOLIDWORKS. The result of this test shows the optimized deck shapes

can significantly reduce the lateral aerodynamic force. Then the wind effect tests of the entire bridge before and after optimization are performed and compared in ABAQUS. As shown in the results, the displacement of midspan is decreased, especially in lateral direction. The results of this study indicate that this actively transformable sharp control surface can significantly reduce the response of the bridge under lateral aerodynamic force.

TABLE OF CONTENTS

LIST OF TABLES

LIST OF FIGURES

ACKNOWLEDGEMENTS

First, I would like to express my sincerest gratitude to my advisor Dr. Yu and co-advisor Dr. John Brigham for providing me the opportunity to do the research and supporting me throughout my graduate studies with their patience and knowledge. I could not finish my thesis without their guidance and encouragement.

I would also like to acknowledge my committee member, Dr. Jeen-Shang Lin. Thank you for your precious time and insightful advice.

Many thanks to Teng Tong, the PhD student of Dr. Yu. Thank you for helping me build the model, guiding me while I was performing the analysis and giving me suggestions.

Furthermore, I would like to extend my appreciation to Chunlin Pan, the PhD student of Dr. Yu, for helping me understanding numerical simulation and mechanical analysis.

Finally, I would like to take this opportunity to express my thanks to my parents for giving birth to me and their continuous support throughout my life.

1.0 INTRODUCTION

1.1 BACKGROUND

"Bridge" is a word that generally stands for a structure helping people cross rivers for more than one thousand years. In ancient time, the bridges, as shown in Figure 1.1 (Wikipedia 2014), were made of wood and stone, which limited the length of main span. And it is also the reason why there were so many multi-arch bridges in ancient time. At that time, the only load was induced by pedestrians and as a result, the bridge design in ancient time was based on static mechanical analysis. However, nowadays, the advanced mechanics and material science enables us to build bridges of stupendous size, both for main span and total length, which has been well witnessed in recent 2 decades. The Akashi Kaikyō Bridge built in 1998, for instance, has so far the longest main span (1991 m) in suspension bridges all over the world, as shown in Figure 1.2 (Wikipedia 2015). The Russky Bridge, as shown in Figure 1.3 (Wikipedia 2015), which was finished 3 years ago in Russia as the longest cable-stayed bridge in the world has a 1104 m long main span. And other 3 of the 4 longest cable-stayed bridges whose main spans are around 1000 m long were finished subsequently in 2008, 2009 and 2010 in China. The overall longest bridge on earth, the Danyang–Kunshan Grand Bridge, with a total length of 164,800 m completed in 2010 in China (Wikipedia 2015), shows that bridges can also be built over the sea now. As demonstrated by

these amazing bridges, the developing speed of bridges is beyond imagination and the difficulties in designing and construction process are much more challenging than any old bridges.

Figure 1.1 Ancient stone bridge

Figure 1.2 The Akashi Kaikyō Bridge

Figure 1.3 The Russky Bridge

For larger bridge size, the wind effect on the bridge becomes more obvious, especially in the high speed wind area where there are many typhoons. There have been many failures of bridges caused by aerodynamic instability, like the Tacoma Narrows Bridge which collapsed in 1940 (Billah et al 1991). Since that time, the aerodynamic analysis has become one of the indispensable mechanical analyses in designing process of bridge.

In aerodynamic analysis, determining the natural frequencies of bridge is a very important part. The first recorded bridge failure because of lacking consideration of the natural frequencies of the bridge can be traced back to 1831. On April 12th, 1831, the orderly marching steps of 74 British soldiers caused the collapse of the Broughton Suspension Bridge. In this catastrophe, the frequency of orderly marching steps coincidently matched the natural frequency of the bridge and led to the resonance of the bridge, which finally caused the collapse of the bridge. Based on this fail experience, the importance of load frequencies and natural frequencies

of structures was realized by the bridge engineers. This kind of resonance can be induced by other resources, for example, seismic load and wind load. As for the super long bridge, the wind load is a critical loading type. Thus, the relation between frequencies of wind loading and natural frequencies of structure is important to the stability of bridge. To determine the natural frequencies of structures, the modal analysis which is measuring and analyzing the dynamic response of structures during excitations is an effective method and became a primary part in design of bridge.

To improve the aerodynamic performance of bridges, the primary target is to lower the response to wind as much as possible. In general, there are two types of measures to achieve this goal, namely passive aerodynamic measures and active aerodynamic measures. As well known, the real wind is always changing in directions. Unfortunately, the wind tunnel test can only theoretically simulate the response of a bridge to the wind from one constant direction, and this might fail the bridge aerodynamic stability design under non-constant wind. To overcome this obstacle, a concept comes up using moveable surfaces to reduce wind force by selecting better shapes under different wind conditions, and based on which these two aforementioned measures are developed. The passive aerodynamic measures reduce aerodynamic force by improving the configuration of cross-section of bridge deck (Xu 2013). For instance, "Slotted deck shape", a deck with open slots in longitudinal direction of deck, improves the aerodynamic stability and prevents shedding of large vortices. The active aerodynamic measures reduce aerodynamic force by using actively controlled surfaces, as shown in Figure 1.4 (Xu 2013). The main difference between these two is that active control system needs external energy to change the shape while the passive control one does not. In fact, aerodynamic shaping and passive measures are not enough to guarantee the aerodynamic stability for a super long bridge that has a main span over

3000 m. Therefore, the only solution for such a large bridge is to build an active aerodynamic control system that can match all the requirement of any wind attacking angle, such that it can actively change shapes according to the wind conditions, which gives a good guide of aerodynamic optimization of bridge.

However, currently, the practical application of active aerodynamic control system is rare. Although it has been an attractive research topic and a lot of researches are focused on it, the tests of the optimization effect on a real bridge with active aerodynamic control system has not be accomplished yet. It is reasonable in that engineers want to know the effect of such an expensive system before it is being built on a real bridge. Therefore, to carry out the test via FEM modeling in computer as an alternative approach with satisfactorily accurate results, is worthy to try and explore.

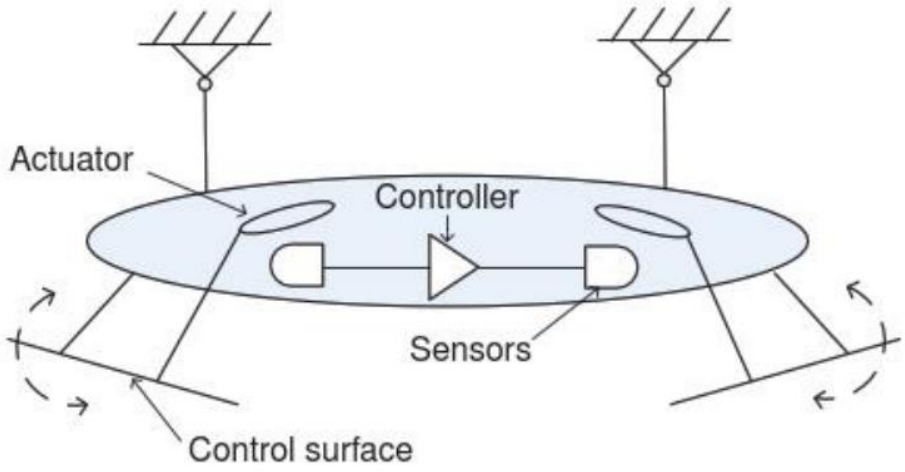

Figure 1.4 Active aerodynamic control system of bridge by Larsen (1992)

In this thesis, the Tatara Bridge was selected as a case study. The main purpose of this thesis is to explore a new active aerodynamic control design which can reduce the aerodynamic force at different wind attacking angles by changing deck shapes in theoretical field, and

therefore enrich the theory of active aerodynamic control system. Additionally, this study will also try to summarize the relationship between the aerodynamic force of different deck shapes and wind attacking angles. In general, this study includes modal analysis leading to the lowest order vibration mode of the bridge and its corresponding frequency, and a series of wind tunnel test simulations designed to find the aerodynamic force of different deck cross-section shapes under different wind conditions. The theoretical background, process, results and related discussions will be introduced in later chapters following a brief literature review about this topic.

1.2 LITERATURE REVIEW

1.2.1 Modal analysis

The modern modal analysis can be traced back in 1960s. At that time, the experimental test is the only method of modal analysis. This situation has been changed with the invention of some powerful numerical tools, such as finite element method. Later both the experimental and theoretical modal analysis has gained large development with the four innovations in late 1970s, namely manufactures of digital signal analyzers, extremely powerful desktop computers, Structural Measurement Systems of San Jose and "FESDEC" the first commercially available finite element analysis program (Ramsey 1983). These achievements provide the users an access to a full complement of experimental and theoretical analysis tools. Examples of the application of both approaches on bridges are listed below.

In 1994, a research about modal analysis of an arch bridge was published by Deger et al (1994). In this research, a servohyraulic vibration generator was used to excite the bridge and the

three-axial acceleration measurement devices were placed on 144 points of the bridge in three dimensions to measure the response of the bridge. Meanwhile, a finite element model which consisted of 300 CQUAD4 quadrilateral plate elements was built to roughly estimate a few eigen-frequencies of the bridge. The comparison of the results between real experiment and finite element model showed that the finite element models were able to reproduce the measured frequencies and vibration shapes with satisfactory accuracy.

In the same year, a research about modal analysis of a highway bridge was presented by Deger et al (1995). The method used in this research is same as the method mentioned before, involving both experimental and finite element approaches. In this experimental test, the results were measured at 94 points in three directions of a bridge. In finite element analysis, the model consisted of 1000 CQUAD4 quadrilateral plate elements and 29 CBEAM beam elements. The comparison showed that such a finite element model consisted of approximately 1000 elements was able to capture the eigen-frequencies and corresponding mode shapes.

Later, Clemente et al. (1998) published a research about experimental modal analysis of the Garigliano cable-stayed bridge. In this research, authors gained the preliminary idea of dynamic response of the bridge and the selection of optimum sensor locations through the initial theoretical analysis via finite element model. After the experimental test was finished, they upgraded the finite element model and used this new model to analyze the vibration of the bridge. Some good matches of the results from both approaches were found. For instance, as for the first order mode, the experimental frequency was 0.9 and FEM frequency was 0.87. For the second order mode, the experimental frequency was 1.30 and FEM frequency was 1.33. And similar results were shown in other modes. Thus, the authors concluded that the numerical model

was also useful in structural analyses under service loads. Some similar results were found by some other researchers later (Cunha et al 2001 and Ren 2004).

In 2012, Wang et al (2012) published a research about comparative study on buffeting performance of Suton Bridge. Based on design and measured spectrum, the FEM model of the bridge was established on the ANSYS platform. For FEM model, the 3D beam element (Beam4) was used for the girder, transverse diaphragms, towers, and piers, and 3D tension-only truss element (Link10) was used for stay cables. Meanwhile, the nonlinearity of the stayed-cable stiffness was approximated by the linearized stiffness using the Emst equation of equivalent modulus of elasticity (Emst 1965). The soil-structure interaction was not considered in this study. The First 200 natural frequencies and vibration modes of the Sutong Bridge were calculated by the subspace method solver of ANSYS. Some typical vibration frequencies and corresponding vibration shapes were list. From these results, the author concluded that the lateral bending appeared earlier than the vertical bending and the sixteenth mode was an important mode which was closely related to the flutter instability. Moreover, the contribution of the 1st order mode response was not always the largest and the transverse buffeting vibrations of towers were dominated by their lateral bending. There are some similar studies presented (Xu et al 1997, Zhang et al 2011 and Wei et al 2012).

1.2.2 Wind tunnel test and CFD simulation

CFD stands for computational fluid dynamics which uses numerical methods to solve the fluid flow problems. Recently, with the advance of computer technology, the CFD simulation became a powerful tool in aerodynamic shape designs. Nowadays, the real wind tunnel test was less popular than before, since it always cost large space and a lot of labor work when compared with

the CFD simulation method. Therefore, to involve the CFD simulation method in a virtual wind tunnel test has been attracted significant attentions. Of course, the accuracy of the CFD simulation has to be evaluated by comparison with experimental data. Here are some aerodynamic designing examples using both CFD simulation method and experimental method.

In 2006, a research about computational fluid dynamics simulation and wind tunnel testing on microlight model was published by Ishak et al. (2006). The objective of this research is to determine the aerodynamic characteristics of a microlight. In the determining process, the author used experimental test and CFD simulation. In the CFD simulation, the SOLIDWORKS software package was used in microlight modeling and half solid model was used in simulation test, as shown in Figure 1.5 (Ishak 2006). As for the experimental wind tunnel test, it used a real 1:25 scaled-down model of single-seated microlight. Like normal wind tunnel test, the result of test must be corrected, which consists of solid blockage and wake blockage. It is showed in Figure 1.6 that lift coefficient and drag coefficient from experiment test and CFD simulation are almost overlapped. Therefore, the author concluded that both methods are usable and agreeable with each other.

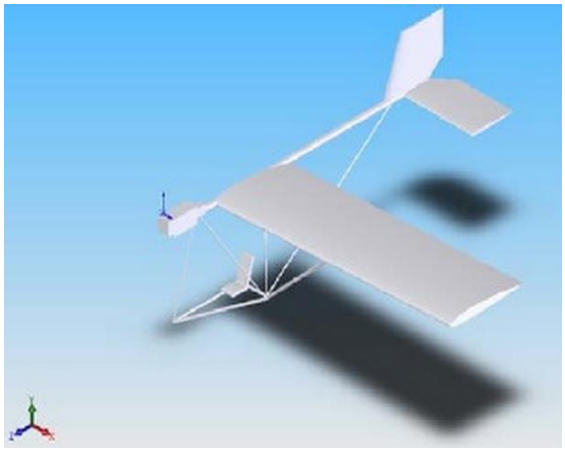

Figure 1.5 The half of solid model by Ishak (2006)

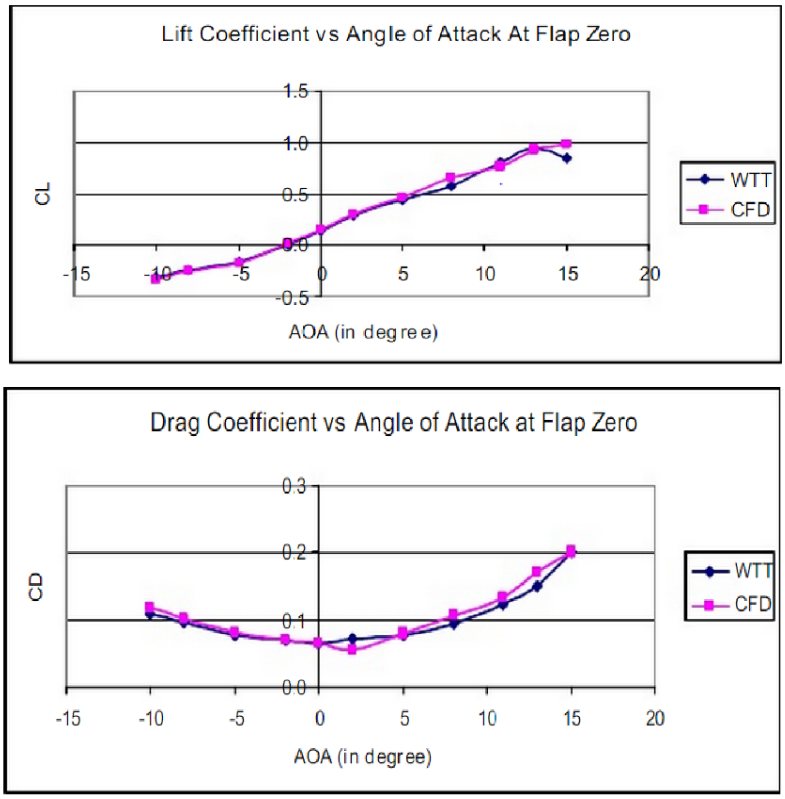

Figure 1.6 Comparison of CFD and experimental test by Ishak (2006)

In the same year, Ciobaca et al. (2006) published a research about a CFD process chain for simulating open wind tunnel test sections. In this process, the DNW-NWB wind tunnel, as shown in Figure 1.7, and AWB wind tunnel, as shown in Figure 1.8, were used as experimental verification of CFD simulation. This verification showed a very good result as expected, which indicated that the CFD simulation is able to virtually realize the wind tunnel testing in open test sections, as a reliable simulation method for aerodynamic designs.

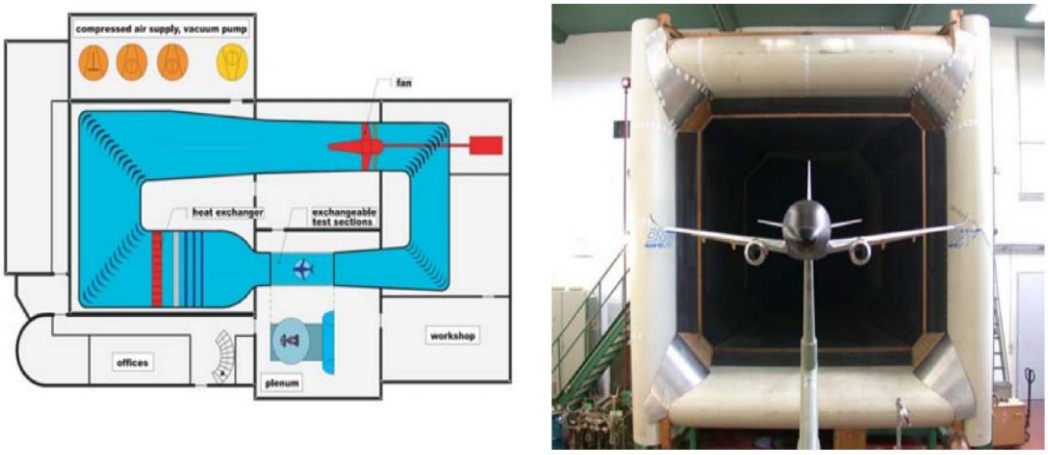

Figure 1.7 DNW-NWB wind tunnel (Ciobaca et al 2006)

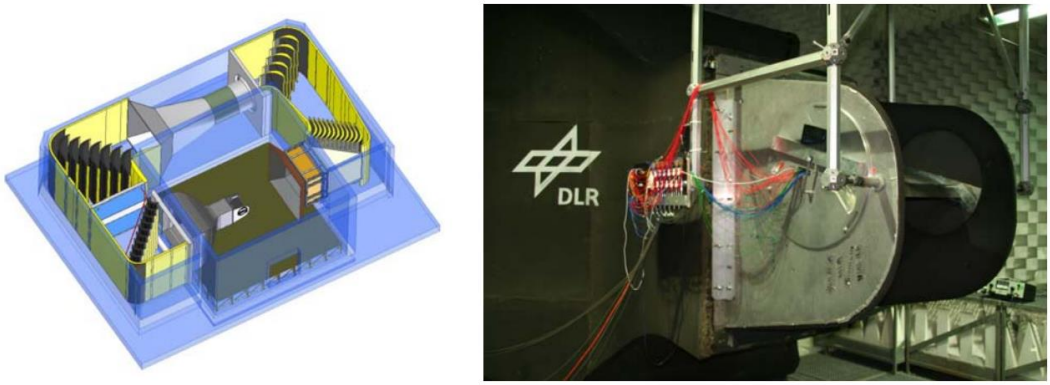

Figure 1.8 AWB wind tunnel (Ciobaca et al 2006)

1.2.3 Aerodynamic optimization

Since the collapse of the Tacoma Narrows Bridge, the aerodynamic optimization has been attracting more and more attentions. Many concepts and methods of optimization were presented for this topic, including some classical ones which have significant influence on the development of aerodynamic optimization in history.

In 1988, Nobuto et al. (1988) published a research about control of flutter by tuned mass damper (TMD). In this research, the author used two TMDs placed on the leading and trailing edges of the deck to change the flutter frequency of bridge, which improved the flutter wind speed by 14%. And in 1992, Branceleoni et al. (1992) presented a new idea that using tanks filled with water on the bridge deck to modify the gravity center of bridge, which was successfully used in the Humber Bridge. Many similar TMD control methods on bridges can be found (Gu et al 2001, Datta et al 2002 and Kwon et al 2007).

The first reported research on active control system was addressed by Kobayashi and Nagaoka et al. (1992). The authors designed a new deck cross-section with the control surfaces located above the deck and tested it in the wind tunnel. From this experiment, the authors found an increase of flutter wind speed of factor 2. In this design, the control algorithm was proportional to the rotation of deck itself.

In the same year, Ostenfeld and Larsen et al. (1992) presented a design of two concepts of active control methods, as shown in Figure 1.9. The first design reduced the wind-induced excitation by changing the geometry of the deck side which leads to the modification of flow pattern around the deck. The second design is to add a deck with additional active control surfaces attached on the bottom of both sides. In this design, the aerodynamic stability was improved by rotating control surfaces to produce aerodynamic force for restraining the motion of deck. This design did not modify the original structural properties of the bridge itself.

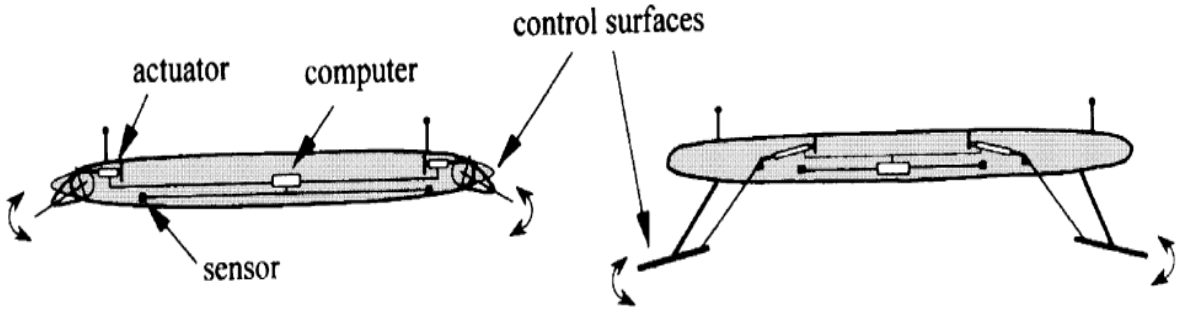

Figure 1.9 Active control methods by Ostenfeld and Larsen (1992)

6 years later, Kobayashi et al. (1998) published a study about experiment and theory of aerodynamic control through additional flaps attached directly to the edges of deck. The experimental results of trailing flap active control system in which the amplitude and phase of the flap were given with respect to the motion of deck showed a great agreement with theoretical predictions based on the Theodorsen Function.

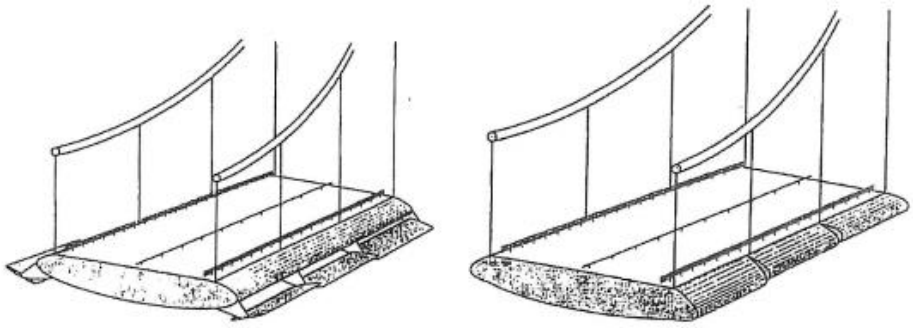

Figure 1.10 Active control methods by Hansen and Palle (1998)

Also in 1998, Hansen and Palle et al. (1998) presented a research about active control of long bridge using flaps. Two types of actively controlled flaps were described in this study, as shown in Figure 1.10. Authors tested these two models in wind tunnel and concluded that the flaps control system was a very effective optimization method in control vibration of deck, and the flaps installed as integrated parts on the trailing and leading edges worked better than the

other type. The experimental results also confirmed that the trailing flaps are more efficient than the leading flaps. Additionally, the control of both trailing and leading flaps is a more efficient way, compared to the one flap control method. However, since the separation of the flow around the deck was not taken into account, the effect of trailing flap might be overestimated. Some similar studies can be found (Thoft-Christensen 2000, Wilde el at 2001 and Huynh et al 2001) and a general introduction of recent research, developments and practice of vibration, control and monitoring of long-span bridges in Japan was published by Fujino (2002).

1.3 STUDY PLAN

To simulate a super long span bridge such as the Tatara Bridge, making a full size model in experimental tests is unrealistic. To scale it to a smaller size can be easier, however sometimes ignore some critical properties of the bridge due to size effect and some other reasons. Therefore, to use computer simulation has been realized as an indispensable approach.

Computer simulation is an attempt to model a real-life or hypothetical situation in a computer so that it can be studied to see how the system works under various conditions. The prediction may be made about the behavior of system influenced by changing the system parameters in the simulation. It is a powerful tool to virtually investigate the behavior of the system and greatly reduce the time and labor.

In this study, the Tatara Bridge is first discretized by finite elements in computer to find the dynamic properties of bridge structure through modal analysis introduced in this chapter. After that, the active control surfaces are used to optimize the aerodynamic stability.

The outline of the thesis is organized as follows.

Chapter 2 describes the process of FEM modal analysis of the Tatara Bridge and results.

Chapter 3 introduces the CFD simulative wind tunnel tests of various deck shapes and corresponding results.

Chapter 4 shows the optimization process of the bridge and its effect.

Chapter 5 presents the summaries and recommendations of this study.

2.0 FEM MODAL ANALYSIS OF THE TATARA BRIDGE

2.1 BASIC INFORMATION OF THE TATARA BRIDGE

First, the basic information about the Tatara Bridge is introduced here. The Tatara Bridge currently has the fifth longest main span in cable-stayed bridges all over the world. The bridge is located around the mid-point of the Nishi-Seto Expressway, as shown in Figure 2.1, in Japan, one of the most geologically active and typhoon-prevalent areas on earth. This bridge, completed and opened to the public on May 1, 1999, connects Ikuchijima Island on the Hiroshima prefecture side to Omishima Island on the Ehime prefecture side, as shown in Figure 2.2. The Tatara Bridge crosses a narrow strait which is 1.3 km wide and links the Mt. Kannon (on the southwestern tip of Ikuchishima Island in Hiroshima Prefecture) with Cape Tatara (on Omishima Island in Ehime Prefecture).

The structure of the Tatara Bridge can be introduced in parts as girder, cables, towers and foundations. Since soil-structure interaction is not considered in this research, the foundation part will not be introduced. The general dimension of the bridge is shown in Figure 2.3.

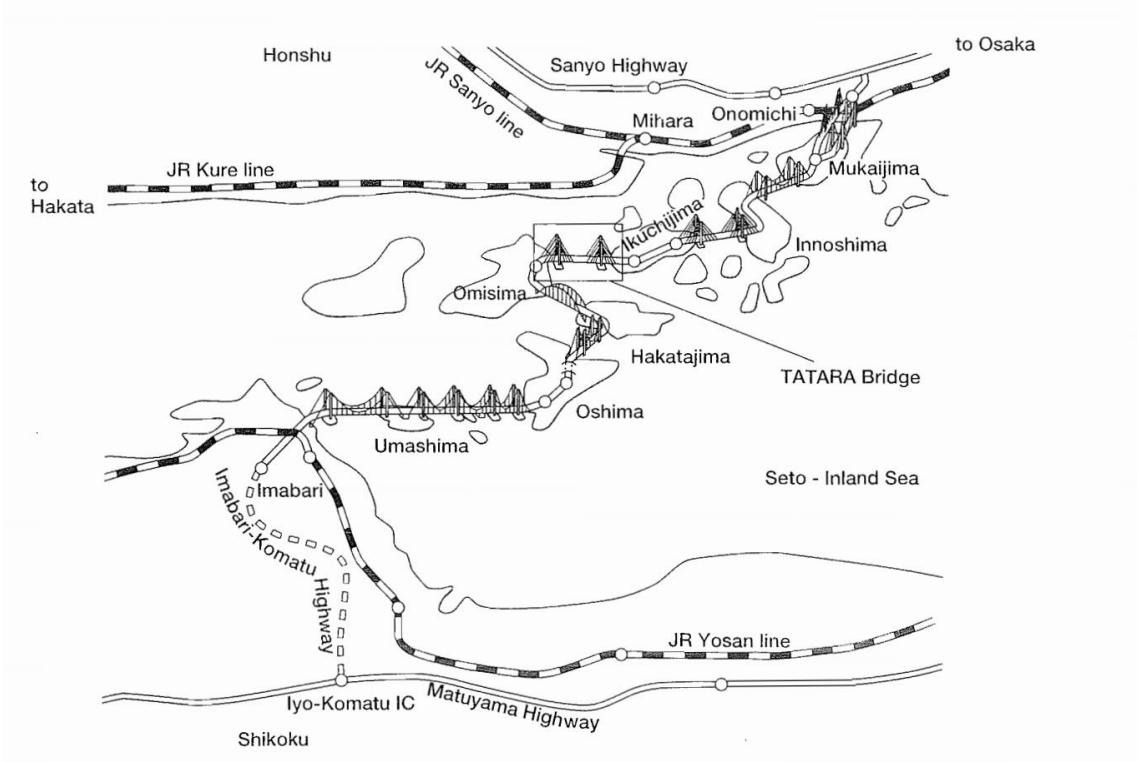

Figure 2.1 Nishi-Seto Expressway (Authority 1999)

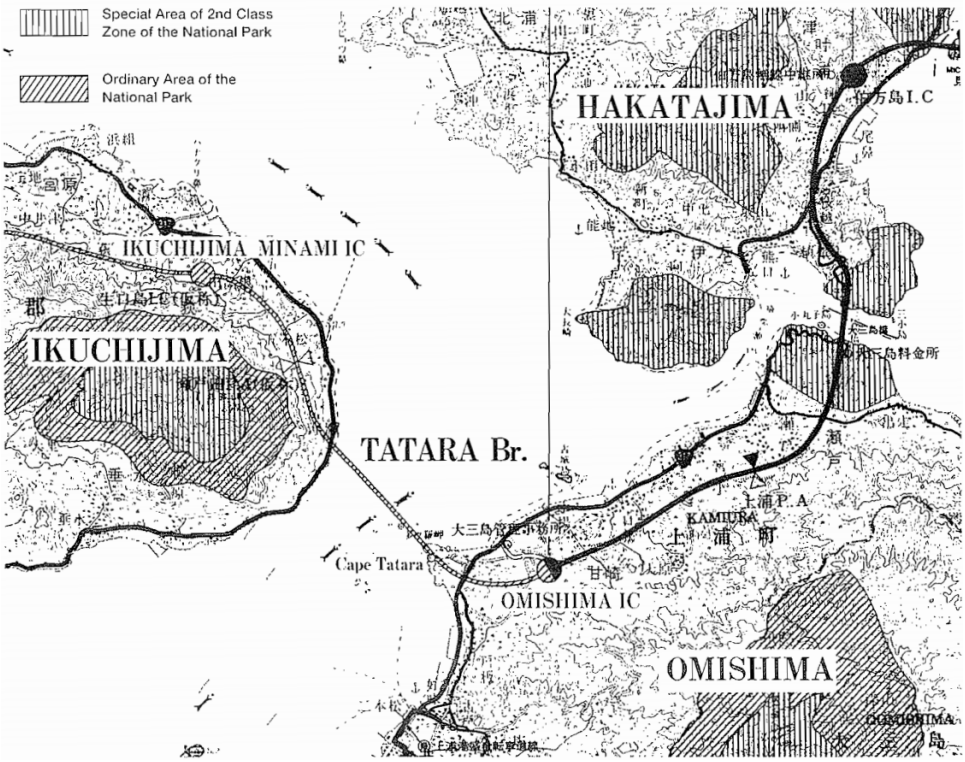

Figure 2.2 Location of the Tatara Bridge on the map (Authority 1999)

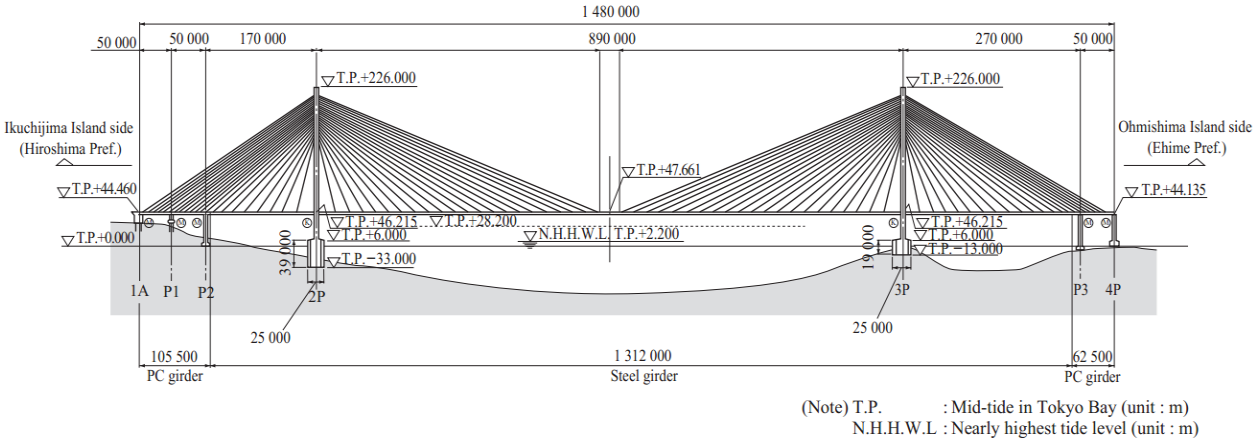

Figure 2.3 General dimensions of the Tatara Bridge (Yabuno 2003)

The main girder has a total length of 1480 m, which contain 3 separated spans, 270 m, 890m, and 320m respectively. It is 30.6 m wide, including the roads of bicycles and sidewalk, and 2.7 m thick. The cross-section profiles are shown in Figure 2.4. This girder is structured by hybrid PC-Steel girders. PC girders are installed at each end of both side span sections as a counterweight to resist negative reaction, with the length of 105.5 m and 62.5 m respectively. The flat 3-cell box girders attached with fairings was used in the midspan of the bridge.

The main tower of the Tatara Bridge is 220 m high and designed as an inverted Y shape, as shown in Figure 2.5. The cross-section of the main tower is cross-shaped section with corners cut for high speed wind stability (see Figure 2.6).

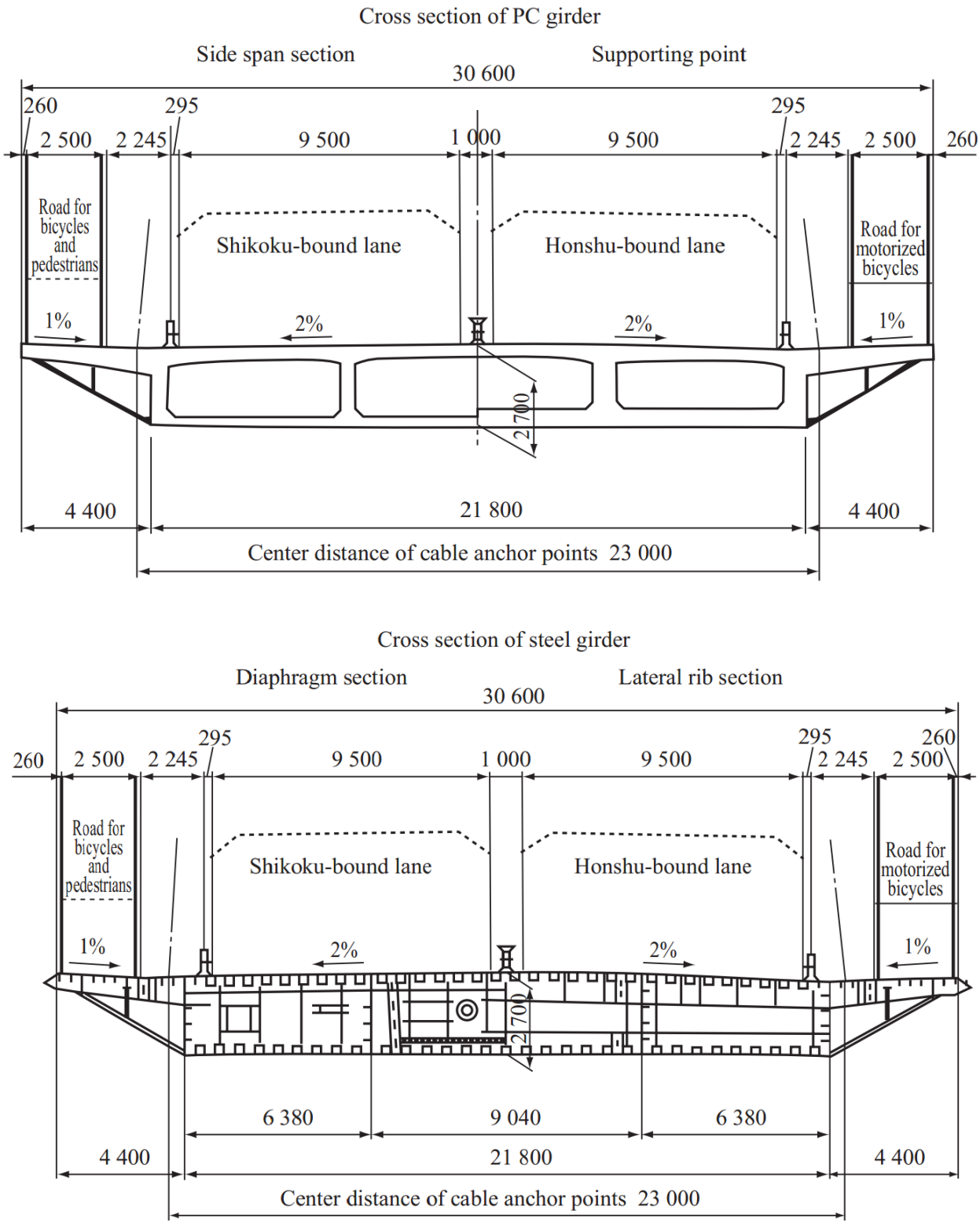

Figure 2.4 Cross-section of girders (main girder section) (unit: mm) (Yabuno 2003)

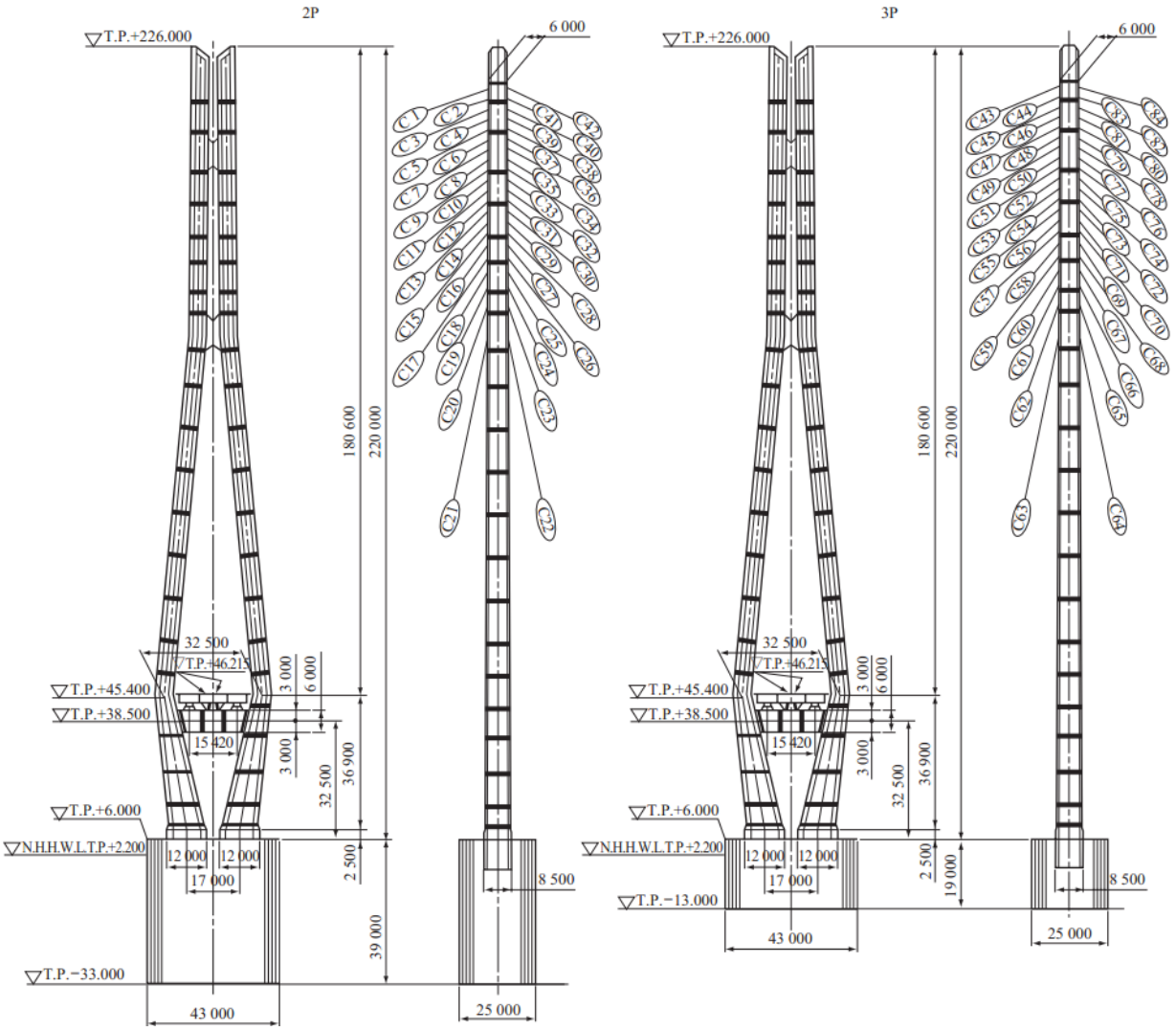

Figure 2.5 General dimension of main tower (Yabuno 2003)

The cable system contains 168 two-plane multi-fan cables connecting the towers and girders. The maximum cable length is about 460 m. The section properties of cables are shown in Table 2.1. The cables have to be fixed to rigid structures on the side spans so as to balance the weight of center span girder. There are two methods of doing this: cables fixed to the side-span girder and cables fixed to a separate structure such as an abutment. For the Tatara Bridge, the side-span cables are directly fixed to the side span girders, not separate structures. The surface of

cables are indented (see Figure 2.7), where the polyethylene cable coating is used to lower vibration induced by wind and rain.

Generally, the whole bridge is not freely supported. The elastic joint bearings in longitudinal direction are adopted and installed at the joints of towers and girder (see Figure 2.5). The theoretical background of the simulation of this bridge is explained in next section.

Table 2.1 Section properties of cables

Cable number		Outside diameter (mm)	Sectional area (mm^2)	Cable number		Outside diameter (mm)	Sectional area (mm^2)
Center span	43	169	14600	Side span	64	115	6270
	44	161	13000		65	115	6270
	45	155	12000		66	115	6270
	46	151	11400		67	115	6270
	47	149	10900		68	120	6270
	48	149	10900		69	120	6270
	49	147	10200		70	135	8580
	50	147	10200		71	135	8580
	51	147	10200		72	135	8580
	52	147	10200		73	135	8580
	53	139	9270		74	135	8580
	54	136	8580		75	145	10200
	55	136	8580		76	150	10900
	56	136	8580		77	150	10900
	57	119	7200		78	150	10900
	58	119	7200		79	150	10900
	59	119	7200		80	150	11400
	60	113	6270		81	155	12000
	61	113	6270		82	160	13000
	62	113	6270		83	165	13400
	63	108	5810		84	170	14600

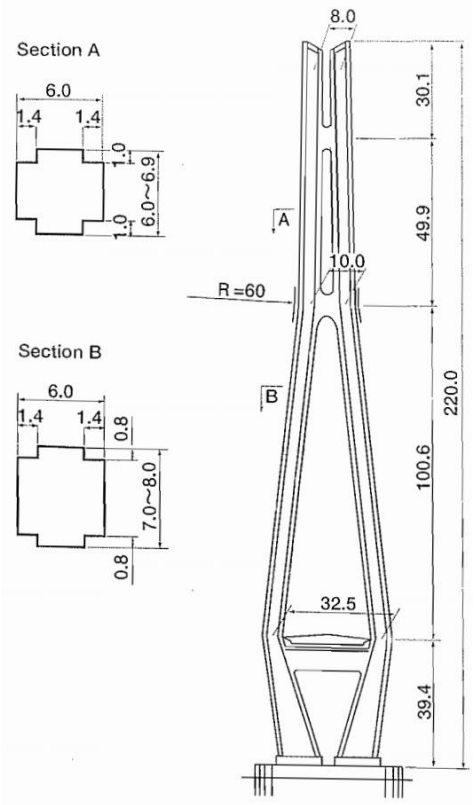

Figure 2.6 Section profile of main tower (Authority 1999)

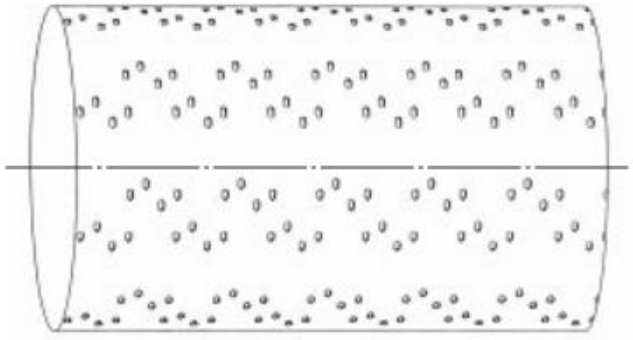

Figure 2.7 Indent of cable surface (Yabuno 2003)

2.2 THE THEORY USED IN SIMULATION OF THE TATARA BRIDGE

"Analytical descriptions of physical phenomena and processes are called mathematical models (Bratley 1983)." It is true that most of physical phenomena and processes can be represented by mathematic equations which capture their key characteristics. The governing equations represent the physical laws or principles like conservation of mass and energy. Theoretically, the solution of the equations will provide the knowledge of theses physical phenomena and enable the prediction of them. FEM, as one of the most important numerical tools to solve the equations, is therefore adopted in this study for modal analysis and aerodynamics simulation.

2.2.1 Finite element method

Generally speaking, the finite element method is a numerical method designed for boundary value problems. It uses interpolation functions to approximate the field functions on the domain, which is described in a weak form of the governing partial differential equations. In the finite element method, the given domain is always treated as a collection of several subdomains and the approximation of the field functions is realized piecewisely by a complete function group, for example Lagrange-type-interpolation polynomials. This approximation will convert the differential equations to algebraic ones, and the solution is guaranteed to converge to the real solution with the increasing of DOFs.

The main steps of finite element method are:

(1) Discretization of model (Mesh)

The entire model is separated into several elements consist of nodes (see Figure 2.9).

(2) Evaluating the stiffness matrix of each element described by shape functions, via numerical integration.

(3) Assembly of all element stiffness matrices, nodal loading vectors to form the global equilibrium equations.

(4) Importing boundary conditions and solving the algebraic equations.

(5) Determining the interpolated unknown fields, stress and strain of the elements of interest.

In the finite element analysis, the overall discrete model (meshed model), like the middle picture in Figure 2.8, is always called finite element model, which consists of finite number of elements and therefore has finite number of DOFs (degree-of-freedom).

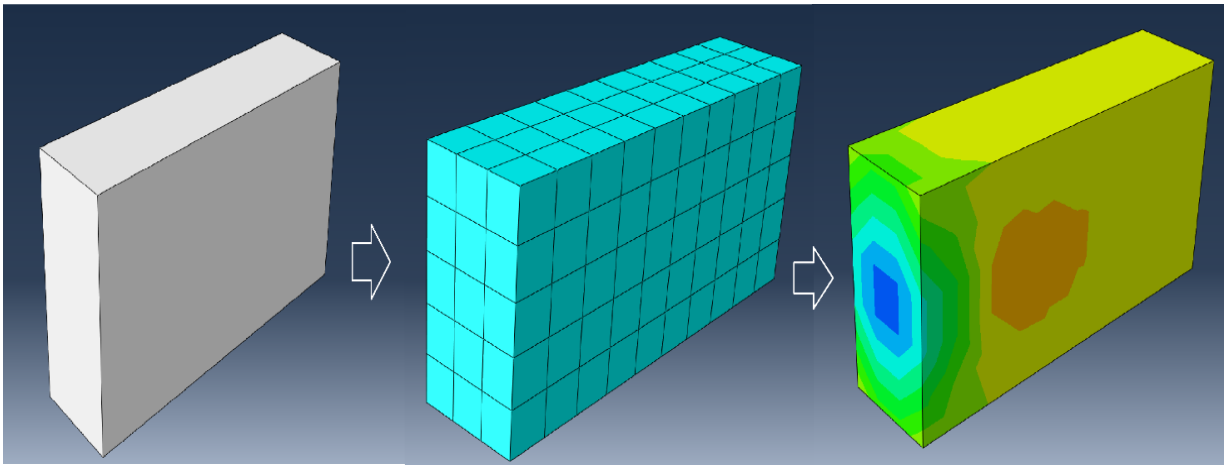

Figure 2.8 Process of finite element method

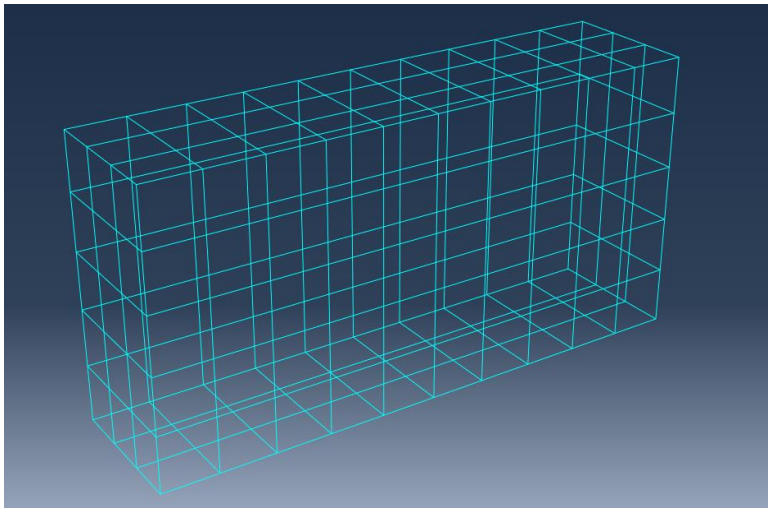

Figure 2.9 Example of mesh

2.2.2 Theory of modal analysis

Generally, the modal analysis is the analysis of dynamic response of the structure to vibrational excitation (Reddy 2010). It will lead to the natural mode shapes and the frequencies of structure during free vibration. As discussed above, the experimental modal analysis is prohibitively expensive due to the limit of equipment and space. Thus in this thesis, the modal analysis is performed by numerical simulation, namely finite element analysis. During FEA, the unknown terms in the governing equations of motion are eigenvalues and corresponding eigenvectors, with the physical meaning as the natural frequencies and corresponding modes of vibration. Since the magnitude of structure's vibration will markedly increase when the stimulating frequency reaches the first order natural frequency, which is realized very dangerous for structure's safety, the mode corresponding to the first order natural frequency is the desired result which is easier to be stimulated than the other higher frequency modes.

2.2.2.1 Analysis of free vibration frequencies

The generalized equation of motion is

$$\mathbf{m}\ddot{\mathbf{u}} + \mathbf{c}\dot{\mathbf{u}} + \mathbf{k}\mathbf{u} = \mathbf{F} \tag{2.1}$$

in which $\mathbf{m}$ is mass matrix, $\mathbf{u}$ is the displacement, $\dot{\mathbf{u}}$ is the first derivative of displacement, $\ddot{\mathbf{u}}$ is the second derivative of displacement, $\mathbf{c}$ is the damping matrix, $\mathbf{F}$ is the force vector.

The general equation of motion under zero damping free vibration condition can be expressed as:

$$\mathbf{m}\ddot{\mathbf{u}} + \mathbf{k}\mathbf{u} = \mathbf{0} \tag{2.2}$$

In this equation, $\mathbf{0}$ stands for zero vector.

The expression of displacement can be written as:

$$\mathbf{u}(t) = \hat{\mathbf{u}}\sin(\omega t + \theta) \tag{2.3}$$

In this expression, $\hat{\mathbf{u}}$ represents the shape of system and θ is a phase angle.

Thus, the second derivative of displacement is:

$$\ddot{\mathbf{u}}(t) = -\omega^2\hat{\mathbf{u}}\sin(\omega t + \theta) = -\omega^2\mathbf{u} \tag{2.4}$$

Substitute equation 2.3 and 2.4 in to equation 2.2, get:

$$-\omega^2\mathbf{m}\hat{\mathbf{u}}\sin(\omega t + \theta) + \mathbf{k}\hat{\mathbf{u}}\sin(\omega t + \theta) = \mathbf{0} \tag{2.5}$$

Since the sine term is arbitrary, the equation 2.5 becomes:

$$\left[\mathbf{k} - \omega^2\mathbf{m}\right]\hat{\mathbf{u}} = \mathbf{0} \tag{2.6}$$

By Cramer's rule, the equation above can be written as:

$$\hat{\mathbf{u}} = \frac{\mathbf{0}}{\left\|\mathbf{k} - \omega^2\mathbf{m}\right\|} \tag{2.7}$$

Thus, the only condition for a nontrivial solution of equation 2.7 is

$$\left\|\mathbf{k} - \omega^2\mathbf{m}\right\| = 0 \tag{2.8}$$

Equation 2.8 is the frequency equation of the system. The N roots of ω^2 is the frequencies of N modes. And the frequency vector $\boldsymbol{\omega}$ can be written like:

$$\boldsymbol{\omega} = \begin{bmatrix} \omega_1 \\ \omega_2 \\ \vdots \\ \omega_N \end{bmatrix}$$

2.2.2.2 Analysis of free vibration mode shapes

After get the frequencies of vibration, the equation of motion can be expressed as:

$$\tilde{\mathbf{E}}^{(n)}\hat{\mathbf{u}}_{\mathbf{n}} = \mathbf{0} \tag{2.9}$$

In equation 2.9, the $\tilde{\mathbf{E}}^{(n)}$ is defined as

$$\tilde{\mathbf{E}}^{(n)} = \mathbf{k} - \omega^2\mathbf{m} \tag{2.10}$$

in which, *n* stands for the number of a mode.

Since the natural frequencies are evaluated from equation 2.8, this equation is satisfied identically, leaving the amplitude of vibration is undetermined. Concerning the shape of vibration, the assumption that the displacement vector of first element has a unit amplitude is made (Clough 1975). The displacement matrix can be expressed as:

$$\begin{bmatrix} \hat{u}_{1n} \\ \hat{u}_{2n} \\ \hat{u}_{3n} \\ \vdots \\ \hat{u}_{Nn} \end{bmatrix} = \begin{bmatrix} 1 \\ \hat{u}_{2n} \\ \hat{u}_{3n} \\ \vdots \\ \hat{u}_{Nn} \end{bmatrix} \tag{2.11}$$

The equation 2.9 can be written as expanded form,

$$\begin{bmatrix} e_{11}^{(n)} & e_{12}^{(n)} & \cdots & e_{1N}^{(n)} \\ e_{21}^{(n)} & e_{22}^{(n)} & \cdots & e_{2N}^{(n)} \\ \vdots & \vdots & \ddots & \vdots \\ e_{N1}^{(n)} & e_{N2}^{(n)} & \cdots & e_{NN}^{(n)} \end{bmatrix} \begin{bmatrix} 1 \\ \hat{u}_{2n} \\ \vdots \\ \hat{u}_{Nn} \end{bmatrix} = \begin{bmatrix} 0 \\ 0 \\ 0 \\ 0 \end{bmatrix} \tag{2.12}$$

In this expended form, $e_{NN}^{(n)}$ stands for the component of $\tilde{\mathbf{E}}^{(n)}$ in Nth row and Nth column.

For convenience, equation 2.12 can be expressed symbolically as

$$\begin{bmatrix} e_{11}^{(n)} & \tilde{\mathbf{E}}_{10}^{(n)} \\ \tilde{\mathbf{E}}_{01}^{(n)} & \tilde{\mathbf{E}}_{00}^{(n)} \end{bmatrix} \begin{bmatrix} 1 \\ \hat{\mathbf{u}}_{0n} \end{bmatrix} = \begin{bmatrix} 0 \\ \mathbf{0} \end{bmatrix} \tag{2.13}$$

Here,

$$\tilde{\mathbf{E}}_{01}^{(n)} = \begin{bmatrix} e_{22}^{(n)} & e_{23}^{(n)} & \cdots & e_{2N}^{(n)} \\ e_{32}^{(n)} & e_{33}^{(n)} & \cdots & e_{3N}^{(n)} \\ \vdots & \vdots & \ddots & \vdots \\ e_{N2}^{(n)} & e_{N3}^{(n)} & \cdots & e_{NN}^{(n)} \end{bmatrix} \tag{2.14}$$

$$\tilde{\mathbf{E}}_{10}^{(n)} = \begin{bmatrix} e_{12}^{(n)} & e_{13}^{(n)} & \cdots & e_{1N}^{(n)} \end{bmatrix} \tag{2.15}$$

$$\tilde{\mathbf{E}}_{01}^{(n)} = \begin{bmatrix} e_{21}^{(n)} \\ e_{31}^{(n)} \\ \vdots \\ e_{N1}^{(n)} \end{bmatrix} \tag{2.16}$$

$$\hat{\mathbf{u}}_{0n} = \begin{bmatrix} \hat{u}_{2n} \\ \hat{u}_{3n} \\ \vdots \\ \hat{u}_{Nn} \end{bmatrix} \tag{2.16}$$

Then,

$$\tilde{\mathbf{E}}_{01}^{(n)} + \tilde{\mathbf{E}}_{00}^{(n)} \hat{\mathbf{u}}_{0n} = \mathbf{0} \tag{2.17}$$

$$e_{11}^{(n)} + \tilde{\mathbf{E}}_{10}^{(n)} \hat{\mathbf{u}}_{0n} = 0 \tag{2.18}$$

The equation 2.17 can be rearranged as

$$\hat{\mathbf{u}}_{0n} = -\tilde{\mathbf{E}}_{01}^{(n)} (\tilde{\mathbf{E}}_{00}^{(n)})^{-1} \tag{2.19}$$

Thus, the displacement amplitudes can be achieved. And the displacement vectors associated with n^{th} mode of vibration consist of displacement amplitude and the unit amplitude of 1st component. After expressed vector in dimensionless form, the result is the n^{th} mode shape $\mathbf{f}_n$.

$$\mathbf{f}_n = \begin{bmatrix} \phi_{1n} \\ \phi_{2n} \\ \phi_{3n} \\ \vdots \\ \phi_{Nn} \end{bmatrix} \equiv \frac{1}{\hat{u}_{kn}} \begin{bmatrix} 1 \\ \hat{u}_{2n} \\ \hat{u}_{3n} \\ \vdots \\ \hat{u}_{Nn} \end{bmatrix} \tag{2.20}$$

And $\hat{u}_{kn}$ is the reference component which is always largest displacement.

2.3 BRIDGE MODELING

In this section, the details are introduced about finite element modeling of this bridge in general purpose software. The software used in this study is ABAQUS which is a very powerful general purpose software and used by thousands engineers from different types of professions. The product suite of ABAQUS is consists of five main products:

(1) Abaqus/CAE, which is used in modeling and mechanical problems.

(2) Abaqus/Standard, which is a general FEM analyzer using implicit integration scheme.

(3) Abaqus/Explicit, which is a special FEM analyzer using explicit integration scheme.

(4) Abaqus/CFD, which is used in fluid dynamics.

(5) Abaqus/Electromagnetic, which is used in electromagnetic problems.

The global coordinate system was set in ABAQUS, as shown in Figure 2.10, with the X-axis along the bridge length, Y-axis in the lateral direction and Z-axis in the vertical direction.

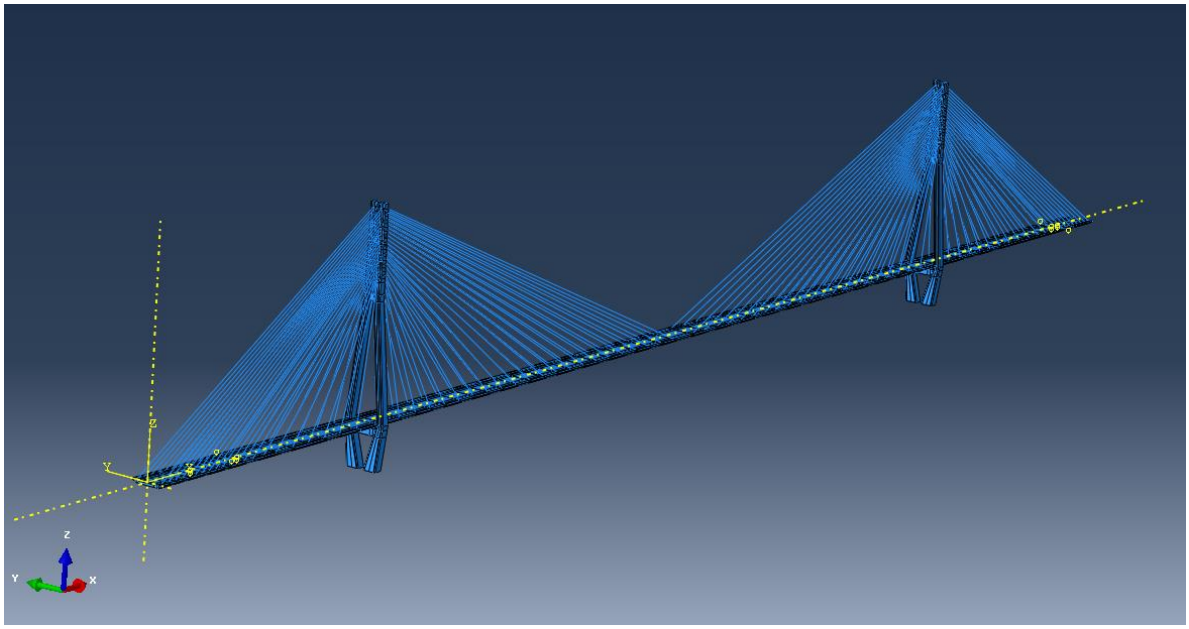

Figure 2.10 Global coordinate system of the bridge model

Based on the basic information of the Tatara Bridge, the bridge is modeled using continuum and truss elements. All the parts of the bridge except the cables are modeled with continuum element C3D8, a 3 dimensional 8-node linear brick element, as shown in Figure 2.11. The cables are modeled by truss element T3D2, a 3 dimensional 2-node structure element. Unlike the beam elements, the T3D2 truss element can only stand axial loading, which makes it perfect for modeling the cables always under tension in the bridge. In real bridge, the cables are fixed to the girder and main towers on the bridge. To capture the real connecting situation, in the finite element model, the tress elements are coupled with C3D8 elements used for modeling girder and towers. It means the truss elements and C3D8 elements share the same nodes at connecting spots (Figure 2.12).

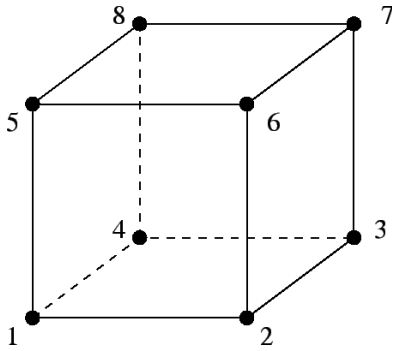

Figure 2.11 8-node brick element

In this study, the real complicated structure of the bridge is simplified to save computational cost without loss of key characteristics. In girder part, the box girder is replaced by a solid girder with the same external shape in the FE model. Similarly, the main towers, are approximated by solid ones. The elastic joints connecting girder and towers are simplified as two bricks at the same locations. In this case, the number of total DOFs in simulation is greatly reduced, which saves a lot of computational cost.

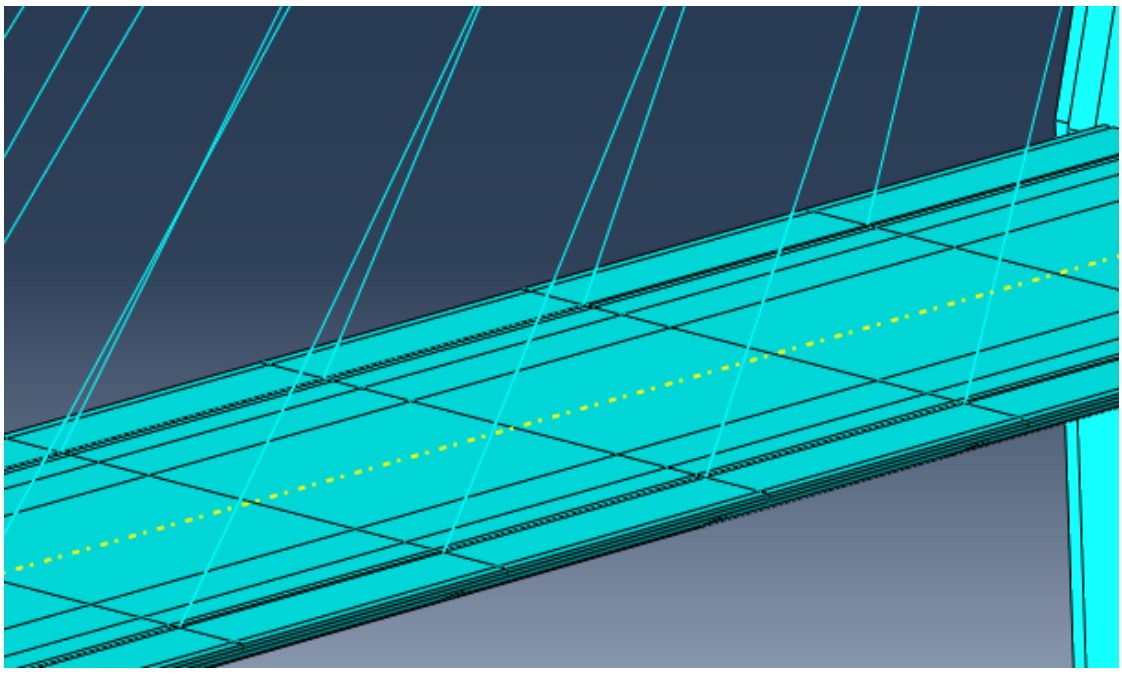

Figure 2.12 Cable coupled with girder

However, to guarantee the approximation is acceptable, the equivalent material properties have to be reassigned to the FE model, due to the slight modification of the geometry of the structural members. The equivalent criteria for the key parameters, namely Young's modulus, Poisson's ratio and density, are listed in the following equations (Note, the subscript 1 stands for the original deck and subscript 2 stands for the simplified deck.):

Mass equivalent

$$\rho_1 V_1 = \rho_2 V_2 \tag{2.21}$$

in which, ρ is the density of material and V is the volume of material.

Bending stiffness equivalent

$$E_1 I_1 = E_2 I_2 \tag{2.22}$$

Here, E stands for the Young's modulus and I is the moment of inertial.

Shear stiffness equivalent

$$G_1 A_1 = G_2 A_2 \tag{2.23}$$

in which

$$G = \frac{E}{2(1+\nu)} \tag{2.24}$$

G is the shear modulus, ν is Poisson's ratios and A is the section area.

Based on these principles, the equivalent parameters can be expressed as:

$$\rho_2 = \frac{\rho_1 V_1}{V_2} = \frac{\rho_1 A_1}{A_2} \tag{2.25}$$

$$E_2 = \frac{E_1 I_1}{I_2} \tag{2.26}$$

$$\nu_2 = \frac{E_2 A_2}{E_1 A_1}(1+\nu_1) - 1 \tag{2.27}$$

The initial boundary conditions are defined at the locations of piers and bottom of main towers. The displacement at bottom of main towers is set to be fixed, as shown in Figure 2.13,

and the connected positions between girder and piers of side-span is defined as fixed (U1=U2=U3 =0), as shown in Figure 2.14. Both ends of the girder are set as fixed.

After the finite element discretization is completed, the Lanczos method solver is selected to calculate the eigenvalues and corresponding eigenvectors. The results are depicted in the following section.

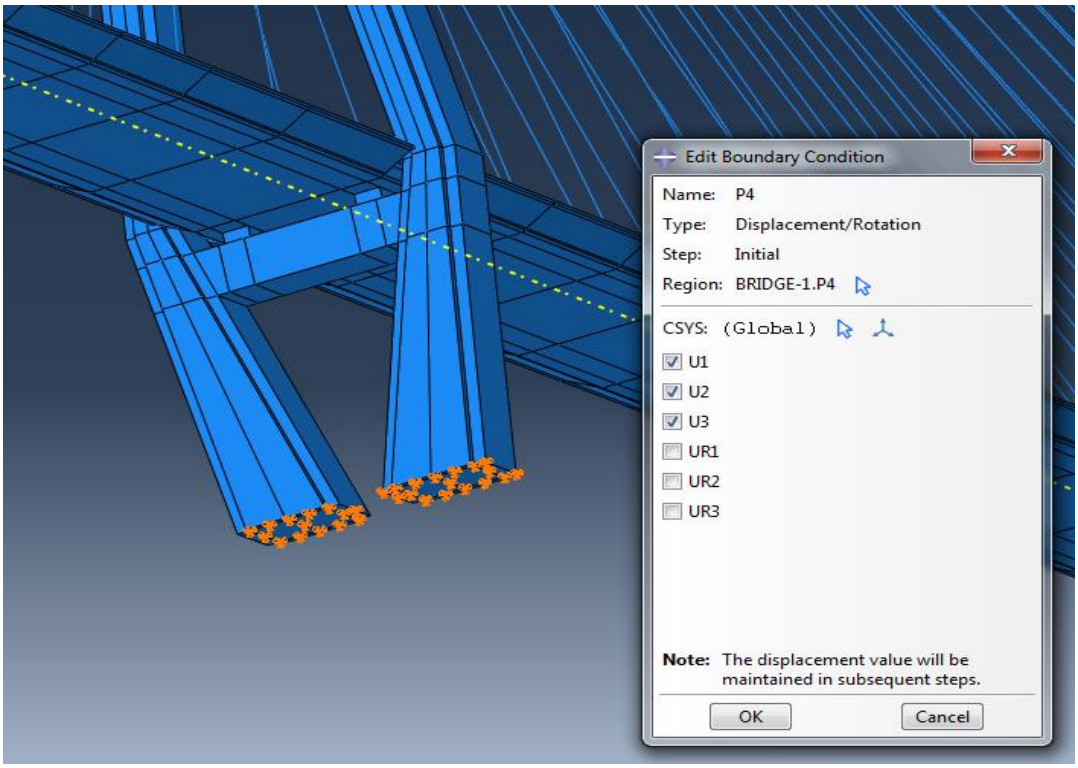

Figure 2.13 Boundary condition at bottom of main tower

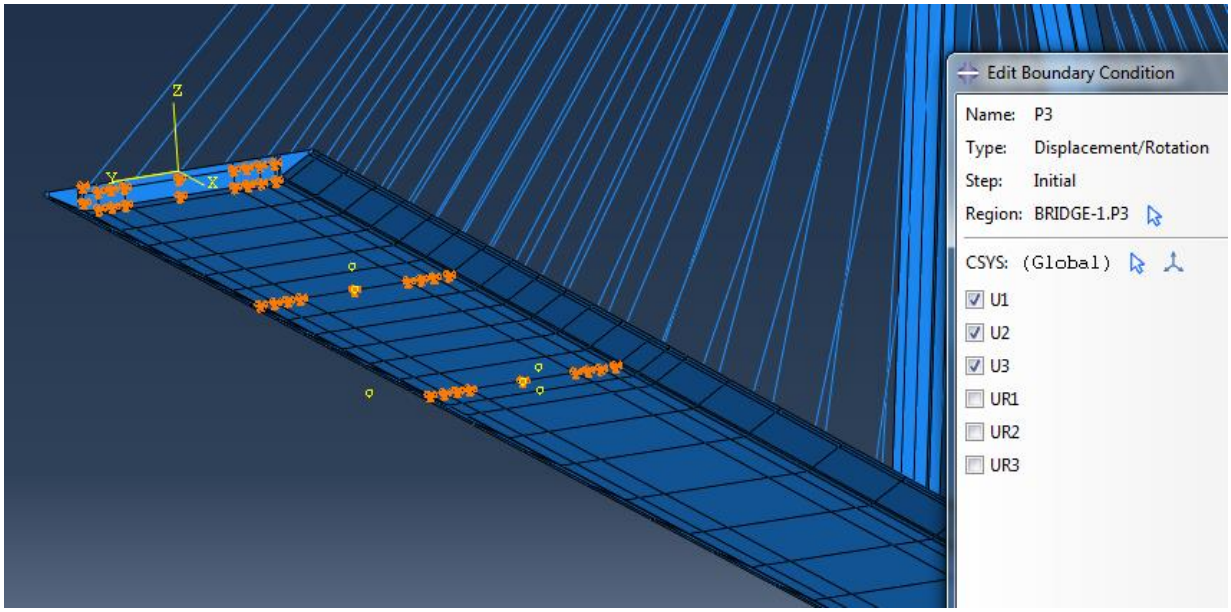

Figure 2.14 Boundary condition at side span

2.4 RESULT AND DISCUSSION OF MODAL ANALYSIS

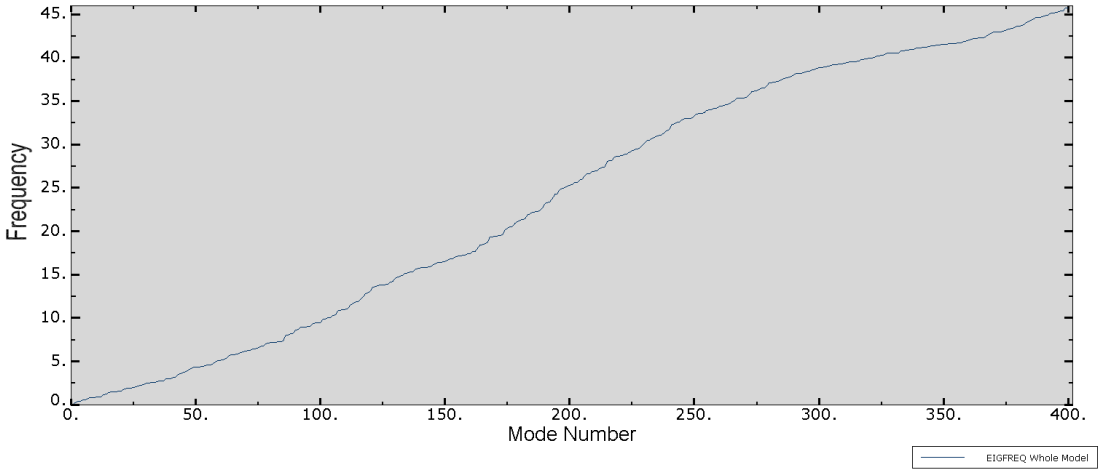

Figure 2.15 Distribution of first 400 frequencies

In this section, the results of modal analysis via Lanczos solver are demonstrated. The distribution of first 400 frequencies is shown in Figure 2.15. Here only part of the mode shapes

are shown in Figure 2.16 to 2.23 and corresponding descriptions of results are listed in Table 2.2. Compared with the results presented by Honshu-Shikoku Bridge Authority, the errors of first 5 modes are 10.7%, 15.5%, 29.3%, 38.1% and 2% respectively.

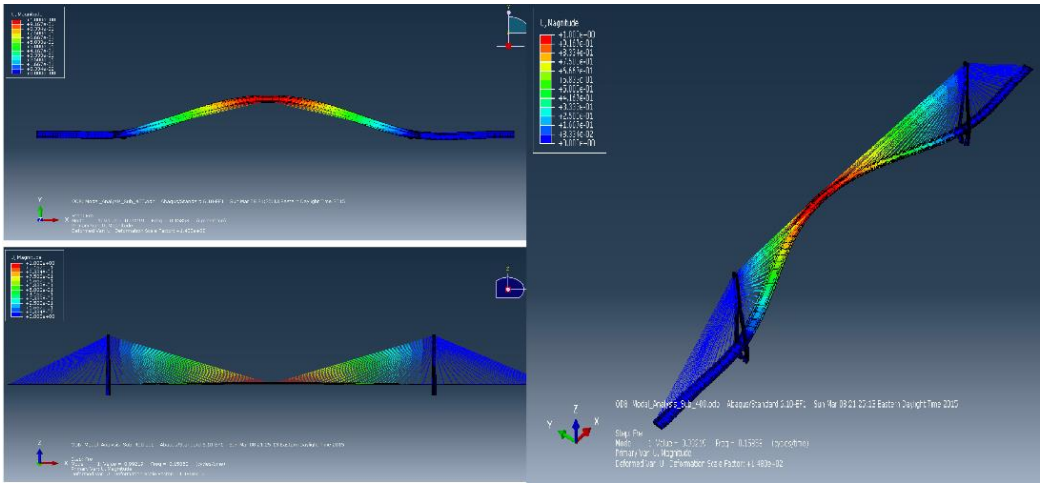

Figure 2.16 First vibration mode

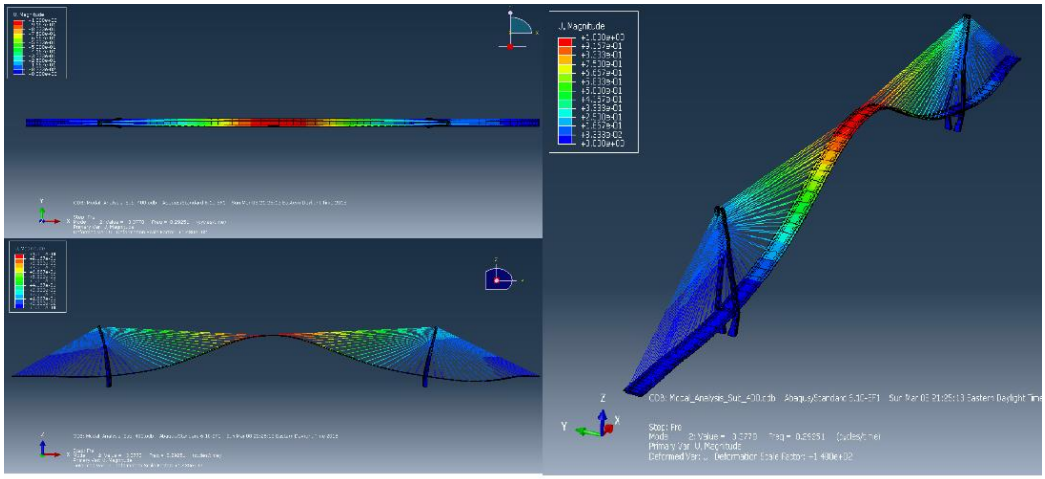

Figure 2.17 Second vibration mode

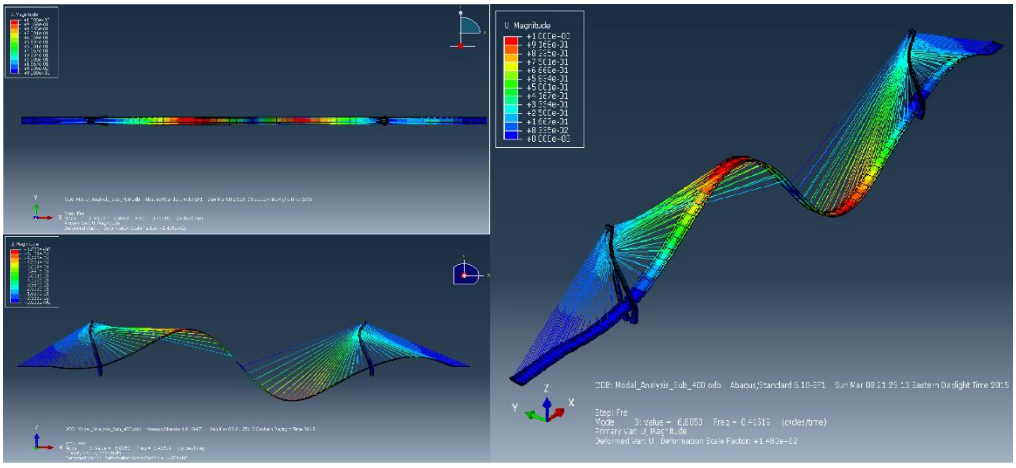

Figure 2.18 Third vibration mode

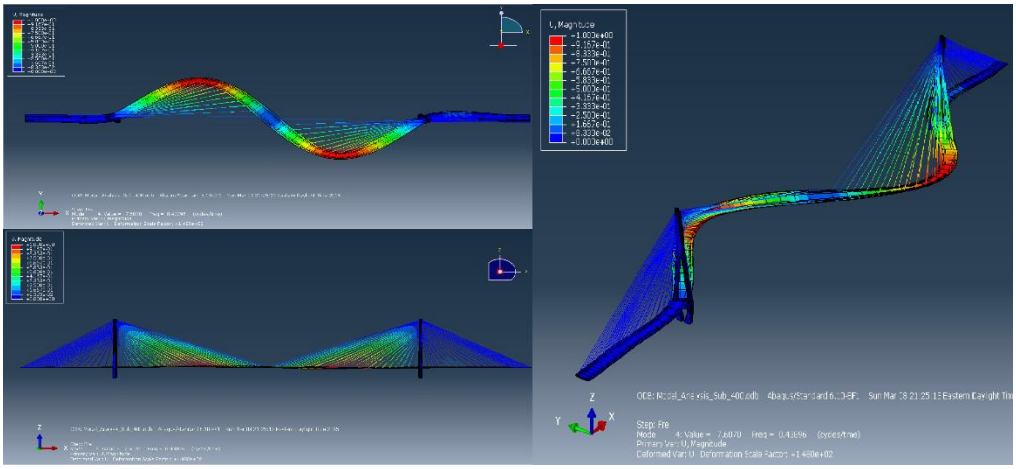

Figure 2.19 Fourth vibration mode

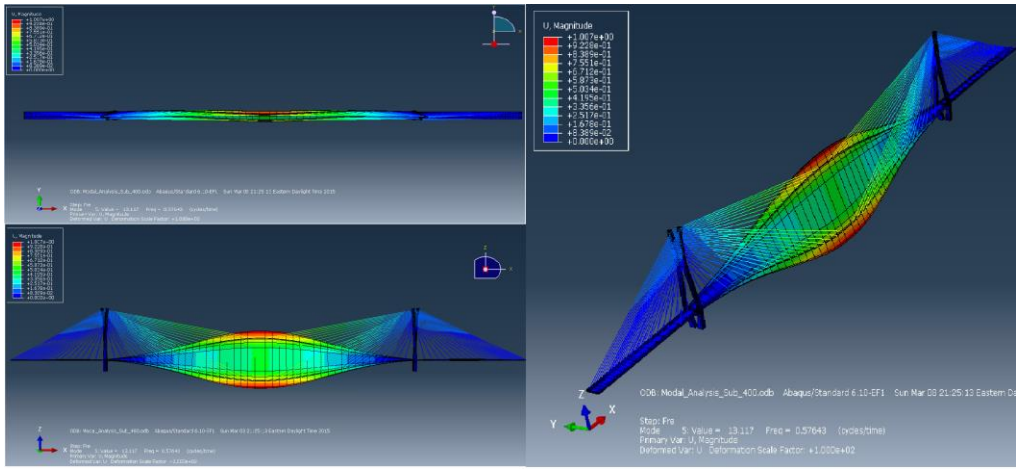

Figure 2.20 Fifth vibration mode

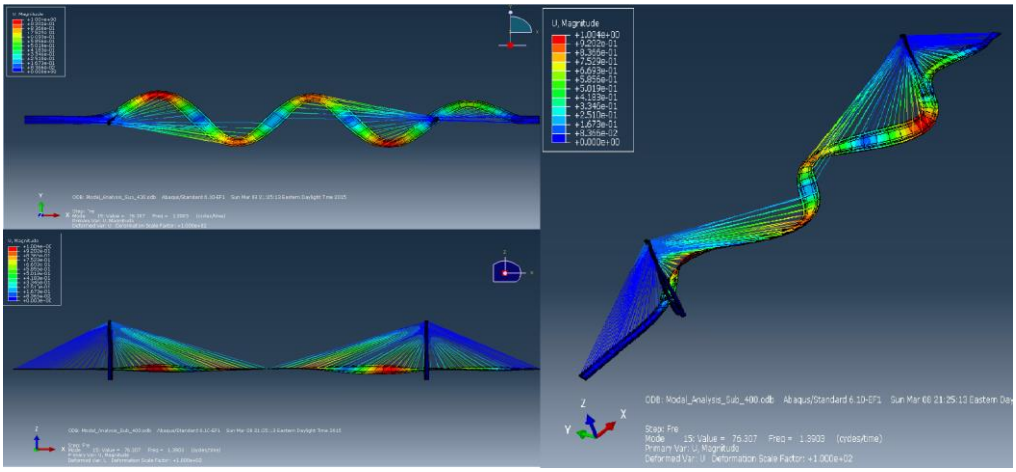

Figure 2.21 15th vibration mode

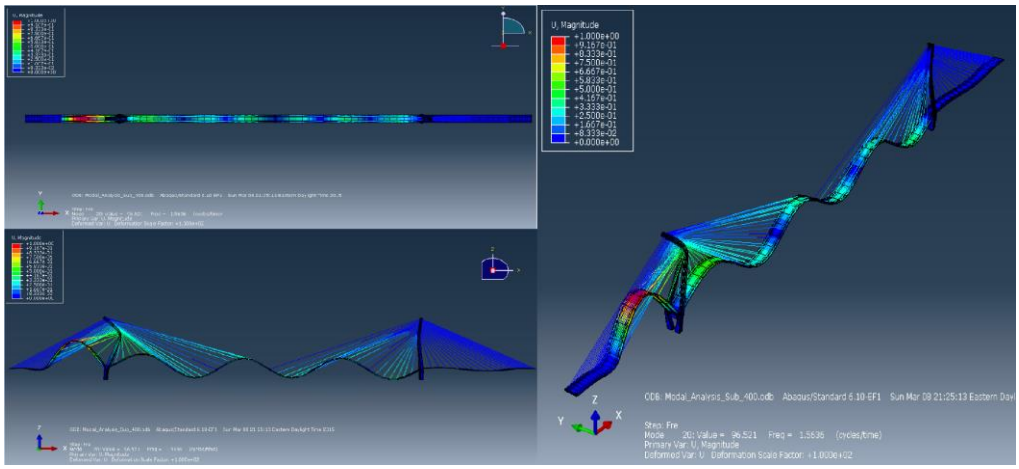

Figure 2.22 20th vibration mode

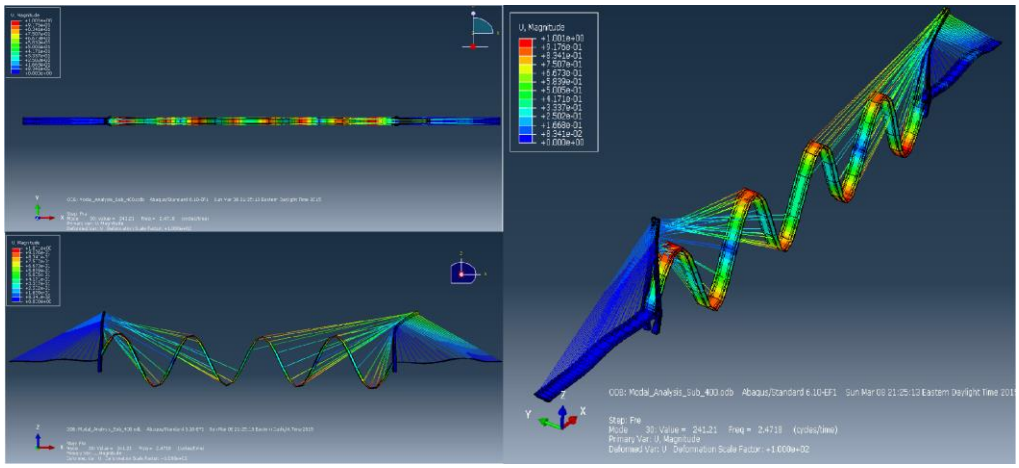

Figure 2.23 30th vibration mode

Table 2.2 First 30 frequencies and corresponding vibration shape description

Mode	Frequency/Hz	Cycle time/s	Features of mode shapes
1	0.15853	6.30795433	S L vibration of Girder
2	0.29251	3.418686541	S V vibration of Girder, associated with LG bending of Tower
3	0.41519	2.408535851	AS V vibration of Girder, associated with LG bending of Tower
4	0.43896	2.278111901	AS L vibration of Girder
5	0.57643	1.734816023	S T vibration of Girder, associated with L bending of Tower
6	0.6063	1.649348507	S V vibration of Girder, associated with LG bending of Tower
7	0.7774	1.286339079	AS T vibration of Girder, associated with L bending of Tower
8	0.78906	1.267330748	AS T vibration of Girder, associated with L bending of Tower
9	0.79913	1.251360855	AS V vibration of Girder, associated with LG bending of Tower
10	0.86665	1.153868344	S L vibration and associated with T of Girder
15	1.3903	0.719269222	S L vibration of Girder, associated with L bending of Tower
20	1.5636	0.639549757	AS V vibration of Girder, associated with LG bending of Tower
25	2.0024	0.499400719	S V vibration of Girder, associated with LG bending of Tower
30	2.4718	0.404563476	AS V vibration of Girder, associated with LG bending of Tower

(Note: S-symmetric, AS-antisymmetric, L-lateral, V-vertical, T-torsional, LG-longitudinal)

2.5 CONCLUSION OF MODAL ANALYSIS

According to the result of modal analysis, we can draw the conclusions about the Tatara Bridge as follows:

(1) The mode shapes are completely symmetric or antisymmetric.

(2) The first order mode shape is lateral vibration of girder and its cycle time is 6.308s, longer than 5s, which means the bridge is a flexible engineering structure (Fan 1997).

(3) The second order mode shape is vertical vibration of girder and associated with longitudinal bending of the main towers.

(4) According to the first order mode, it may be fruitful to reduce the response corresponding to lateral wind load by optimizing the deck shape.

(5) In the first 3 modes, there are two kinds of vertical vibration mode shapes. Thus it is reasonable to conclude the vertical stiffness of the bridge is weaker than in other directions.

3.0 WIND TUNNEL TEST BY CFD SIMULATION

To analyze the dynamic response of a bridge under crosswind which is the core of this study, the key step is to evaluate the aerodynamic forces of the bridge. In practice, wind tunnel test is always adopted in seeking for the information about the aerodynamic forces on the deck. As discussed in the first chapter, using CFD simulation method to model a wind tunnel test in computer is a better choice comparing to the time consuming experiments. Here the commercial software SOLIDWORKS FLOW SIMULAITON developed by Dassault Systemes Corp. is employed for modeling the wind tunnel test. This package has been used by over 2 million engineers and designers at more than 165,000 companies worldwide (Company Info SolidWorks 2015) and proved to be reliable in CFD modeling.

Evaluating the aerodynamic force corresponding to various deck shapes is the primary task in this modeling. This information can guide the optimization to reduce the lateral aerodynamic force, which is the most effective way to lower the lateral vibration of the bridge under the crosswind of the frequency close to the natural frequency of the bridge. Basically, the virtual wind tunnel test lays the foundation of the bridge optimization discussed in the next chapter. In this test, the aerodynamic load will be measured in a 2D simulation, including the horizontal force, vertical force, total force, torque in longitudinal direction of deck, drag coefficient and lifting coefficient.

3.1 DESCRIPTION OF MODIFIED DECK SHAPES

In the simulation, wind force applied to the deck depends on the windward surface area and sharpness of edges of deck. Therefore, various modifications of the original deck shape (Figure 3.1), which are depicted in Figure 3.2 and Figure 3.3, are analyzed in order to obtain the information about the corresponding aerodynamic forces. Note here most modifications are made to the two sides of original deck, and the height of deck shape is not changed (all 2.7m). The details about the modification are described below.

Here Deck 2 is changing from the original deck via sharpening the vertical surface of original deck. From Deck 3 to Deck 10, 8 deck shapes are divided into two groups based on their difference and similarities. For the first group, from Deck 3 to 7, in order to keep the same space for original traffic design, the dimension of top and bottom surfaces are not changed, while the horizontal positions of the tips on the edges of deck are extended by 4 m on each side. Meanwhile, the vertical positions of deck tips are set to be different to achieve different sharpness (see Figure 3.2). In the second group, from Deck 8 to 10, the two sharp tips are fixed vertically at mid of the height while the horizontal positions of the tips are set to be different (see Figure 3.3). We want to study the impact of changing only tips' vertical positions on aerodynamic forces generated on decks in Group 1, and the influence of altering only the tips' horizontal positions in Group 2. The information obtained here helps further aerodynamics optimization.

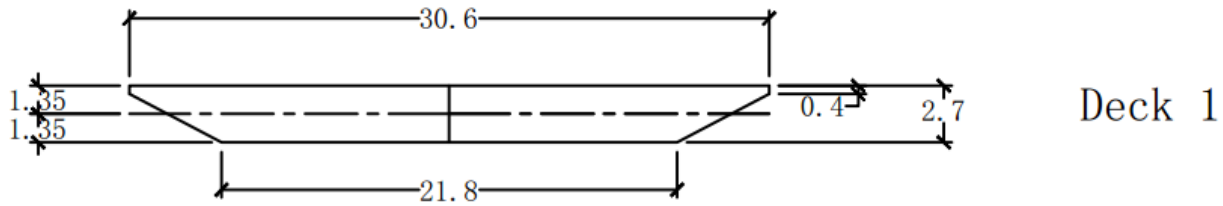

Figure 3.1 Deck shape of original deck (Deck 1)

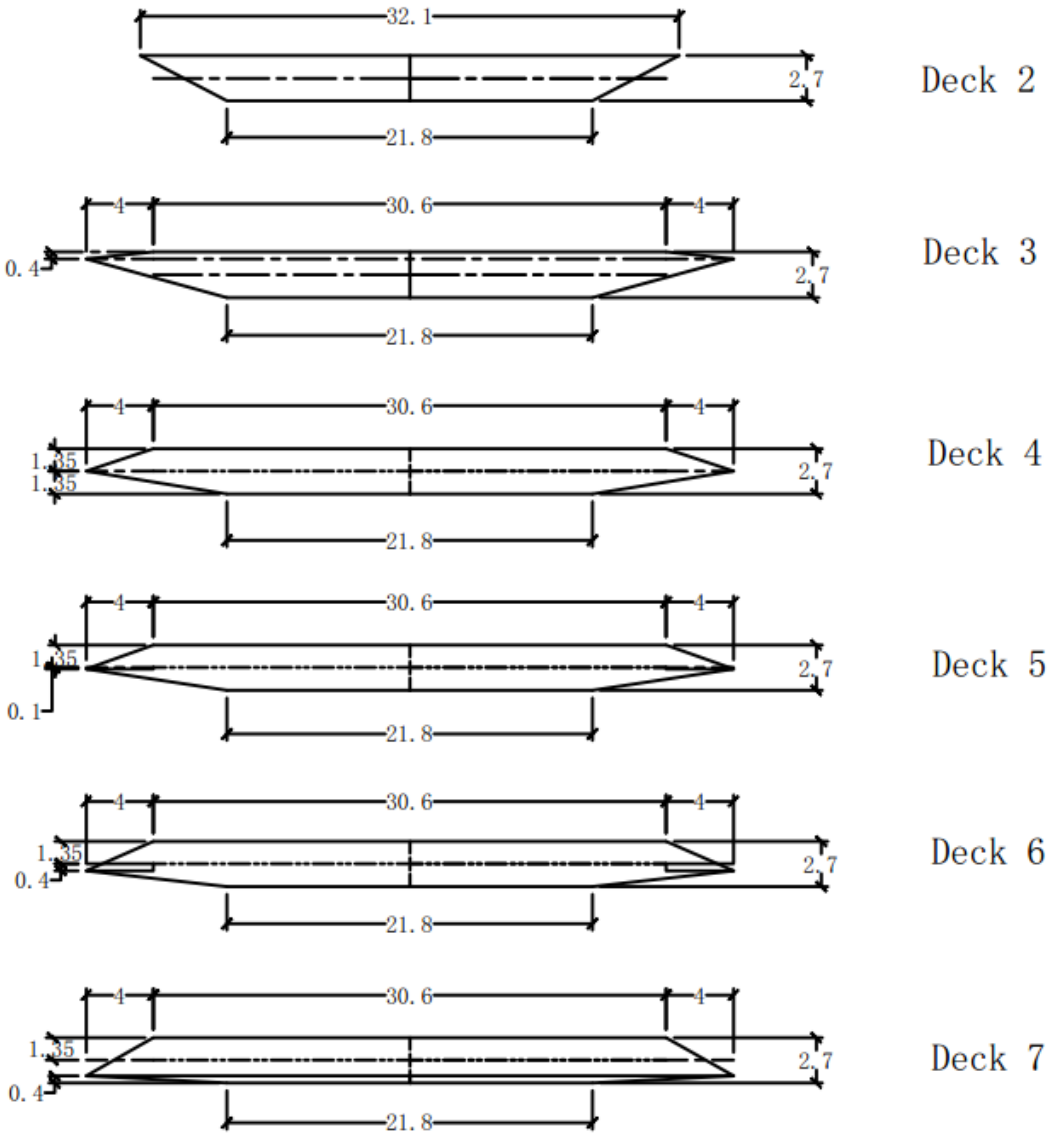

Figure 3.2 Optimized deck shapes of Group 1 (Deck 2 to 7)

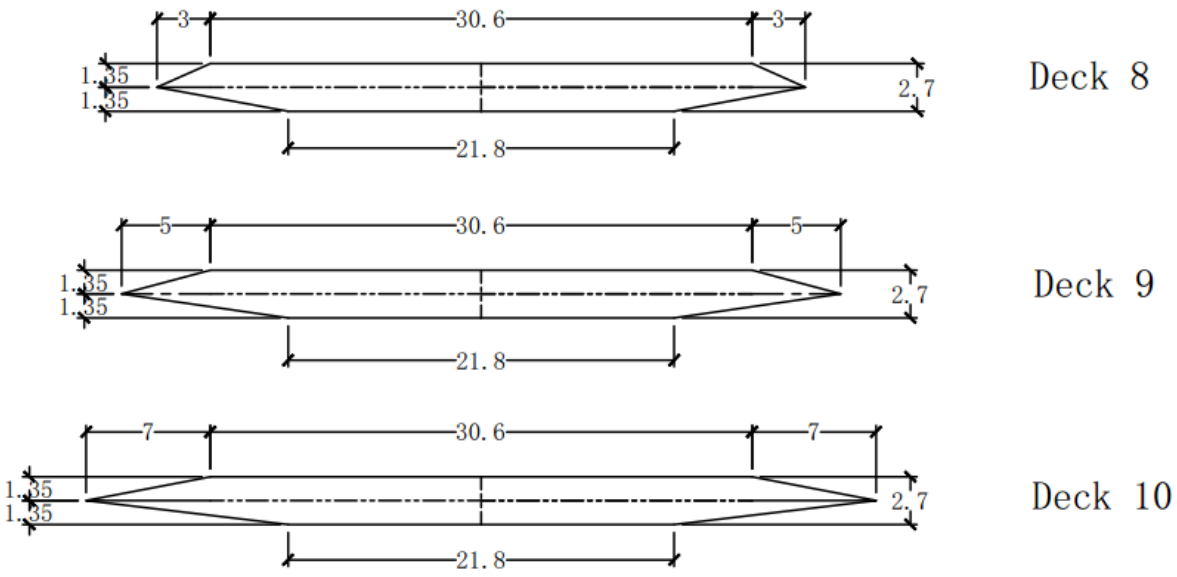

Figure 3.3 Optimized deck shapes of Group 2 (Deck 8 to 10)

3.2 HORIZONTAL WIND TEST SIMULATION

The lateral vibration in horizontal plane will be the main dynamic response of the bridge, according to the result of modal analysis which shows that the first order mode is lateral bending. Therefore, it is reasonable to minimize the horizontal aerodynamic force with the purpose of increasing the stability of the bridge. To prepare information for this optimization, here the virtual horizontal wind test is carried out first.

3.2.1 Horizontal wind test simulation

In this test, the responses of decks with various shapes are simulated under horizontal wind. Here only the highest designed wind speed condition of the bridge is taken into consideration, which is

63.6m/s (142mph) for the Tatara Bridge according to the details of design (Wilson 2009). SOLIDWORKS FLOW SIMULATION software package is employed to carry out the virtual test. The application of SOLIDWORKS FLOW SIMULATION package, which is designed particularly for CFD, makes it convenient to get the details of fluid-solid interaction, especially visualization of the process (Figure 3.4 and 3.5).

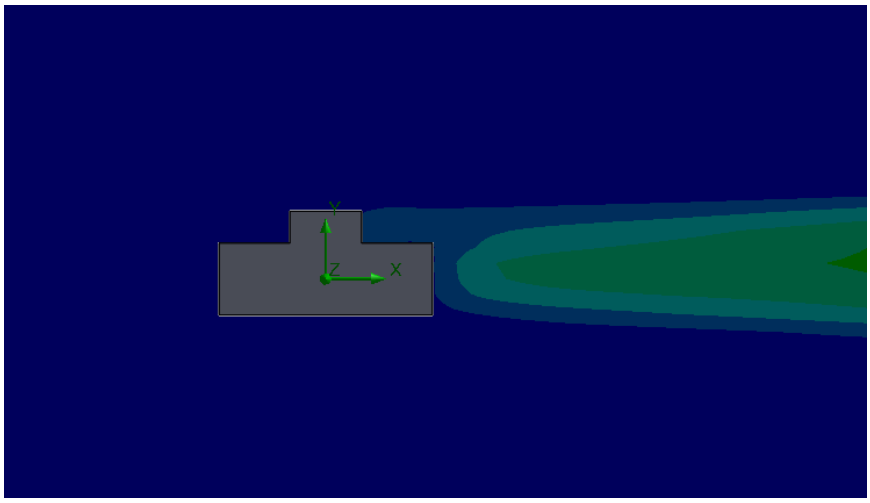

Figure 3.4 Turbulent viscosity of block

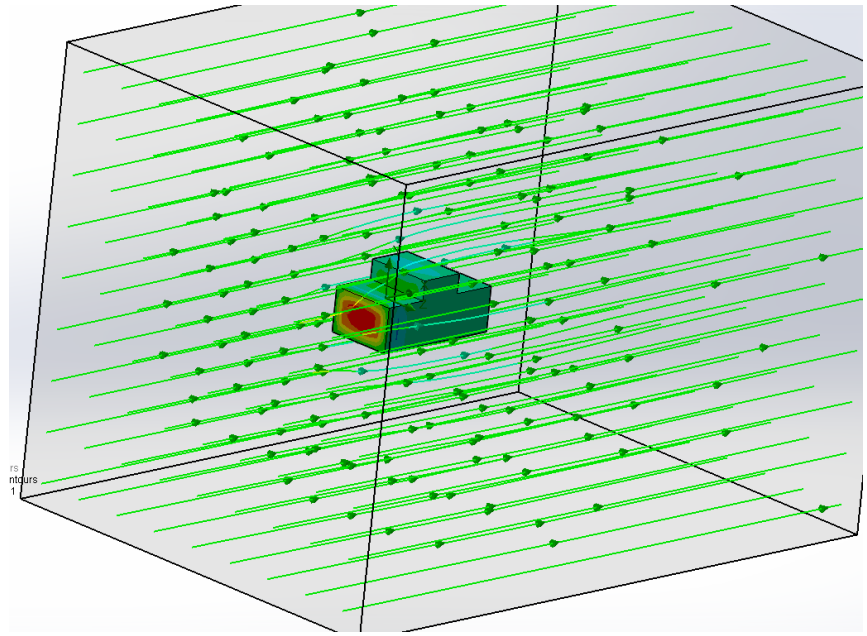

Figure 3.5 Aerodynamic test of block by SOLIDWORKS FLOW SIMULATION

In the simulation process, the main task is to model deck solid and air region. Based on the details of deck cross-section shapes (see Figure 3.1, 3.2 and 3.3), the deck solid models can be made by stretching sketch (see Figure 3.6) in the longitudinal direction. For consistency, all deck models are set as 20 m long (see Figure 3.7). The Cartesian coordinates are adopted with origin located at the mass center of model.

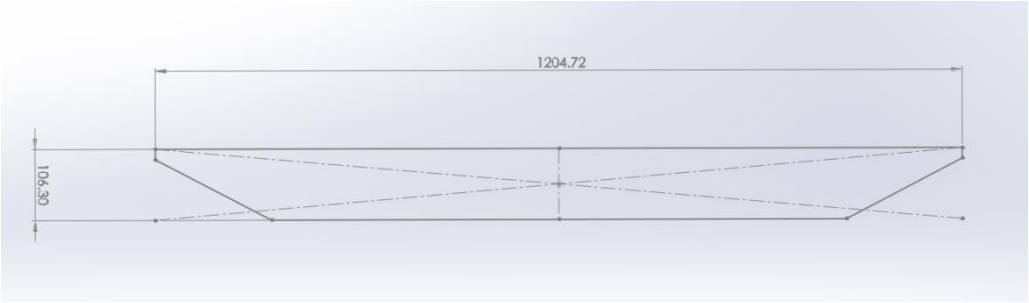

Figure 3.6 Sketch of original deck (Deck 1)

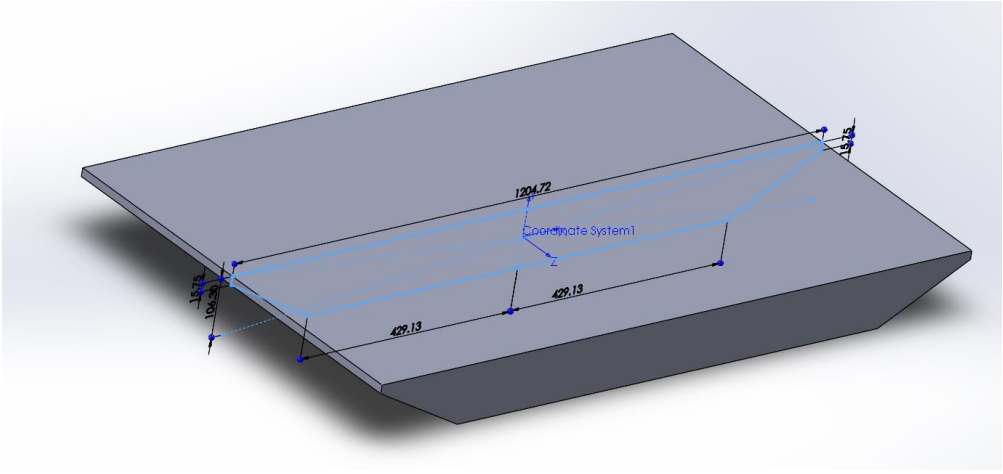

Figure 3.7 Solid deck shape of original deck extruded depending on its sketch

The air region modeling consists of material property importing, initial condition setting, computation domain arrangement and mesh refining. The coordinate system used here is same one that used in deck model. The fluid material is defined by air flow properties in this virtual test, as shown in Figure 3.8. For horizontal wind test, the initial condition of air flow is set as

horizontal moving with speed of 63.6 m/s (see Figure 3.9) which is the highest design wind speed of the Tatara Bridge. The size of the computation domain is set as 85 m long and 50 m high, with deck located at mid vertical position and offside horizontally a little to the left, as shown in Figure 3.10. In order to obtain proper results, the manual mesh setting is used here and explained in Figure 3.11.

During the test, horizontal force, vertical force, moment, drag coefficient, lifting coefficient and moment coefficient will be measured and prepared for further optimization process in the next chapter.

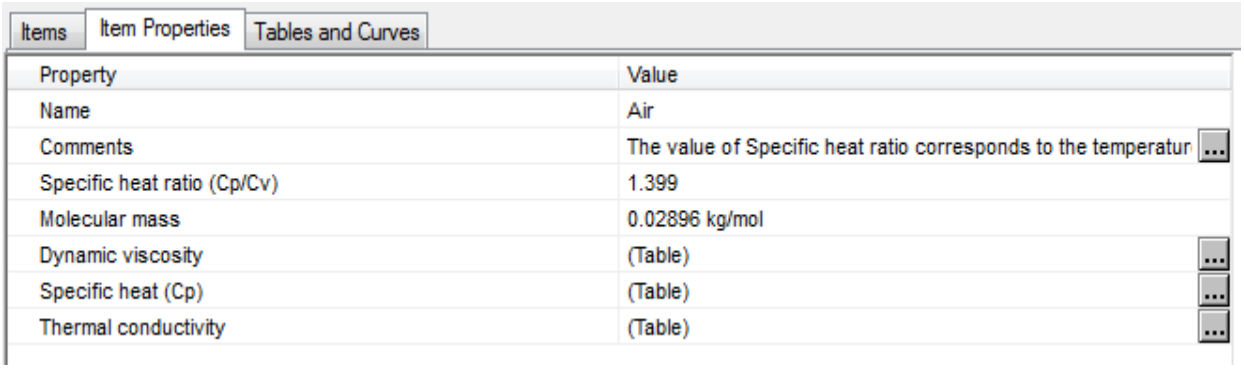

Figure 3.8 Material properties of air

General Settings

Parameter	Value
Parameter Definition	User Defined
Thermodynamic Parameters	
Parameters:	Pressure, temperature
Pressure	101325 Pa
Temperature	293.2 K
Velocity Parameters	
Parameter:	Velocity
Velocity in X direction	63.6 m/s
Velocity in Y direction	0 m/s
Velocity in Z direction	0 m/s
Turbulence Parameters	
Parameters:	Turbulence intensity and length
Turbulence intensity	0.1 %
Turbulence length	0.027 m

Figure 3.9 Define initial condition

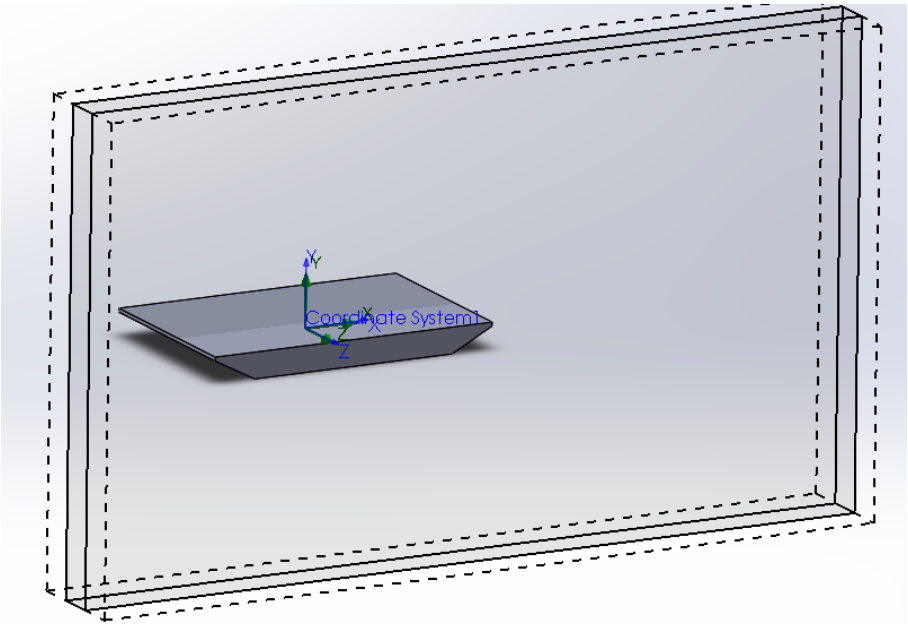

Figure 3.10 Computation domain of air region

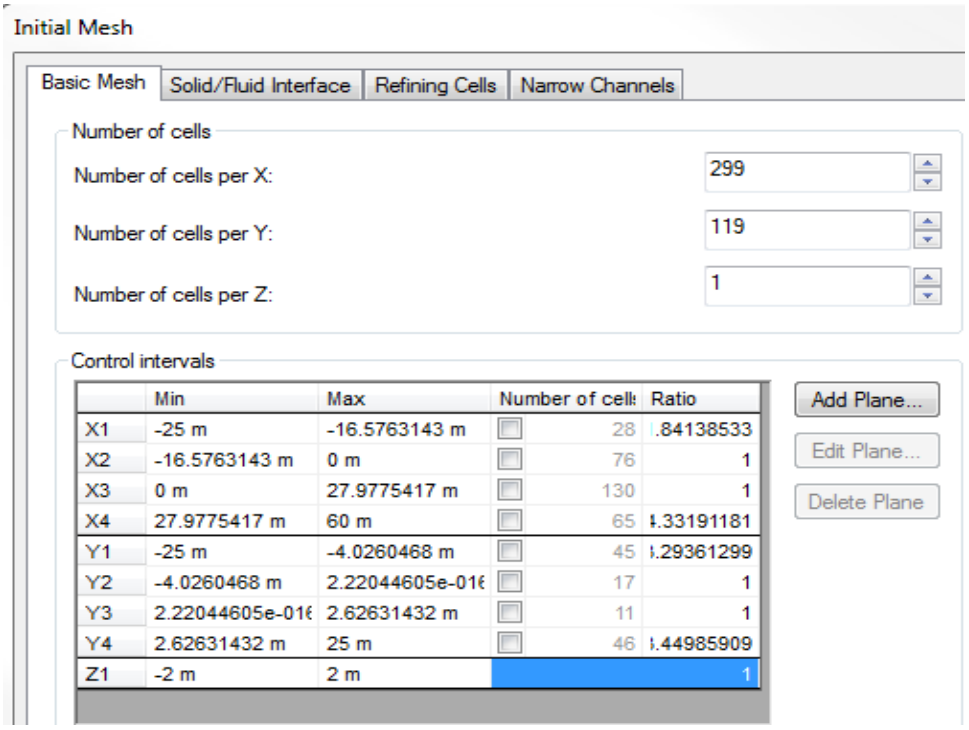

Figure 3.11 Basic mesh control

3.2.2 Result and conclusion of horizontal wind test in SOLIDWORKS

This section documented the result of the horizontal wind test simulation which is described in section 3.2.1 The details include the horizontal force (Force X), vertical force (Force Y), absolute value of Force Y, total force, torque in z direction, drag coefficient, lifting coefficient, moment coefficient and area of cross-section, followed by some discussions and conclusions. Here to show the powerful visualization of this SOLIDWORKS package, the turbulent viscosity of Deck 1 and Deck 4 is depicted in Figure 3.12 and Figure 3.13. As is shown in these figures, the interaction of the wind and Decks is clearly demonstrated.

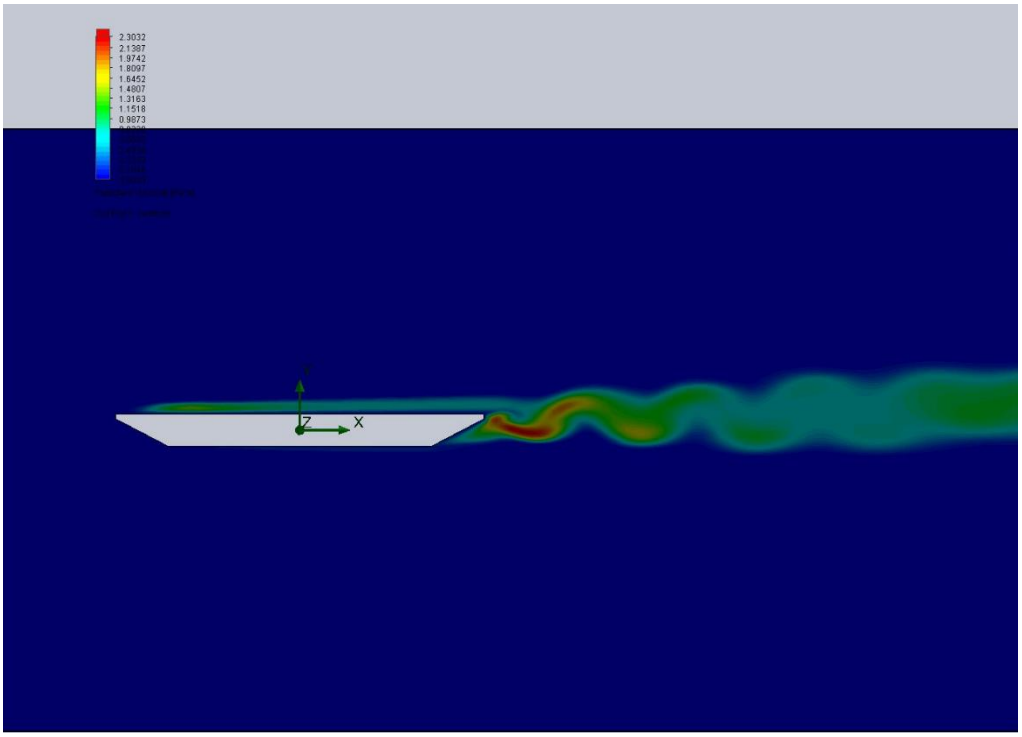

Figure 3.12 Turbulent viscosity of Deck 1 under horizontal wind

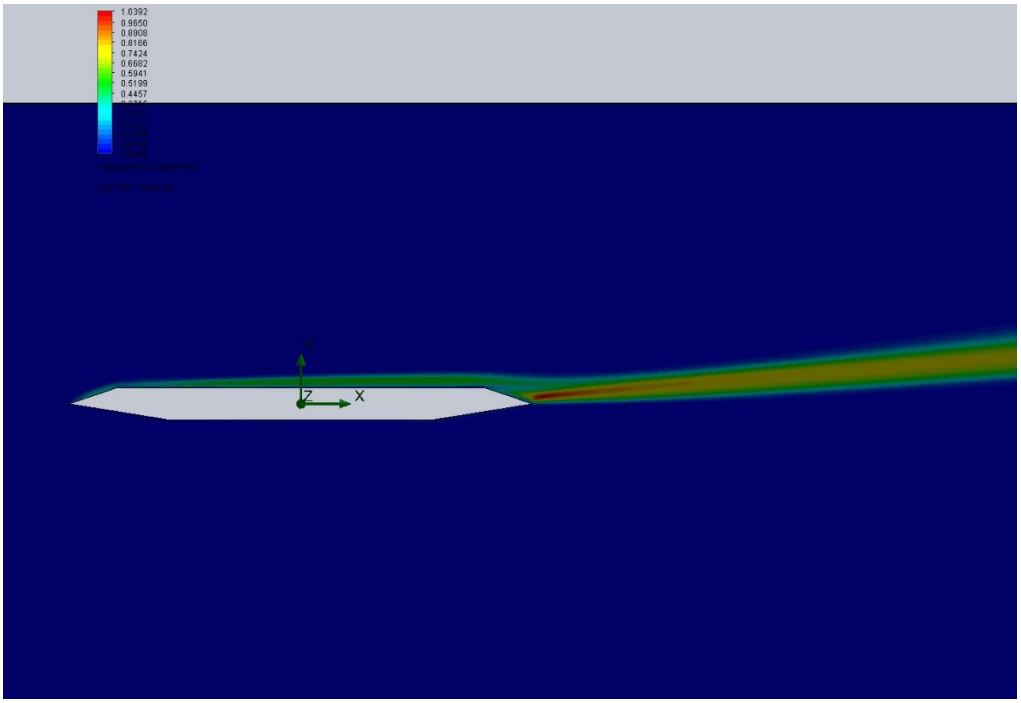

Figure 3.13 Turbulent viscosity of Deck 4 under horizontal wind

3.2.2.1 Result of horizontal wind tunnel test simulation

The results of Deck 1 and Deck 2 are compared in Table 3.1. It is easy to find that the aerodynamic forces are very sensitive to the deck shapes. The small change that modified small vertical surface (Deck 1) to sharp surface (Deck 2) on the edges of deck leads to the big variations of aerodynamic forces. In horizontal direction, the sharp surface can reduce 9.27% force. Thus, it is acceptable to conclude that a sharp surface is more suitable in reducing horizontal aerodynamic force than a vertical surface.

The results of Group 1 are documented in Table 3.2, and the aerodynamic forces are plotted with respect to the tips' vertical positions in Figure 3.14 and 3.15. In Figure 3.14 the forces are normalized by the maximum value of each term, while in Figure 3.15, the forces are plotted as the difference caused by modification of tips' vertical positions from the original shape, namely Deck 1.

As shown in Figure 3.14, with the tip moving from top to bottom, the horizontal force (Force X) achieves minimum value, which is corresponding to the shape of Deck 4. It can be concluded that middle height of the deck is the best vertical position to put sharp tips for producing minimum horizontal force.

For the vertical force (Force Y), with moving of tip from top to bottom, the direction changes from downward to upward, as shown in Figure 3.14. It is also shown in Figure 3.15 that the vertical aerodynamic force changed more significantly compared to horizontal one. And the minimum absolute value is also observed when the vertical position of tip is around the mid height of deck.

As to total force and torque Z, the similar results can be observed from Table 3.3 and Figure 3.15. Therefore, the shape of Deck 4 which reduces horizontal force, vertical force, total

force and moment by 70.3%, 79.9%, 77.2%, and 99.2% respectively has better behavior under the horizontal wind condition than the other selected shapes.

Table 3.1 Test results of Deck1 and Deck2

Deck	Force X (N)	Force Y (N)	Total Force (N)	Torque Z (N*m)	Drag Coefficient	Lifting Coefficient	Moment Coefficient	Area (m*m)
Deck 1	13871.68	-24563	28209.26	-441908	0.0785742	-0.13913	-2.50313	72.5
Deck 2	12585.53	-41479	43345.84	-524879	0.0709855	-0.23395	-2.96045	72.81

Table 3.2 Test results of Group 1

Deck	Force X (N)	Force Y (N)	Total Force (N)	Torque Z (N*m)	Drag Coefficient	Lifting Coefficient	Moment Coefficient	Area (m*m)
Deck 3	5418.246	-58615	58864.68	-529361.8	0.0267118	-0.28897	-2.60974	83.3
Deck 4	4116.969	-4933.2	6425.408	3652.3484	0.0193267	-0.02316	0.017146	87.48
Deck 5	4886.198	-7212.3	8711.588	17885.266	0.022823	-0.03369	0.08354	87.92
Deck 6	6128.33	4302.05	7487.596	159164.94	0.0282015	0.019797	0.732449	89.24
Deck 7	12123.18	27712.5	30248.21	469733.42	0.0543158	0.124161	2.104558	91.66

Table 3.3 Comparison from Deck 1 to Deck 7

Deck Number	1	2	3	4	5	6	7
Force x (%)	0	-9.2717	-60.9402	-70.32104	-64.77572	-55.82127	-12.6048
Force y (%)	0	68.8661	138.6307	-79.91612	-70.63763	-82.48561	12.82229
Force Total (%)	0	53.6582	108.6714	-77.22235	-69.11799	-73.45696	7.227921
Torque Z (%)	0	18.7757	19.79004	-99.1735	-95.95272	-63.98234	6.296651
Drag Coefficient (%)	0	-9.658	-66.0044	-75.40324	-70.95359	-64.1085	-30.8733
Lifting Coefficient (%)	0	68.1471	107.6918	-83.35526	-75.7874	-85.77103	-10.7613

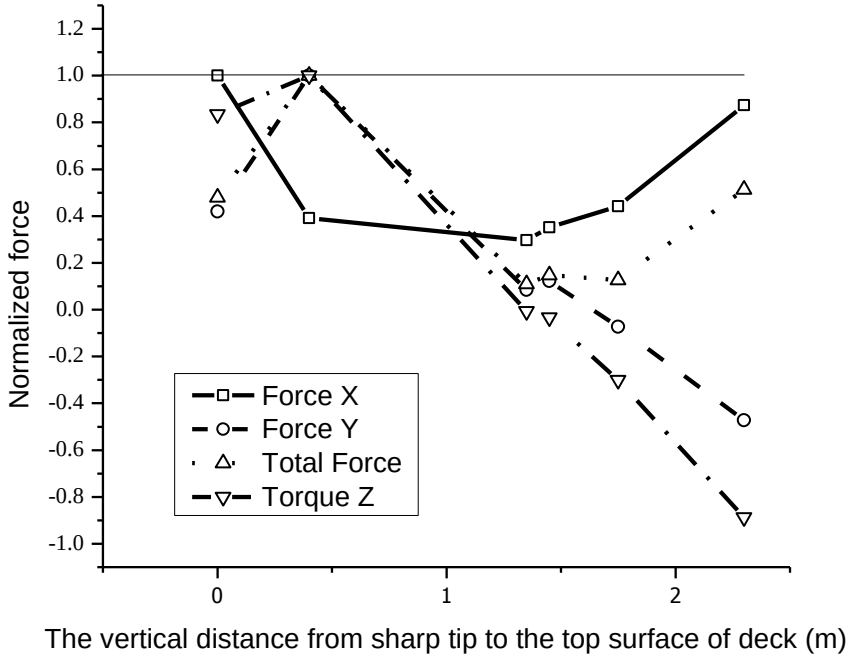

Figure 3.14 Normalized aerodynamic forces vs. the vertical of sharp tip

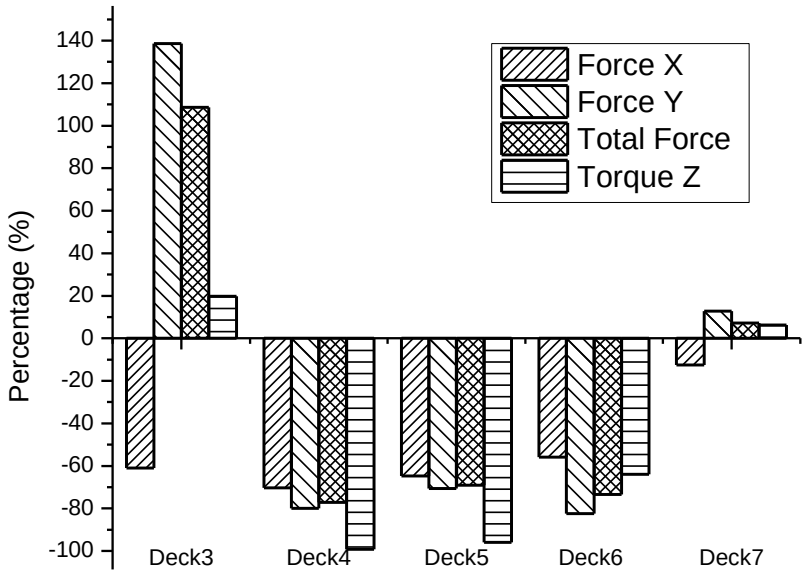

Figure 3.15 Aerodynamic forces comparison between Deck 1 and decks in Group1

Similarly, the results of Group 2 are documented in Table 3.4. And the aerodynamic forces are plotted with respect to the tips' horizontal positions in Figure 3.16 and 3.17. In Figure 3.16, the forces are normalized with respect to the maximum values.

From Figure 3.16, it can be seen that the horizontal force monotonously decreases with the increase of horizontal extension of the sharp tip. However, the decrease is becoming less obvious especially when the extension is longer than 4 m, as shown in Figure 3.17.

Unlike horizontal force, the vertical force and torque do not have this behavior. They change directions when the horizontal extension of tips reaches 5 m and 4 m respectively (see Figure 3.16 and 3.17), which means the minimum vertical force is at 5 m and minimum torque is at 4 m.

Based on the discussion above for horizontal wind condition, the deck with the horizontal extension of 4 m has better behavior for reducing aerodynamic force.

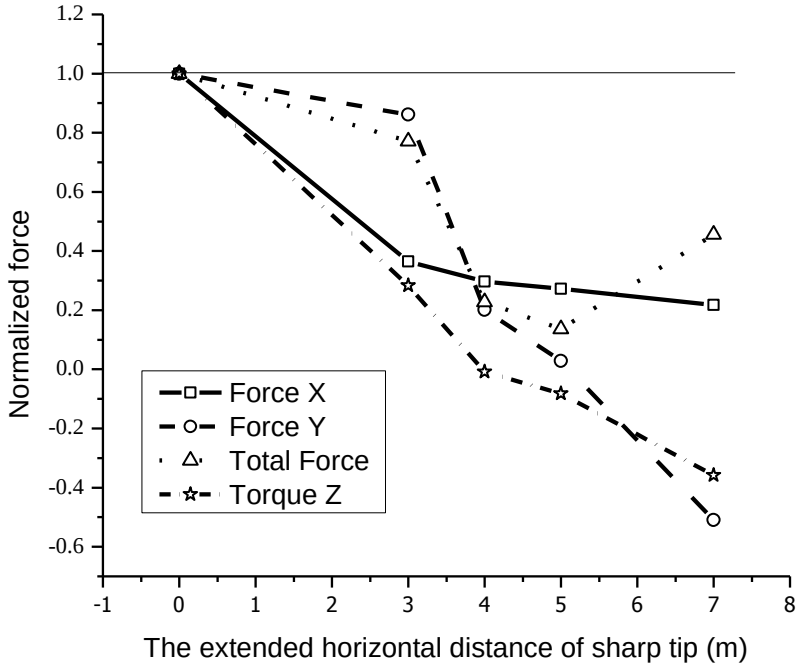

Figure 3.16 Normalized aerodynamic forces vs. the extended horizontal distance of sharp tip

Table 3.4 Test results of Group 2

Deck	Force X (N)	Force Y (N)	Total Force (N)	Torque Z (N*m)	Drag Coefficient	Lifting Coefficient	Moment Coefficient	Area (m*m)
Deck 8	5057.443	-21167	21762.93	-124997.8	0.0243228	-0.101799	-0.60115	85.39
Deck 9	3773.08	-701.81	3837.795	36397.554	0.0171821	-0.003196	0.165749	90.18
Deck 10	3025.596	12512.9	12873.47	158044.86	0.0129997	0.0537625	0.679051	95.58

Table 3.5 Comparison between Deck 1, Deck 2 and Deck in Group 2

Deck Number	1	2	8	4	9	10
Force x (%)	0	-9.2717	-63.5412	-70.32104	-72.80012	-78.18868
Force y (%)	0	68.8661	-13.825	-79.91612	-84.14281	-49.05797
Force Total (%)	0	53.6582	-22.8519	-77.22235	-80.39527	-54.36439
Torque Z (%)	0	18.7757	-71.7141	-99.1735	-91.76355	-64.2358
Drag Coefficient (%)	0	-9.658	-69.0448	-75.40324	-78.13272	-83.45553
Lifting Coefficient (%)	0	68.1471	-26.8335	-83.35526	-97.70297	-61.3591
Moment Coefficient (%)	0	18.27	-75.984	-99.31503	-93.37832	-72.87189
Area (%)	0	0.42759	17.77931	20.662069	24.386207	31.834483

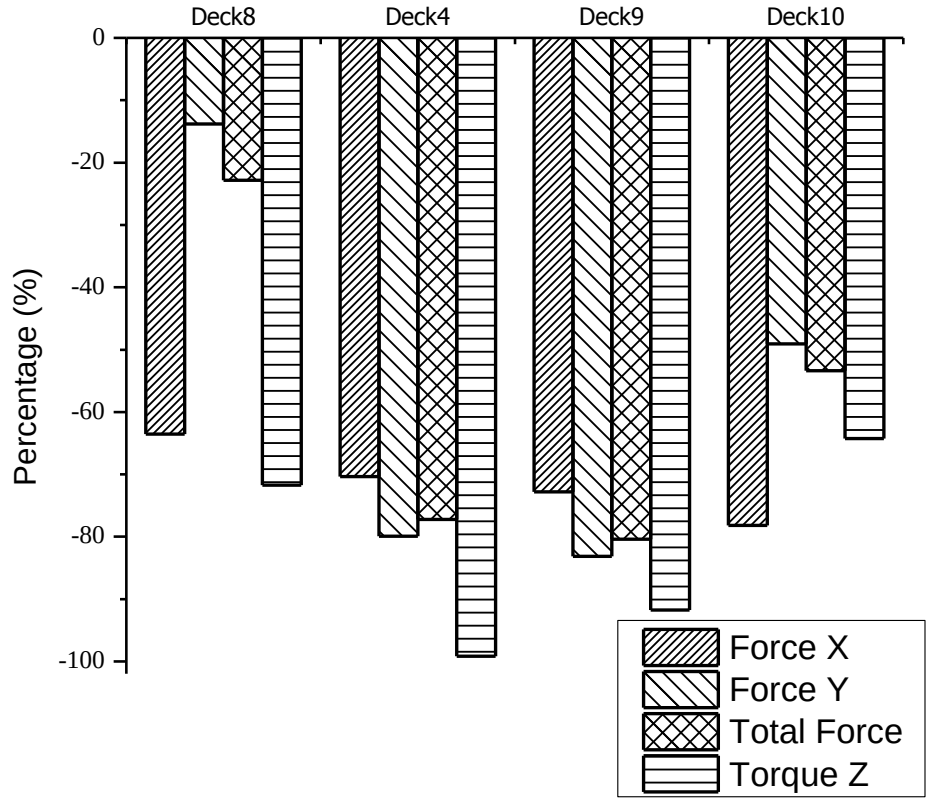

Figure 3.17 Aerodynamic forces comparison between Deck 1 and decks in Group2

Based on the data above, the optimization of the bridge deck can be briefly discussed here. It is always better to set the tips at the middle height of the deck and extend it horizontally to a proper position. Although bigger horizontal extension is shown to have a better behavior in reduce the aerodynamic forces, it is not practical to make it too big, since the rate of usable traffic area of deck and total surface have to be as low as possible in practice. Therefore, to gain the most significant reduction of aerodynamics forces without too much modification of original deck is the basic thought of this optimization.

Here a simple example is shown. Based on the result of Group 1, the area increase is not big with the vertical movement of the tips from top to bottom surface of deck. Thus, to set the sharp tip at mid height of deck is not bad. For the other direction, with the increase of horizontal

extension, the area of cross-section increases much more significantly. For both sides of deck, it is reasonable to set the horizontal extension to be 4 m. Because the cross-section area markedly grows up when the extension is bigger than 4 m, and at the same time the reduction of aerodynamic forces is not obvious compared to the area changes. . As a result, the shape of Deck 4 which has 4 m horizontal extension is the best choice among these 9 selected deck shapes. It reduces force in horizontal direction by 70.3%, force in vertical direction by 79.9%, total force by 77.2% and moment by 99.2%. This effect of deck shape modification is obvious, under horizontal wind condition.

3.2.2.2 Conclusion of horizontal wind tunnel test simulation

Based on the test results, the following conclusions can be made:

(1) The aerodynamic forces are very sensitive to the shape of deck.

(2) The sharp tip at mid height of deck is the most effective vertical position for reducing horizontal aerodynamic force under horizontal wind.

(3) In horizontal direction, the aerodynamic force decreases monotonously with the increase of horizontal extension of tips, and less obviously when the vertical position of tip is set at mid height of deck.

(4) With the deck shape changes, altering horizontal aerodynamic force is less significant than that of vertical aerodynamic force and torque.

3.3 NON-HORIZONTAL WIND TUNNEL TEST SIMULATION

In real situations, the wind direction is not always perfect horizontal and the angle between wind direction and horizontal direction has to be taken into consideration. Therefore, the information obtained above about the decks under horizontal wind may not be suitable for this non-horizontal condition. In this section, the virtual non-horizontal wind test is carried out for different attacking angles, from -7 to 7 degrees, the details of which are described in below.

3.3.1 Description of selected deck shapes

In the non-horizontal wind tunnel test simulation, only 4 typical decks (see Figure 3.18), namely Deck 1, Deck 3, Deck 4 and Deck 6 in the original collection, are tested to obtain the information about the corresponding aerodynamic forces. Deck 1 is the original deck shape which is used for comparison. Other 3 decks used here all have the 4 m horizontally extended sharp tip, but the vertical position of sharp tip is different. In addition to seeking the aerodynamic forces of these decks, this test is also designed to verify the guess that different wind conditions have different favorable shape of deck.

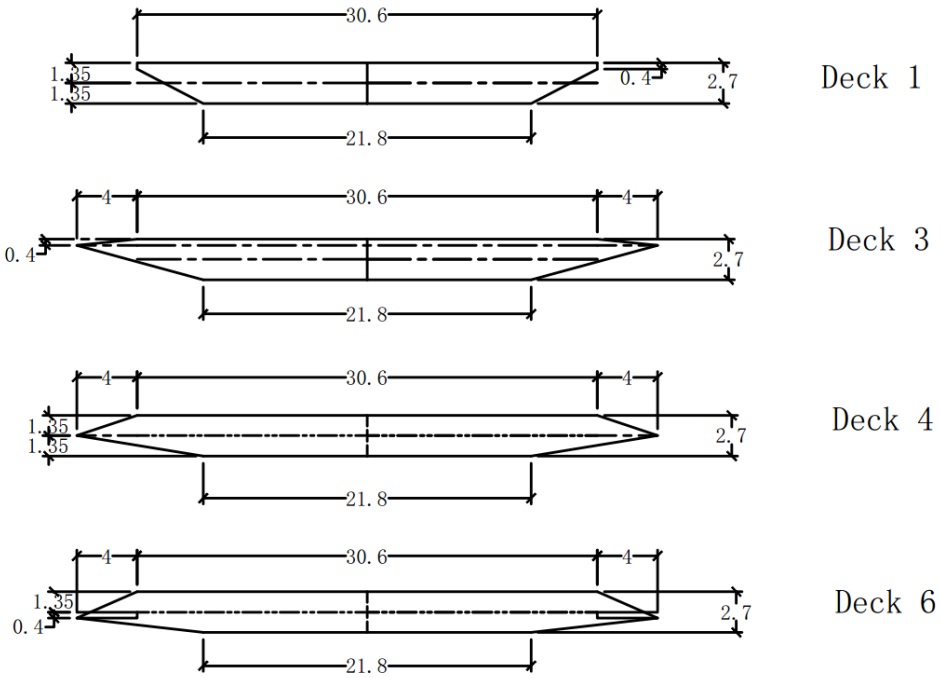

Figure 3.18 Deck shape selected for wind tunnel test simulation of non-horizontal wind

3.3.2 Non-horizontal wind tunnel test modeling

The modeling process of non-horizontal wind tunnel test is almost the same as that of horizontal wind tunnel test, except for slight modification of the initial conditions of air flow. To depict the modeling process, the Deck 4 solid model is shown in Figure 3. 19, and the initial conditions of air flow are shown in Figure 3.20 and 3.21. The wind speed is decomposed into vertical and horizontal components while keeping the constant magnitude of wind speed. The details about this decomposition are documented in Table 3.6. The positive attacking angle of wind is from top surface of deck to the bottom, shown in Figure 3.22, vice versa.

Table 3.6 Decomposition of wind velocity according to different wind attacked angle.

Attacked Angle (°)	-7	-6	-5	-4	-3	-2	-1	0
Velocity X (m/s)	63.126	63.252	63.358	63.445	63.513	63.561	63.59	63.6
Velocity Y (m/s)	7.751	6.648	5.543	4.437	3.329	2.22	1.1	0
Total Velocity (m/s)	63.6							

Attacked Angle (°)	1	2	3	4	5	6	7
Velocity X (m/s)	63.126	63.252	63.358	63.445	63.513	63.561	63.59
Velocity Y (m/s)	-7.751	-6.648	-5.543	-4.437	-3.329	-2.22	-1.1
Total Velocity (m/s)	63.6						

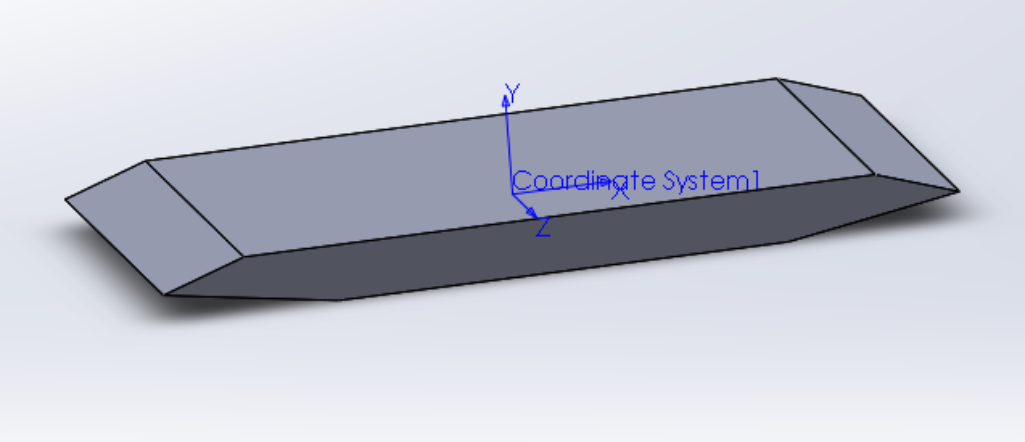

Figure 3.19 Deck 4 solid model in SOLIDWORKS

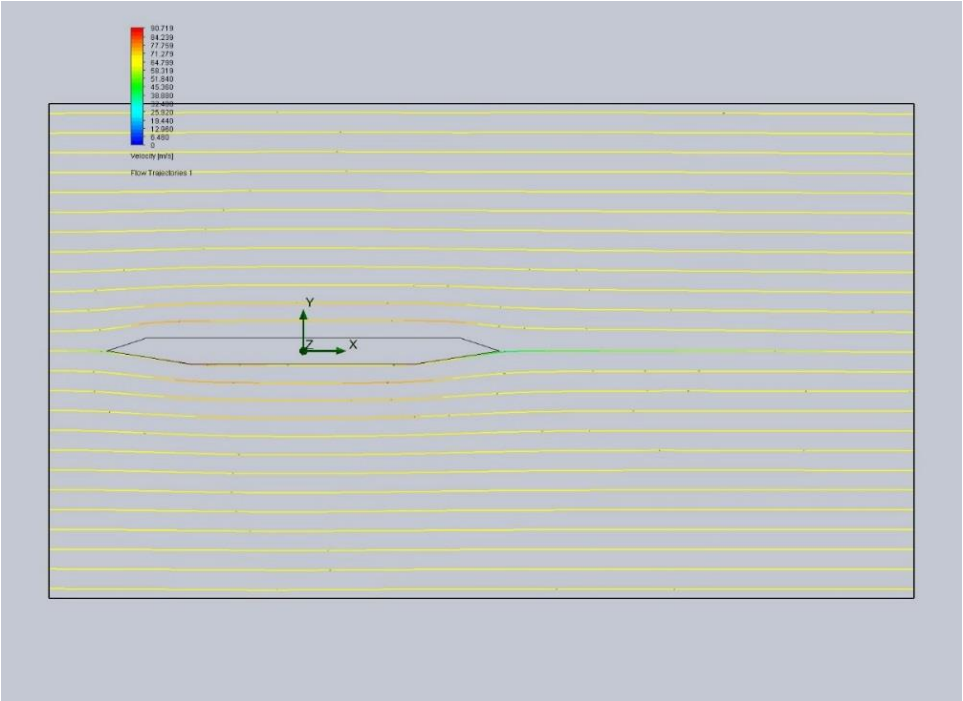

Figure 3.20 Deck in horizontal air flow

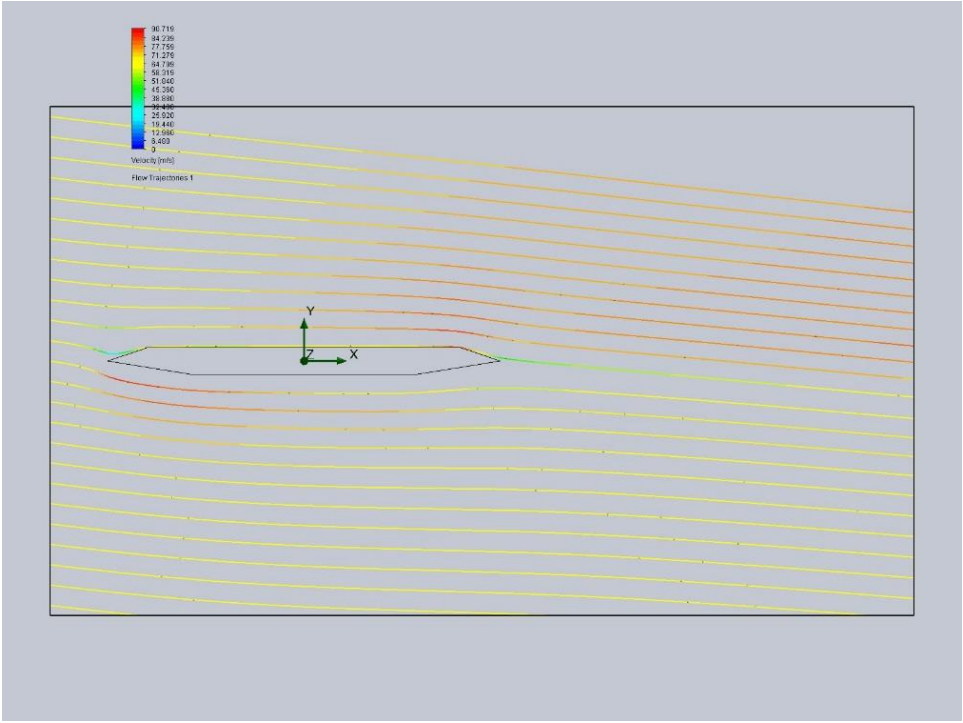

Figure 3.21 Deck in non-horizontal air flow

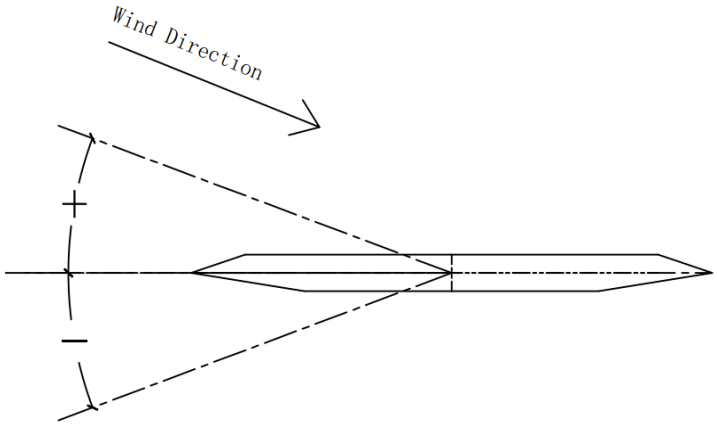

Figure 3.22 Definition of positive wind attacked angle

3.3.3 Result and conclusion of non-horizontal wind test

This section reports the result of Deck1, Deck2, Deck4 and Deck6 subjected to different wind conditions which are described in section 3.2. All of the results are calculated based on the initial setting that under 63.6m/s horizontal wind and wind attacking angle is from -7 to 7 degree, including the horizontal force (Force X), vertical force (Force Y), absolute value of Force Y, total force, torque in z direction, drag coefficient, lifting coefficient, moment coefficient. The area of cross-section is also evaluated when necessary. The discussions and conclusions are also reported in this section.

3.3.3.1 Result of non-horizontal wind test

The magnitudes of horizontal force, vertical force, total force and moment for different shape of the transformable deck, with respect to various wind attacking angles, are plotted from Figure

3.23 to Figure 3.26. In addition, the drag, lifting and moment coefficients with respect to different wind attack angles, are plotted in Figure 3.27, 3.28 and 3.29, respectively.

Taking a view at Figure 3.23 illustrating the wind-induced horizontal force, we can find that the force can change its direction with the change of the wind attacking angle. For decks 1 and 3, the horizontal force continuously decreases with the changing of attacking angle from -7 to 7 degree, and its direction changes when the attacking angle is greater than the certain angles, as shown in Figure 3.23. The similar trend can be also found for decks 4 and 6. The alternation of the direction of horizontal force when the attacking angle is large is of great interest and can further be utilized to reduce the dynamic behavior of the bridge. The minimum horizontal force for different wind attacking angles is listed in Table 3.7. The comparison between these minimum horizontal force and horizontal force of original deck (Deck 1) is shown in Table 3.8.

As for the vertical force, the force will generally decrease to 0 and then increase in opposite direction, for the wind attack angle changing from -7 to 7 degree. For the identical wind attacking angle, the vertical forces for different shapes of the bridge deck are nearly the same. The total force generated by the wind load, which can be decomposed into horizontal and vertical forces, can be seem in Figure 3.25. The torques of four decks, with respect to the wind attack angle, can be seen in Figure 3.26. According to the horizontal force, vertical force and moment analysis, the drag coefficient $C_D = \frac{2F_X}{\rho_{air} v^2 A}$, lifting coefficient $C_L = \frac{2F_Y}{\rho_{air} v^2 A}$ and Moment coefficient $C_M = \frac{2T}{\rho_{air} v^2 A}$ of the bridge are plotted as Figure 3.27, Figure 3.28, and Figure 3.29, respectively. The ρ_{air} is the density of air, F_X is the force in X direction, F_Y is the vertical force T is the torque in longitudinal direction, v is the wind speed and A is the section area.

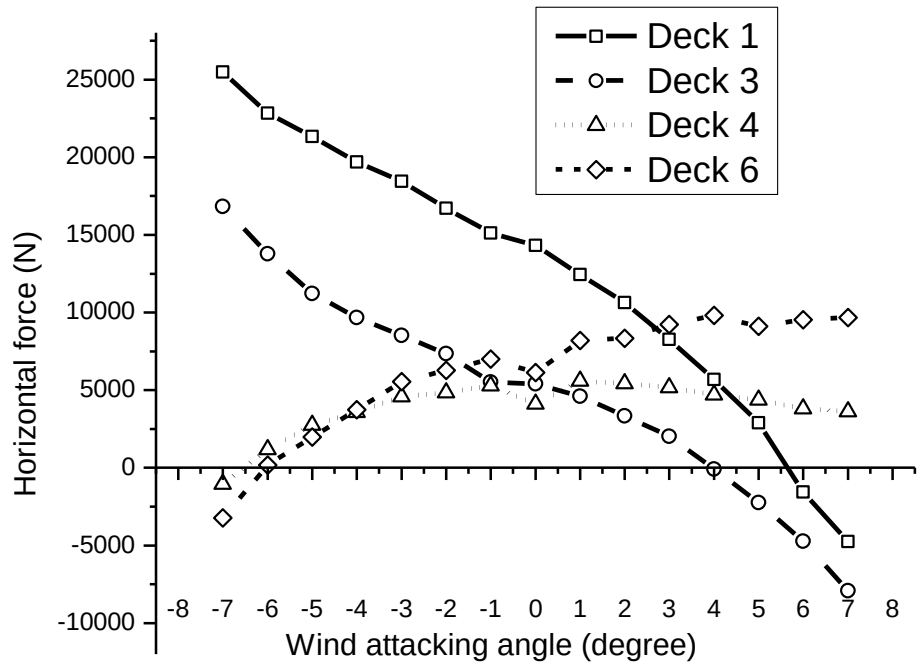

Figure 3.23 Horizontal force vs. wind attacking angle

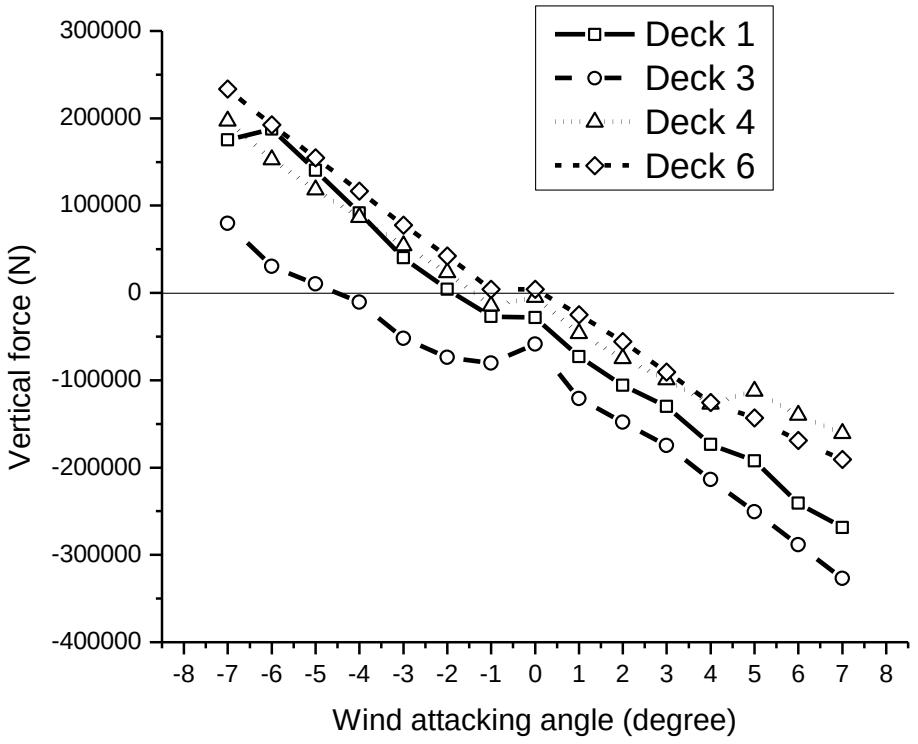

Figure 3.24 Vertical force vs. wind attacking angle

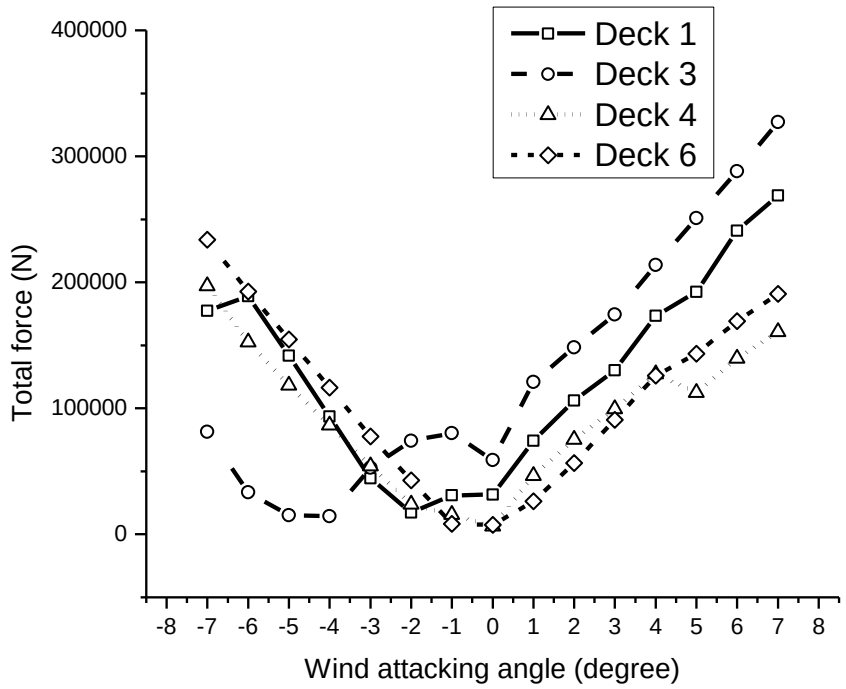

Figure 3.25 Total force vs. wind attacking angle

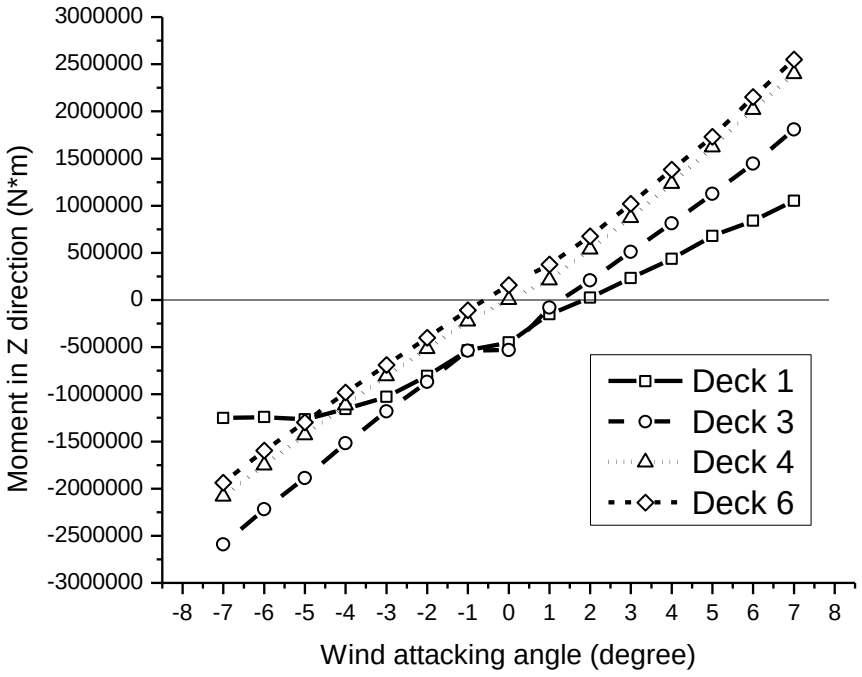

Figure 3.26 Moment vs. wind attacking angle

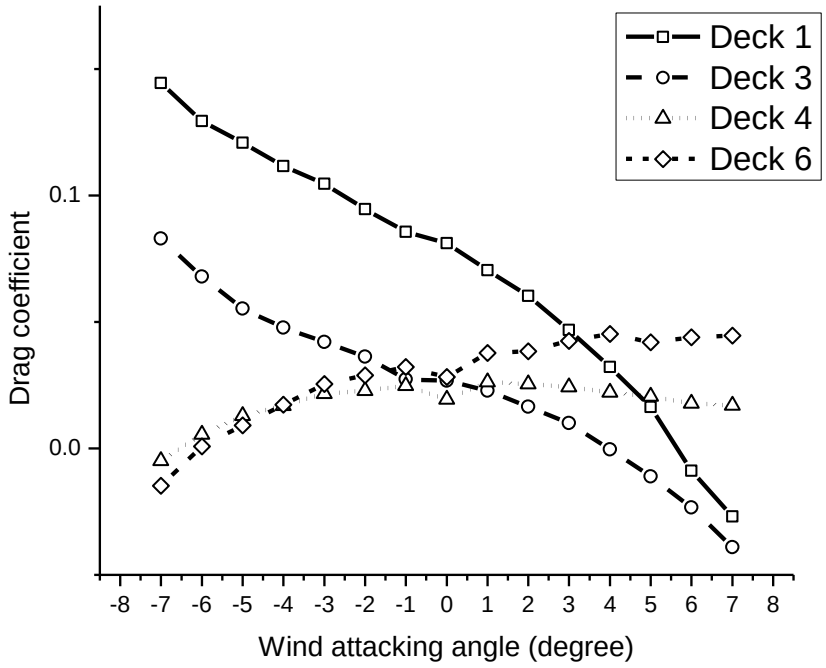

Figure 3.27 Drag coefficient vs. wind attacking angle

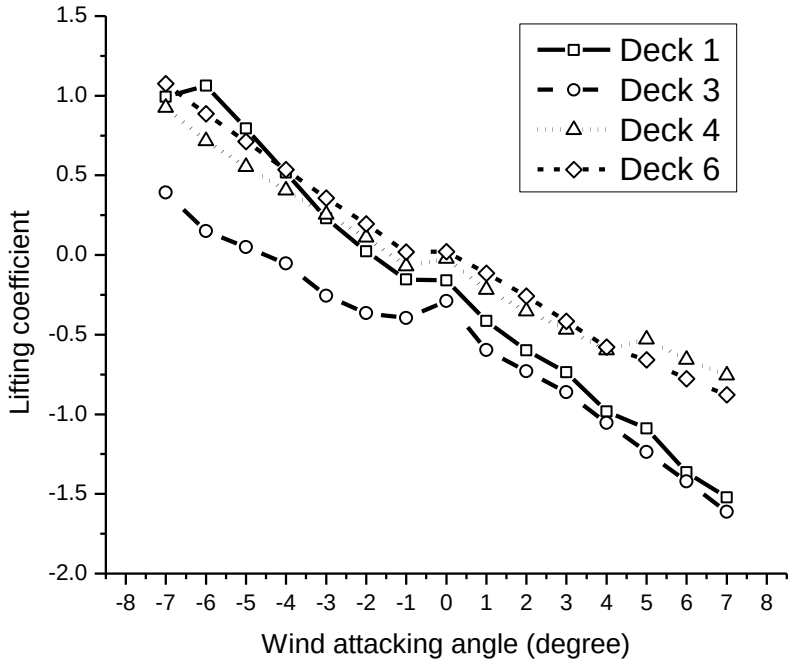

Figure 3.28 Lifting coefficient vs. wind attacking angle

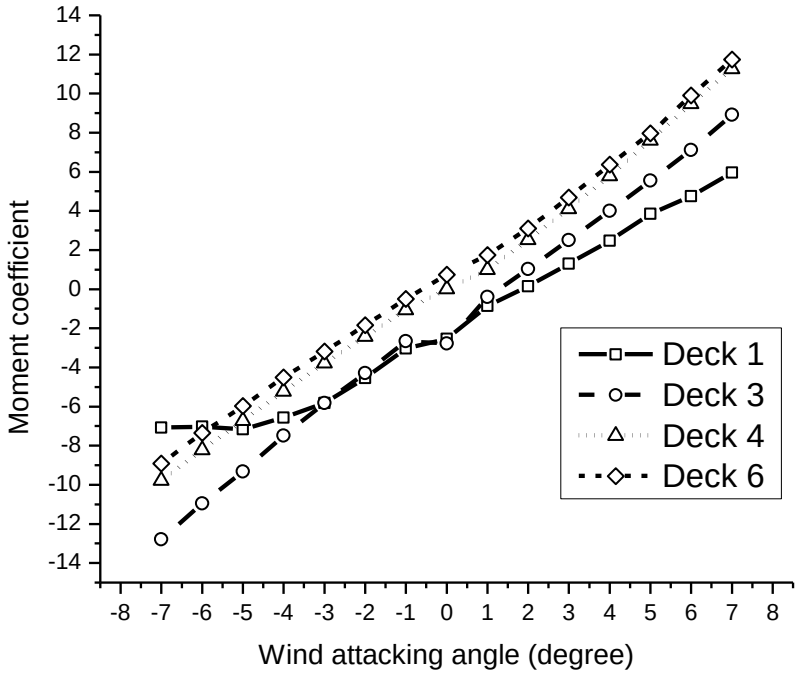

Figure 3.29 Moment coefficient vs. wind attacking angle

Table 3.7 Minimum magnitude of horizontal force with different angle

Minimum Magnitude of horizontal force					
Angle (°)	-7	-6	-5	-4	-3
Min Magnitude	1038.66929	169.882761	1985.24861	3582.885231	4595.43731
Force X (N)	-1038.6693	169.882761	1985.24861	3582.885231	4595.43731
Deck	Deck 4	Deck 6	Deck 6	Deck 4	Deck 4
Angle (°)	-2	-1	0	1	2
Min Magnitude	4850.21653	5283.77113	4116.96917	4614.256698	3340.10652
Force X (N)	4850.21653	5283.77113	4116.96917	4614.256698	3340.10652
Deck	Deck 4	Deck 4	Deck 4	Deck 3	Deck 3
Angle (°)	3	4	5	6	7
Min Magnitude	2036.43459	85.6859459	2249.79079	1570.639787	3616.187
Force X (N)	2036.43459	-85.685946	-2249.7908	-1570.63979	3616.187
Deck	Deck 3	Deck 3	Deck 3	Deck 1	Deck 4

Table 3.8 Comparison of minimum horizontal force of each deck shape

Comparison of the horizontal force value of minimum magnitude and original deck					
Angle (°)	-7	-6	-5	-4	-3
Min Magnitude	1038.66929	169.882761	1985.24861	3582.885231	4595.43731
Original deck	25490.1314	22844.5605	21333.1639	19698.97872	18459.2194
Effect (%)	-95.92521	-99.256354	-90.694073	-81.8118224	-75.104921
Angle (°)	-2	-1	0	1	2
Min Magnitude	4850.21653	5283.77113	4116.96917	4614.256698	3340.10652
Original deck	16702.1071	15117.6568	14326.0288	12437.17482	10640.6994
Effect (%)	-70.960451	-65.049007	-71.262314	-62.8994787	-68.610085
Angle (°)	3	4	5	6	7
Min Magnitude	2036.43459	85.6859459	2249.79079	1570.639787	3616.187
Original deck	8271.30243	5688.98923	2895.24021	-1570.63979	-4744.6676
Effect (%)	-75.379517	-98.493828	-22.293467	0	-23.784187

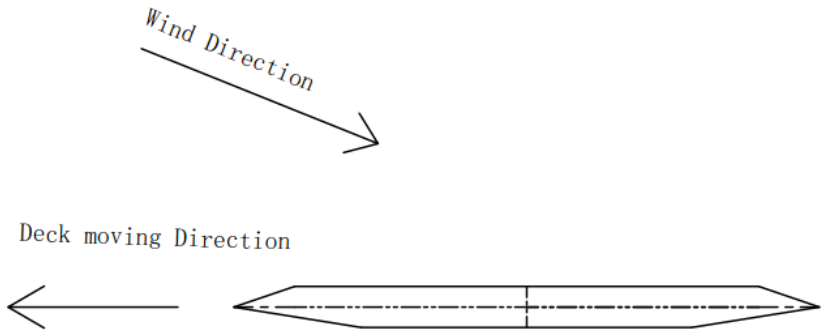

Figure 3.30 Deck moving direction sketch

3.3.3.2 Conclusion

(1) Under both non-horizontal and non-vertical wind, each deck shape has its own specific wind attacking angle at which the horizontal force of deck will be 0.

(2) Under both non-horizontal and non-vertical wind, each deck shape has its own specific wind attacking angle at which the vertical force of deck will be 0.

(3) Under both non-horizontal and non-vertical wind, each deck shape has its own specific wind attacking angle at which the moment of deck will be 0.

(4) The wind attacking angles which lead to 0 value of horizontal force, vertical force and moment are not same.

(5) This optimized method cannot reach the perfect theoretical value, 0, but still has a big effect on reducing horizontal force with different wind attacking angles.

(6) The direction of horizontal force of deck can be opposite to the direction of horizontal velocity of wind.

(7) Changing position of sharp tip to face to the direction of coming wind will reducing horizontal force.

(8) The horizontal force, vertical force and moment have general monotonicity with increasing of wind attacking angle.

(9) The optimized method is also available for reducing vertical force and moment of deck at different wind attacked angles.

4.0 OPTIMIZATION

4.1 DESCRIPTION OF OPTIMIZATION

The primary idea to reduce the dynamic response of this bridge is to install some transformable devices. These special devices can alter the shape of the girder at some critical locations of the bridge, and therefore improve the aerodynamic stability of the bridge. According to the result of modal analysis in Chapter 2, lateral vibration is the primary (first) vibration shape. Thus, the horizontal or skewed winds which have the similar frequency as the 1st vibration mode will lead to the dangerous dynamic response of girder even when the wind speed is not high enough. Under most cases, the bridges will suffer from horizontal or skewed winds. The vertical winds, from one aspect, they are not close to the 1^{st} vibration mode of the bridge in this study, and from another aspect, the gravity of the girder is much bigger than the aerodynamic force generated from vertical winds. Therefore, the horizontal wind with relatively small attacking angle has more influence on bridge vibration than vertical wind and is core of this study.

The purpose of the optimization is to reduce the lateral displacement of this cable-stayed bridge under horizontal/skewed winds, through the 110m long special device installed near the middle point in the bridge. Generally, the largest displacement always happens at the mid-span of the bridge, so dynamic response of the middle point of the bridge is the research focus.

The design wind speed (63.6 m/s) is selected as the maximum wind speed in this optimization. The duration time of wind is set as 120 seconds, which is according to the real measurement of the wind loads. For simplicity, the wind load is set in the sine form (see Figure 4.1) with the frequency being 0.15853, which is the same as the 1st mode of the bridge. In the Figure 4.1, the speed of the wind varies from 38.16 m/s to 63.6 m/s. The attack angle of the skewed wind is selected from -7° to 7°.

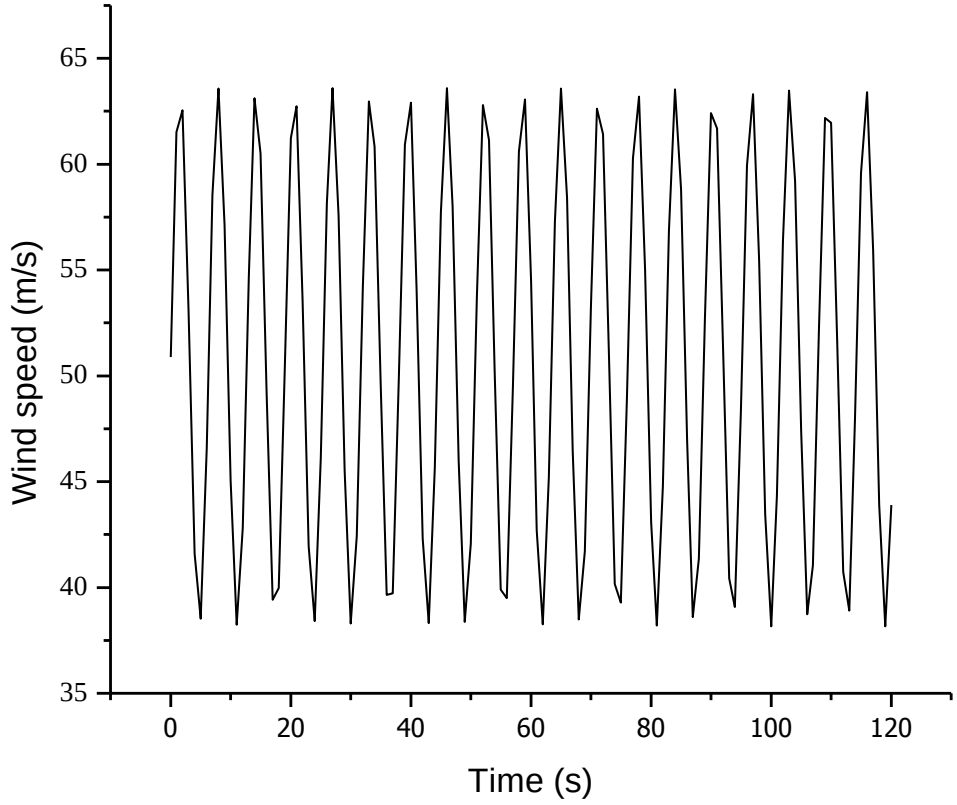

Figure 4.1 Wind speed amplitude vs. time

4.2 OPTIMIZATION PROCESS

The optimization can be divided into the following three steps:

1) The software SOLIDWORK is utilized to obtain the force distribution of the girder;

2) The force obtained from step 1) is applied to the finite element model of the bridge in ABAQUS to analyze its dynamic response under wind load; and

3) The dynamic responses for the bridge before and after the optimization are compared.

As for the step 1), the shape of the 110 m long transformable device should be determined with respect to the wind attacking angle. The force and moment distributions of the device with different shapes are already be analyzed in Chapter 3. Here, our purpose is to manually alter the shape of the device according to the wind attack angle. The principle of altering the shape is to reduce the horizontal wind force. Based on the limited test results in Figure 3.7, the shape of the transformable device is determined for different attacking angle ranging from -7° to 7°. The magnitudes of the horizontal/vertical forces and the moment are also determined under the wind speed being 63.6 m/s, see Table 4.1.

In step 2), the aerodynamic forces used in ABAQUS are calculated based on the aerodynamic coefficients which measured in virtual wind tunnel tests. Details are shown following:

$$F_D = qC_D A_1 \tag{4.1}$$

in which, fluid pressure $q = 0.5\rho v_c^2$, ρ is the density of air, v_c is the wind speed, F_D is the drag force, C_D is the drag coefficient, A_1 is the projected area.

$$F_L = qC_L A_2 \tag{4.2}$$

in which, fluid pressure $q = 0.5\rho v_c^2$, F_L is the lifting force, C_L is the lifting coefficient, A_2 is the plan area.

$$M = qC_M A_2 L_0 \tag{4.3}$$

in which, fluid pressure $q = 0.5\rho v_c^2$, M is the moment, C_M is the moment coefficient, L_0 is the width of deck.

Table 4.1 Best optimized deck shape choice with different wind attacked angles

Optimized Deck of Different Wind Attacked Angles				
Angle (°)	Deck	Force X (N)	Force Y (N)	Moment (N*m)
-7	Deck 6	-3216.9425	233709.18	-1938991.34
-6	Deck 6	169.882761	192550.132	-1595533.41
-5	Deck 6	1985.24861	154548.629	-1298061.19
-4	Deck 4	3582.88523	86669.9946	-1113600.67
-3	Deck 4	4595.43731	54117.4488	-805961.865
-2	Deck 4	4850.21653	23484.8536	-517431.998
-1	Deck 4	5283.77113	-14854.097	-226479.651
0	Deck 4	4116.96917	-4933.197	3652.348399
1	Deck 3	4614.2567	-120885.79	-80141.5788
2	Deck 3	3340.10652	-148209.33	207865.0206
3	Deck 3	2036.43459	-174569.24	510154.4878
4	Deck 3	-85.685946	-213763.06	813132.7501
5	Deck 3	-2249.7908	-250832.66	1125348.424
6	Deck 6	9530.49034	-168999.69	2153494.269
7	Deck 6	9687.57684	-190605.39	2551334.929

ABAQUS software is utilized and the finite element model used in bridge modal analysis can be directly reused. The force and moment distributions for the bridge, including the girder, the bridge tower, and the transformable device, are input into the finite model. Please note the magnitudes of the force and moment are simply proportional to the wind speed. The general static and explicit analysis methods are utilized for the analysis.

In the final step, the lateral displacement (U2) and total displacement magnitude U for the bridge before and after optimization are compared to validate the optimization effects. These comparisons can tell us the other factors which can be further optimized.

4.3 RESULT OF OPTIMIZATION

The maximum lateral displacement at the mid-span for the bridge before and after optimization is plotted in Figures 4.2 and 4.3. We can witness that the maximum lateral displacement at the mid-span is sensitive to the wind attacking angle. When the wind blows from the top to bottom which is corresponding to the positive value of skewed angle in Figure 4.2, the maximum lateral displacement will decrease with the increase of the attacking angle. However, if the wind changes the direction which blows from bottom to top with the attacking angle being negative ones in the Figure 4.2, the opposite trend is true, which means the maximum lateral displacement will increase with the increase of the attacking angle. The reason is that the pressure distribution is different. Besides, we can see that the maximum lateral displacement is effectively decreased after optimization. The optimization effectiveness for the wind under different attack angles is illustrated in Figure 4.3. Overall, there is roughly 20% decrease after optimization for different attacking angles.

If we concern about the amplitude of lateral vibration, we can find after optimization, not only the maximum lateral displacement, but also the amplitude of the lateral vibration is more effectively reduced, see Figures 4.4 and 4.5.

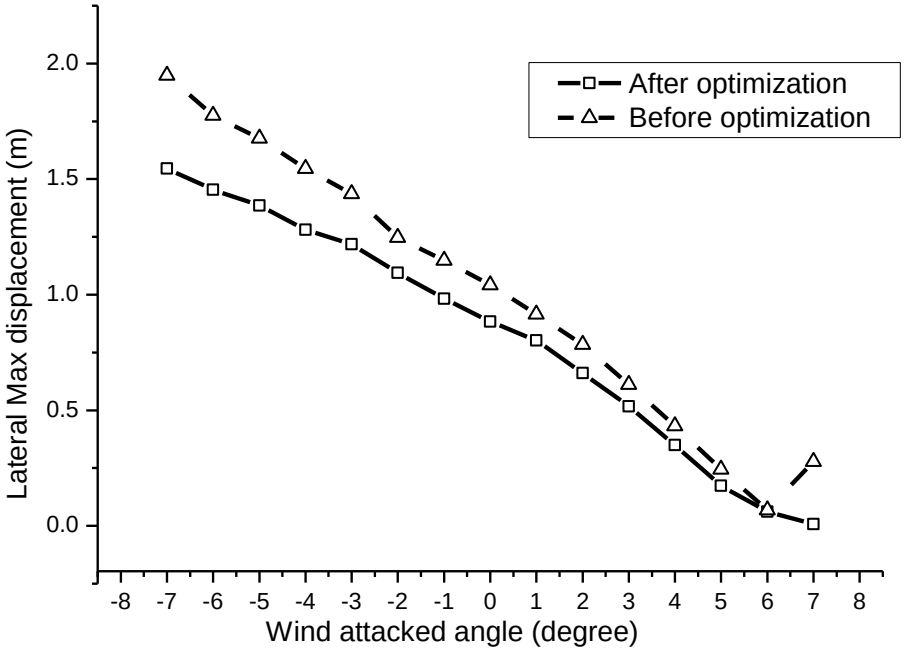

Figure 4.2 Maximum lateral displacement vs. wind attacked angle

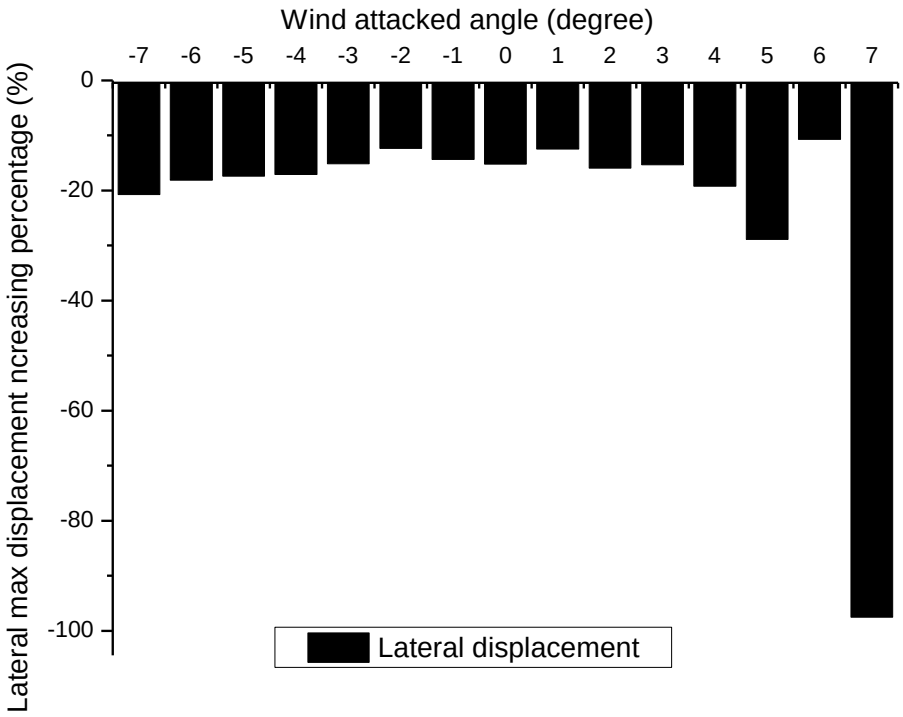

Figure 4.3 Increasing of max lateral displacement vs. wind attacked angle

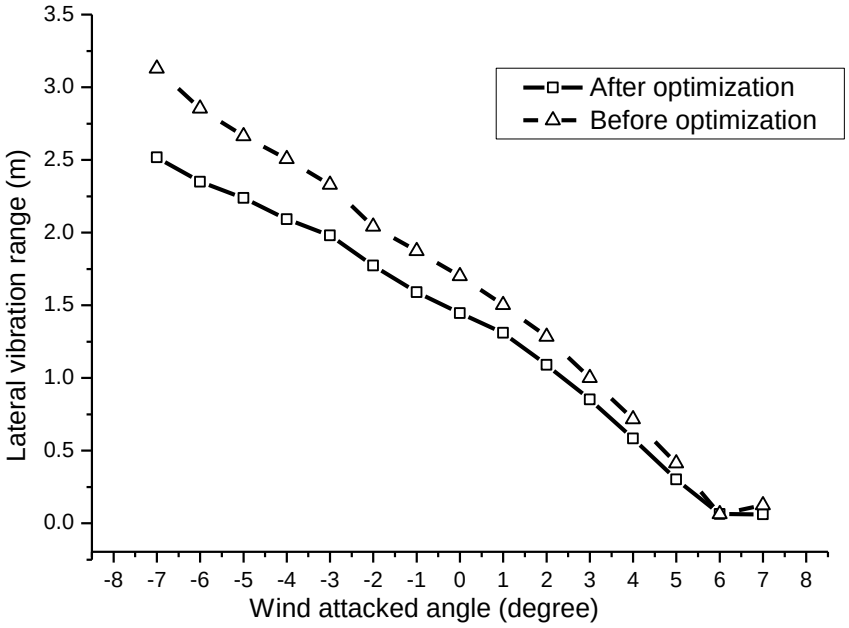

Figure 4.4 Lateral vibration range vs. wind attacked angle

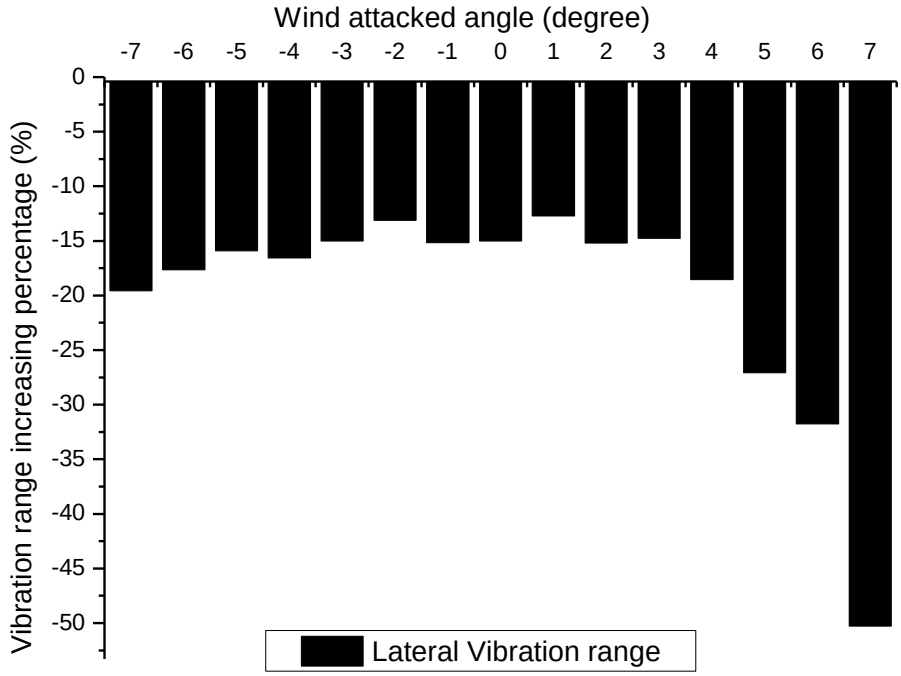

Figure 4.5 Increasing of lateral vibration range vs. wind attacked angle

As to the maximum displacement in the vertical direction, the optimization effect is not so significant compared to the in the lateral direction. The maximum vertical displacement at the

mid-point for the bridge with/without optimization is shown in Figures 4.6 and 4.7. With the variation of the wind attacking angle, the maximum vertical displacement for the optimized bridge nearly coincide with that of the original bridge, except for the one with the wind attacking angle being -7°.

If we concern about the amplitude of vertical vibration, we can find that the optimization has negligible effect on both maximum vertical displacement and amplitude of the vertical displacement, see Figures 4.8 and 4.9.

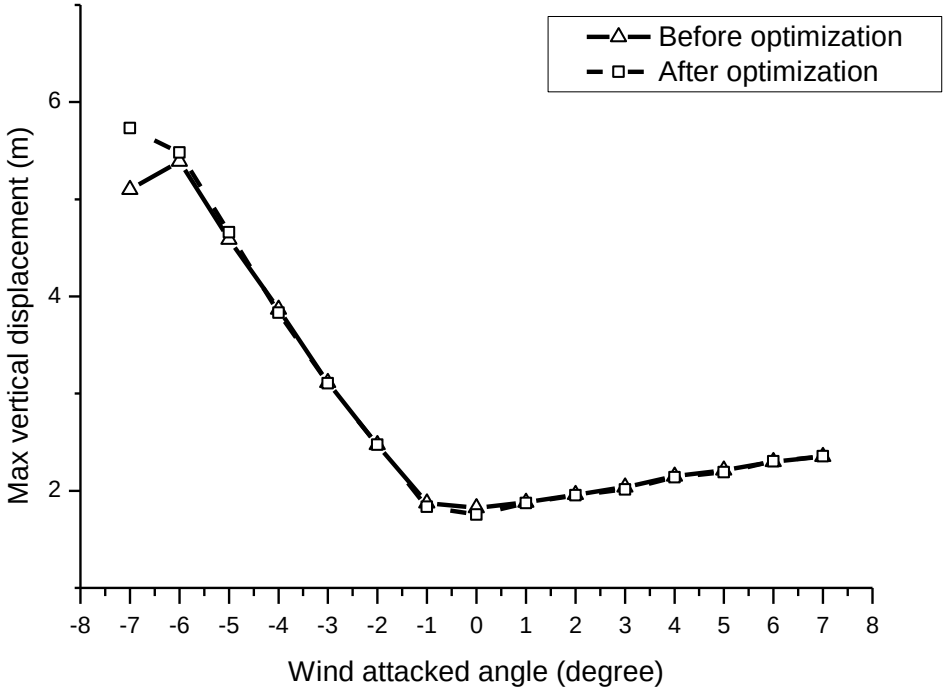

Figure 4.6 Maximum vertical displacement vs. wind attacking angle

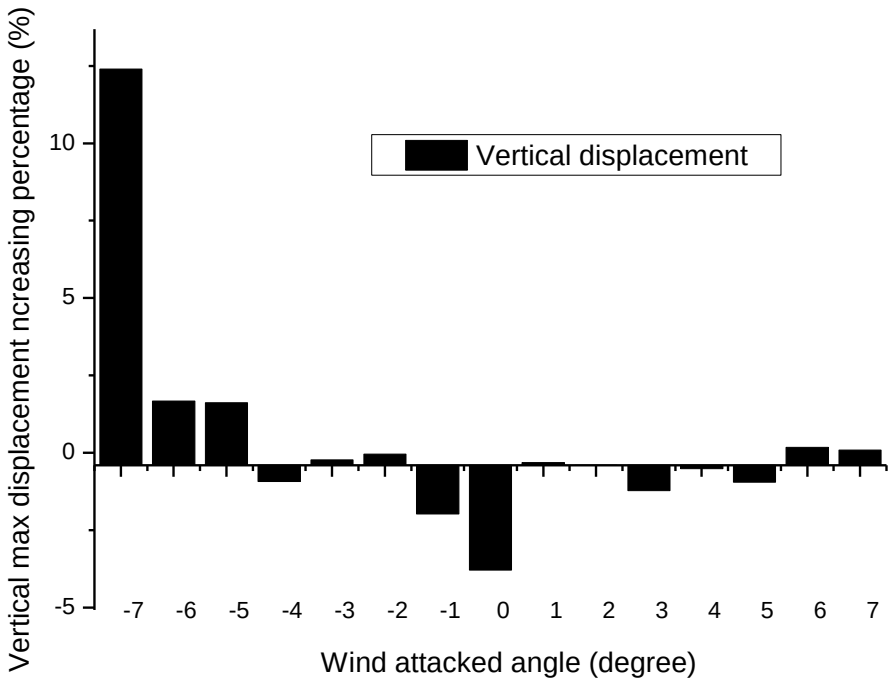

Figure 4.7 Increasing of vertical vibration range vs. wind attacking angle

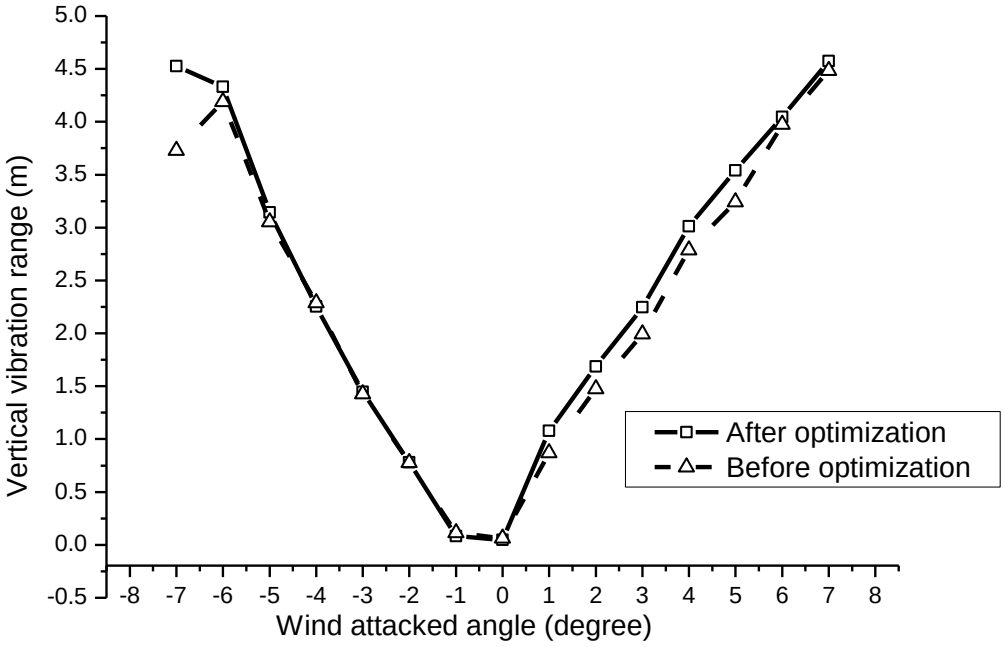

Figure 4.8 Vertical vibration range vs. wind attacking angle

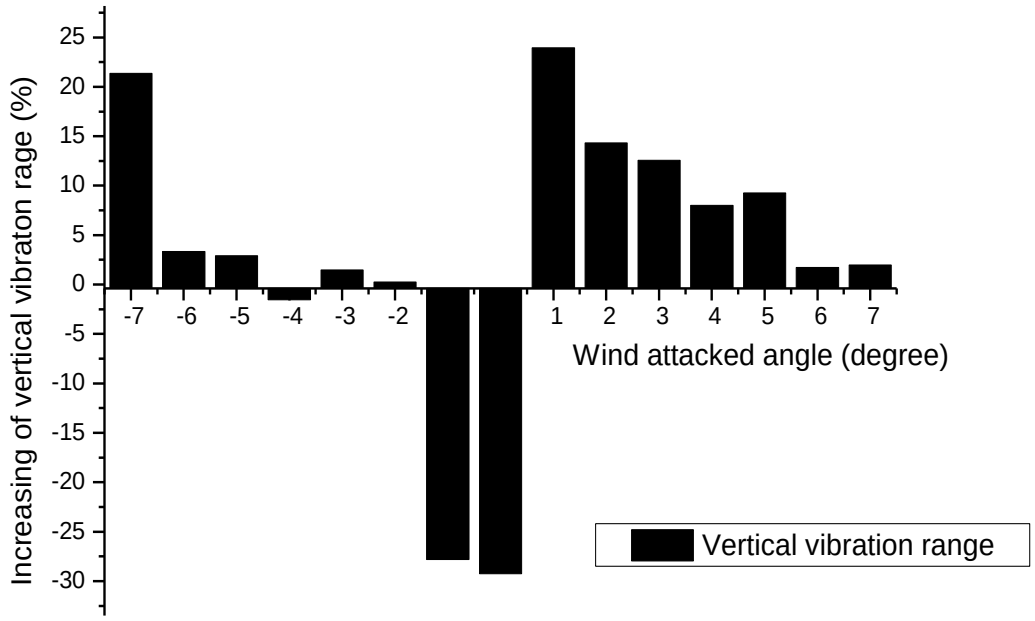

Figure 4.9 Vertical vibration range vs. wind attacking angle

If we look closer into the magnitude of the total displacement which can be decomposed into the lateral and vertical displacements, we can find that the lateral displacement will dominate the total displacement when the wind attacking angle varies from -3 to 3 degree. If the wind attacking angle is out of this range, the vertical displacement will increase significantly and will be much greater than the lateral displacement. From this result, it can be concluded that the vertical vibration becomes the main type of vibration when wind attacking angle is out from -3 to 3 degree and this optimization has little effect on weakening vertical vibration of the bridge. Fortunately, vertical vibration for the bridge under wind load is not the focus in engineering, for most cases. When the wind attacking angle is 0, the dominated displacement is in lateral direction, as shown in Figure 4.10

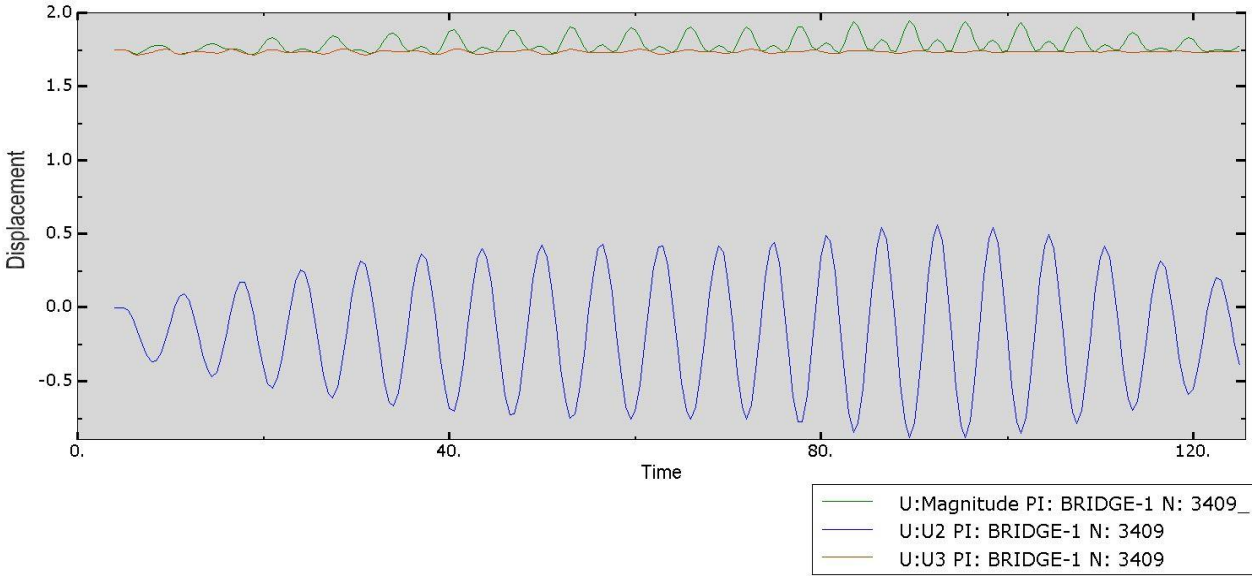

Figure 4.10 Displacement at 0 degree wind attacked angle (U2: lateral, U3: vertical)

4.4 CONCLUSION

Based on the test results, the following conclusions can be obtained:

(1) This optimization has obvious effect in reducing lateral vibration when wind attacking angle varies from -7 to 7 degree. On the other hand, this optimization has little effect in reducing the vertical vibration even if the wind attacking angle is larger.

(2) Through optimization, the aerodynamic stability of the bridge in both vertical and lateral directions is improved, and this is more effective when wind attacking angle is smaller.

(3) This optimization has little effect on reducing vertical vibration.

(4) Suppose that the wind attacking angle is relatively larger and wind speed is higher, the vertical vibration of this thin closed box girder will dominate the dynamic response.

5.0 SUMMARY AND RECOMMENDATIONS OF FUTURE WORKS

5.1 SUMMARY

This research is presented in a series simulation tests to investigate and finally improve the aerodynamic stability of the Tatara Bridge under high speed wind condition. All the analysis of the bridge is based on the numerical simulation and processed in the computer by ABAQUS and SOLIDWORKS software. All the dimensions and the material parameters, like young's modulus and Poisson's ratio, are set according to the real bridge.

In the bridge modal analysis, the first 400 natural frequencies and corresponding modes were calculated by Lanczos method solver of ABAQUS software. The first order mode is found to be the lateral bending of deck in horizontal plane, which gives a guide for further analysis.

In the wind tunnel test simulation, 10 different decks were tested and 15 different initial settings of wind were adopted to simulate the real conditions. All these simulations are realized by SOLIDWORKS FLOW SIMULATION software in the computer, providing the information of aerodynamic forces corresponding to different deck shapes which lays the foundation for further optimization.

The force and moment distributions for the different shape of the transformable special device under various wind attacking angles, which are obtained from the SOLIDWOEKS, are utilized to optimize the dynamic response of the bridge. The lateral and vertical displacement

trends with respect to the wind attacking angles are analyzed and compared. The results can validate that the dynamic response of the bridge under the wind loads can be effectively improved in the lateral direction.

5.2 RECOMMENDATIONS

This research is presented by numerical simulations of dynamics behavior of real bridge, instead of in situ experiments. The results can give some guide for corresponding experimental researches. Meanwhile, the mechanical simplification and the virtual wind tunnel test of girders in 2D instead of 3D save computational cost remarkably. This study can also be improved in several aspects. There are some recommendations for the future studies:

(1) In modal analysis, the simulation of cable can be improved by using more truss elements, which will make the analysis results more accurate, compared to the single truss element.

(2) The shape of the bridge girder can significantly affect the dynamic behavior under wind load. More computational and experimental tests are required to determine the optimized shape, considering the other factors like reducing the overall cost, the easiness of construction, etc.

(3) The location of the transformable device is proved to reduce the lateral displacement of the bridge of the bridge. However, more factors, including the location, the size, etc., should be considered in further study.

(4) As to the larger wind attacking angles, the vertical vibration control needs to be considered for bridge optimization, especially for the thin box girder bridge like the Tatara Bridge.

APPENDIX A

A.1 WIND TUNNEL TEST SIMULATION RECORD

Table 5.1 Records of original deck (Deck 1)

Angle (°)	Force X (N)	Force Y (N)	Total Force (N)	Torque Z (N*m)	Drag Coefficient	Lifting Coefficient	Moment Coefficient
-7	25490.1314	175460.746	177302.623	-1250423.18	0.14438542	0.993873802	-7.082853965
-6	22844.5605	187709.937	189094.935	-1240438.18	0.12939994	1.063257694	-7.026295277
-5	21333.1639	140189	141802.89	-1265624.81	0.12083884	0.794081737	-7.168961558
-4	19698.9787	91430.7028	93528.7292	-1158827.13	0.11158222	0.517896921	-6.564020417
-3	18459.2194	40472.9511	44483.7335	-1027787.61	0.10455977	0.229253589	-5.821764724
-2	16702.1071	4019.8909	17179.0542	-803860.249	0.09460684	0.022770131	-4.553358279
-1	15117.6568	-26968.543	30916.7568	-534496.379	0.08563193	-0.15275968	-3.027582864
0	14326.0288	-28186.771	31618.4937	-449083.819	0.08114786	-0.15966017	-2.543774901
1	12437.1748	-73113.478	74163.7646	-151306.393	0.0704487	-0.41414146	-0.857054716
2	10640.6994	-105656.87	106191.333	25865.4392	0.06027281	-0.59847915	0.146511302
3	8271.30243	-129984.27	130247.165	231157.6723	0.04685168	-0.7362784	1.30936155
4	5688.98923	-173447.72	173540.991	436130.1023	0.03222451	-0.98247128	2.470400316
5	2895.24021	-192330.02	192351.814	680487.723	0.0163997	-1.08942755	3.854531199
6	-1570.6398	-240924.7	240929.821	840492.6335	-0.00889668	-1.36468557	4.760857497
7	-4744.6676	-268779.82	268821.696	1052427.907	-0.02687553	-1.52246715	5.961336353

Table 5.2 Records of Deck 3

Angle (°)	Force X (N)	Force Y (N)	Total Force (N)	Torque Z (N*m)	Drag Coefficient	Lifting Coefficient	Moment Coefficient
-7	16836.1406	79660.906	81420.6091	-2593167.82	0.08300167	0.392725877	-12.78423956
-6	13775.9999	30360.4806	33339.7203	-2220322.66	0.06791527	0.149676258	-10.94612408
-5	11216.8227	10160.6799	15134.6136	-1890256.16	0.0552986	0.050091847	-9.318906131
-4	9672.83557	-10658.688	14393.4495	-1518299.31	0.04768679	-0.05254701	-7.485170025
-3	8526.73683	-52093.918	52787.1346	-1180135.16	0.04203656	-0.25682145	-5.818030911
-2	7350.00876	-73895.103	74259.7392	-869266.817	0.03623532	-0.36430064	-4.285459324
-1	5527.19094	-80231.796	80421.9557	-539512.243	0.02724889	-0.39554035	-2.659779171
0	5418.24553	-58614.782	58864.6758	-529361.762	0.02671179	-0.28896912	-2.780982849
1	4614.2567	-120885.79	120973.826	-80141.5788	0.02274815	-0.59596334	-0.395095579
2	3340.10652	-148209.33	148246.962	207865.0206	0.01646662	-0.73066755	1.024768315
3	2036.43459	-174569.24	174581.122	510154.4878	0.01003956	-0.86062113	2.515046317
4	-85.685946	-213763.06	213763.075	813132.7501	-0.00042243	-1.05384546	4.00872006
5	-2249.7908	-250832.66	250842.752	1125348.424	-0.0110914	-1.2365975	5.547933965
6	-4733.0745	-288222.84	288261.7	1444072.601	-0.02333392	-1.42092996	7.119234593
7	-7910.6652	-327097.6	327193.239	1807504.211	-0.03899934	-1.61258133	8.910941524

Table 5.3 Records of Deck4

Angle (°)	Force X (N)	Force Y (N)	Total Force (N)	Torque Z (N*m)	Drag Coefficient	Lifting Coefficient	Moment Coefficient
-7	-1038.6693	197076.097	197078.834	-2083378	-0.00487593	0.925154904	-9.780218955
-6	1172.9709	152600.162	152604.67	-1752071.32	0.0055064	0.716366877	-8.224931364
-5	2755.22048	118202.92	118235.027	-1431092.45	0.01293412	0.554892313	-6.718126735
-4	3582.88523	86669.9946	86744.0202	-1113600.67	0.01681951	0.406864008	-5.227691925
-3	4595.43731	54117.4488	54312.2114	-805961.865	0.02157284	0.254049192	-3.783510961
-2	4850.21653	23484.8536	23980.4702	-517431.998	0.02276888	0.110247401	-2.429035068
-1	5283.77113	-14854.097	15765.8626	-226479.651	0.02480416	-0.06973114	-1.063187079
0	4116.96917	-4933.197	6425.40801	3652.348399	0.01932672	-0.02315842	0.016807453
1	5589.46497	-46200.637	46537.5219	210621.8561	0.02623921	-0.21688447	0.988744177
2	5422.11281	-75010.518	75206.2302	539575.4378	0.02545359	-0.35212971	2.532985332
3	5175.55572	-99431.759	99566.3654	873128.4882	0.02429615	-0.46677289	4.098818253
4	4706.32059	-127172.53	127259.587	1235012.262	0.02209337	-0.5969993	5.797647048
5	4382.16484	-112503.78	112589.088	1619948.218	0.02057165	-0.52813822	7.604692108
6	3799.86002	-139724.45	139776.114	2018998.499	0.01783808	-0.6559231	9.477995521
7	3616.187	-160801.01	160841.662	2399024.601	0.01697584	-0.75486496	11.26199174

Table 5.4 Records of Deck 6

Angle (°)	Force X (N)	Force Y (N)	Total Force (N)	Torque Z (N*m)	Drag Coefficient	Lifting Coefficient	Moment Coefficient
-7	-3216.9425	233709.18	233731.319	-1938991.34	-0.01480379	1.075487797	-8.922890945
-6	169.882761	192550.132	192550.207	-1595533.41	0.00078177	0.886081231	-7.342359063
-5	1985.24861	154548.629	154561.379	-1298061.19	0.00913576	0.711205116	-5.973445173
-4	3751.66302	116503.007	116563.397	-982099.832	0.01726448	0.536125975	-4.519447573
-3	5541.27868	77438.4921	77636.498	-690466.93	0.02549997	0.356358074	-3.177405176
-2	6280.41023	42269.0647	42733.0947	-402222.13	0.02890132	0.194514667	-1.850954221
-1	6993.61209	4285.08389	8201.98476	-109394.876	0.03218335	0.019719189	-0.503415632
0	6128.3302	4302.05414	7487.59646	159164.9396	0.02820148	0.019797283	0.732448552
1	8203.6577	-25030.833	26340.8925	377283.3643	0.03775176	-0.11518741	1.736190486
2	8332.99685	-55886.966	56504.7949	676058.8991	0.03834696	-0.25718181	3.111101997
3	9219.47846	-90440.318	90909.0195	1019650.137	0.04242639	-0.41619015	4.692247351
4	9813.15759	-125545.45	125928.389	1382309.826	0.04515839	-0.5777377	6.3611423
5	9116.52507	-143133.76	143423.79	1730421.044	0.04195262	-0.65867592	7.963087793
6	9530.49034	-168999.69	169268.207	2153494.269	0.04385761	-0.77770632	9.909995018
7	9687.57684	-190605.39	190851.417	2551334.929	0.04458049	-0.87713187	11.7407865

A.2 WIND EFFECT TEST RESULT RECORD

Table 5.5 Midspan displacement before optimization

Angle (°)	Midspan displacement **before** optimization (m)					
	Lateral		Vertical		Magnitude	
	Range	Max	Range	Max	Range	Max
-7	3.129	-1.949	3.73	5.1	3.73	5.1
-6	2.853	-1.776	4.19	5.39	4.17	5.39
-5	2.663	-1.676	3.054	4.586	3.022	4.612
-4	2.5072	-1.545	2.288	3.867	2.174	3.8
-3	2.331	-1.436	1.426	3.114	1.44	3.141
-2	2.042	-1.248	0.777	2.474	0.852	2.598
-1	1.874	-1.148	0.115	1.872	0.362	2.168
0	1.7016	-1.042	0.065	1.824	0.298	2.087
1	1.5022	-0.9159	0.871	1.88	0.695	1.922
2	1.285	-0.7853	1.4752	1.962	1.4445	1.98
3	1.0006	-0.611	1.9947	2.038	1.8701	2.048
4	0.7172	-0.432	2.789	2.149	2.0347	2.153
5	0.4143	-0.2444	3.241	2.213	2.1961	2.214
6	0.0951	0.069	3.977	2.299	1.9836	2.299
7	0.1245	0.2781	4.485	2.353	2.2821	2.356

Table 5.6 Midspan displacement after optimization

Angle (°)	Midspan displacement **after** optimization (m)					
	Lateral		Vertical		Magnitude	
	Range	Max	Range	Max	Range	Max
-7	2.5168	-1.545	4.527	5.732	4.553	5.773
-6	2.3493	-1.454	4.33	5.48	4.394	5.56
-5	2.239	-1.385	3.143	4.66	3.153	4.68
-4	2.092	-1.281	2.253	3.831	2.239	3.85
-3	1.9813	-1.219	1.447	3.107	1.439	3.127
-2	1.774	-1.094	0.779	2.473	0.775	2.513
-1	1.59	-0.983	0.083	1.835	0.274	2.062
0	1.4462	-0.8836	0.046	1.755	0.205	1.946
1	1.3112	-0.8016	1.0794	1.874	1.0674	1.894
2	1.0897	-0.6604	1.6865	1.954	1.6378	1.966
3	0.8529	-0.5172	2.2452	2.013	1.8379	2.038
4	0.5842	-0.3491	3.0124	2.138	2.0718	2.141
5	0.3021	-0.1738	3.541	2.192	1.803	2.193
6	0.0649	-0.0616	4.045	2.303	2.0268	2.303
7	0.0619	0.0069	4.574	2.355	2.3308	2.355

Table 5.7 Midspan displacement increasing after optimization

	Midspan displacement increase **after** optimization (m)					
Angle (°)	Lateral		Vertical		Magnitude	
	Range	Max	Range	Max	Range	Max
-7	-19.5653563	-20.72857876	21.36729	12.39216	4.553	13.19608
-6	-17.6550999	-18.13063063	3.341289	1.669759	4.394	3.153989
-5	-15.9218926	-17.3627685	2.914211	1.613607	3.153	1.474415
-4	-16.5603063	-17.08737864	-1.52972	-0.93095	2.239	1.315789
-3	-15.002145	-15.11142061	1.472651	-0.22479	1.439	-0.44572
-2	-13.1243879	-12.33974359	0.2574	-0.04042	0.775	-3.27175
-1	-15.1547492	-14.3728223	-27.8261	-1.9765	0.274	-4.8893
0	-15.0094029	-15.20153551	-29.2308	-3.78289	0.205	-6.75611
1	-12.7146851	-12.47952833	23.92652	-0.31915	1.0674	-1.45682
2	-15.1984436	-15.90474978	14.32348	-0.40775	1.6378	-0.70707
3	-14.7611433	-15.35188216	12.55828	-1.22669	1.8379	-0.48828
4	-18.5443391	-19.18981481	8.010039	-0.51187	2.0718	-0.55736
5	-27.0818248	-28.88707038	9.256402	-0.94894	1.803	-0.94851
6	-31.7560463	-10.72463768	1.709832	0.173989	2.0268	0.173989
7	-50.2811245	-97.5188781	1.984392	0.084998	2.3308	-0.04244

APPENDIX B

WIND EFFECT TEST FIGURES

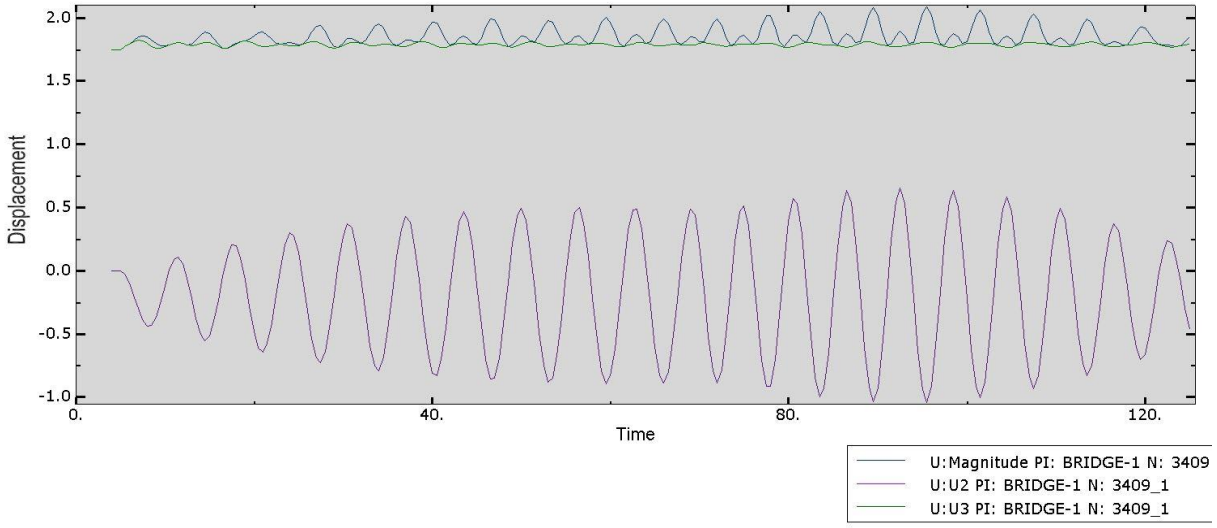

Figure 5.1 Displacement of Deck1 at 0 degree

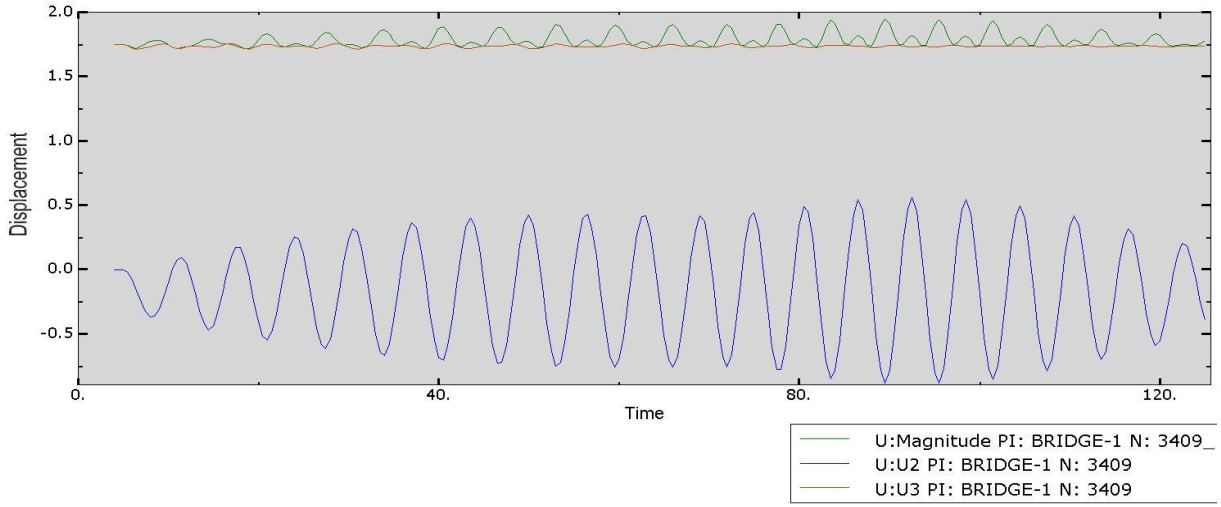

Figure 5.2 Displacement of optimized deck at 0 degree

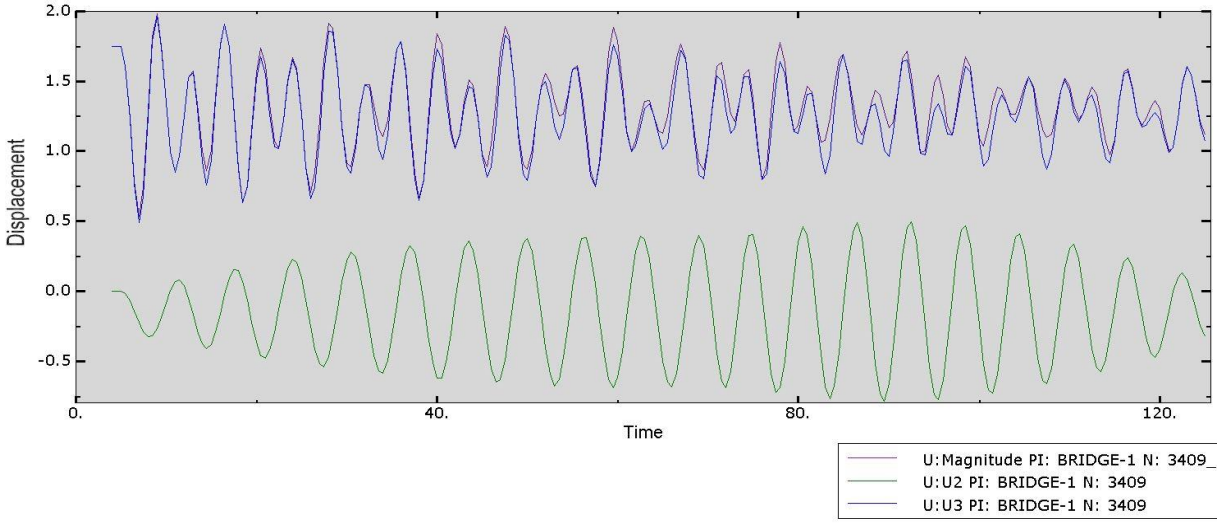

Figure 5.3 Displacement of Deck1 at 2 degree

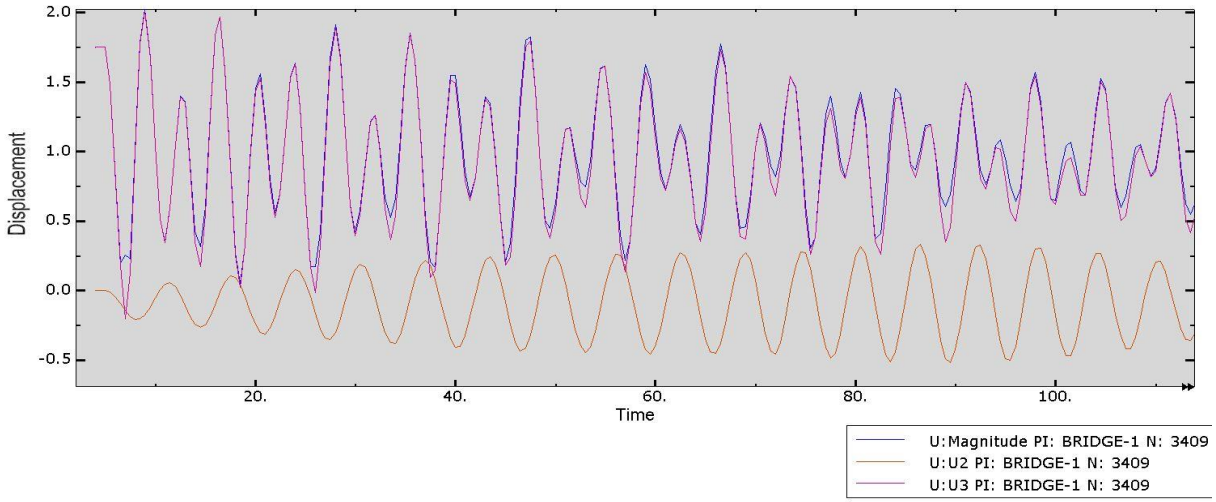

Figure 5.4 Displacement of optimized deck at 3 degree

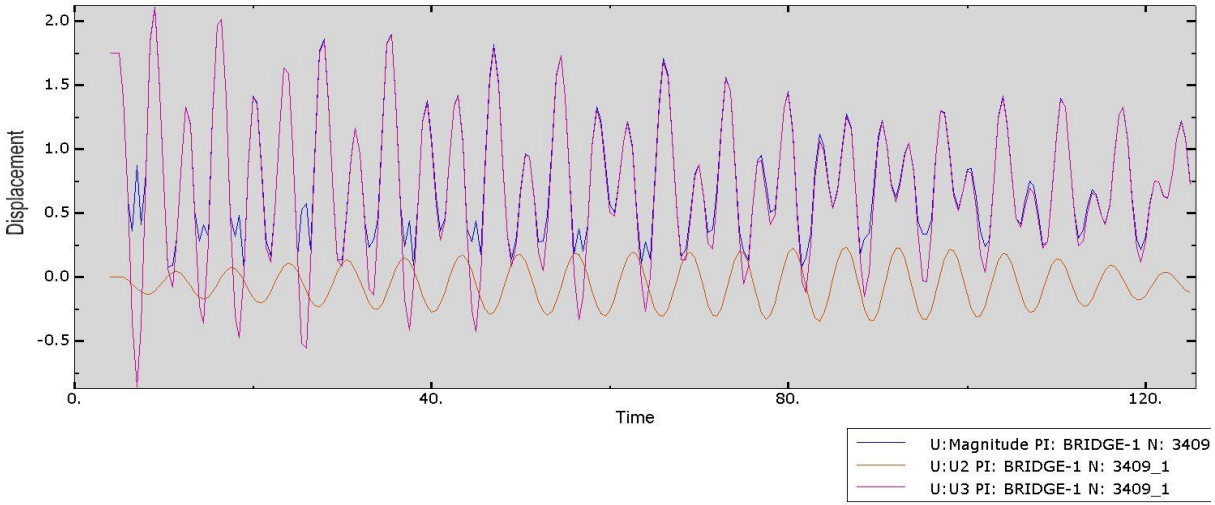

Figure 5.5 Displacement of optimized deck at 4 degree

BIBLIOGRAPHY

Authority, H. S. B. (1999). The Tatara Bridge: design and construction technology for the world's longest cable-stayed bridge. *Tokyo: Honshu-Shikoku Bridge Authority*.

Banks, J., Carson, J. S., & Nelson, B. L. (2000). *DM Nicol, Discrete-Event System Simulation*. Englewood Cliffs, NJ, USA: Prentice hall.

Billah, K. Y., & Scanlan, R. H. (1991). Resonance, Tacoma Narrows bridge failure, and undergraduate physics textbooks. *Am. J. Phys*, *59*(2), 118-124.

Branceleoni, F. (1992). ‘‘The construction phase and its aerodynamic issues.’’ *Aerodynamics of large bridges*, A. Larsen, ed., Balkema, Rotterdam, The Netherlands, 147–158.

Bratley, P., Fox, B. L., & Schrage, L. E. (1983). *A guide to simulation* (Vol. 2). New York: Springer-Verlag.

Ciobaca, V., Melber-Wilkending, S., & Pott-Pollenske, M. A CFD PROCESS CHAIN FOR SIMULATING OPEN WINDTUNNEL TEST SECTIONS.

Clemente, P., Marulo, F., Lecce, L., & Bifulco, A. (1998). Experimental modal analysis of the Garigliano cable-stayed bridge. *Soil dynamics and earthquake engineering*, *17*(7), 485-493.

Clough, R. W., & Penzien, J. (1975). *Dynamics of structures* (No. Monograph).

Company Info SolidWorks. (n.d.). Retrieved March 18 2015, from http://www.solidworks.com/sw/183_ENU_HTML.htm

Cunha, A., Caetano, E., & Delgado, R. (2001). Dynamic tests on large cable-stayed bridge. *Journal of Bridge Engineering*, *6*(1), 54-62.

Datta, T. K., & Pourzeynali, S. (2002). Control of flutter of suspension bridge deck using TMD. *WIND STRUCT INT J.*, *5*(5), 407-422.

Deger, Y., Cantieni, R., & Pietrzko, S. (1994). Modal analysis of an arch bridge: experiment, finite element analysis and link. In *PROCEEDINGS-SPIE THE INTERNATIONAL SOCIETY FOR OPTICAL ENGINEERING* (pp. 425-425). SPIE INTERNATIONAL SOCIETY FOR OPTICAL.

Deger, Y., Cantieni, R. O., Pietrzko, S., Ruecker, W., & Rohrmann, R. (1995, February). Modal analysis of a highway bridge: experiment, finite element analysis and link.

In *PROCEEDINGS-SPIE THE INTERNATIONAL SOCIETY FOR OPTICAL ENGINEERING* (pp. 1141-1141). SPIE INTERNATIONAL SOCIETY FOR OPTICAL.

Fan, L.C. (1997). *Seismic Prevention for Bridge*. Shanghai: Tongji University Press, 1997:117-154

Fujino, Y. (2002). Vibration, control and monitoring of long-span bridges—recent research, developments and practice in Japan. *Journal of Constructional Steel Research*, *58*(1), 71-97.

Gu, M., Chen, S. R., & Chang, C. C. (2001). Parametric study on multiple tuned mass dampers for buffeting control of Yangpu Bridge. *Journal of Wind Engineering and Industrial Aerodynamics*, *89*(11), 987-1000.

Hansen, H. I., & Thoft-Christensen, P. (1998). *Active control of long bridges using flaps*. Dept. of Building Technology and Structural Engineering.

Hansen, H. I., & Thoft-Christensen, P. (2001). Active flap control of long suspension bridges. *Journal of Structural Control*, *8*(1), 33-82.

Huynh, T., & Thoft-Christensen, P. (2001). Suspension bridge flutter for girders with separate control flaps. *Journal of Bridge Engineering*, *6*(3), 168-175.

Ishak, I. S. (2006). Computational fluid dynamics simulation and wind tunnel testing on microlight model.

Kobayashi, H., & Nagaoka, H. (1992). Active control of flutter of a suspension bridge. *Journal of Wind Engineering and Industrial Aerodynamics*, *41*(1), 143-151.

Kobayashi, H., Ogawa, R., and Taniguchi, S. (1998). ‘‘Active flutter control of a bridge deck by ailerons.’’ Proc., *2nd World Conf. on Struct. Control*, T. Kobori et al., eds., Kyoto, Japan, 3, 1841–1848.

Kwon, S. D., & Park, K. S. (2004). Suppression of bridge flutter using tuned mass dampers based on robust performance design. *Journal of wind engineering and industrial aerodynamics*, *92*(11), 919-934.

Nobuto, J., Fujino, Y., and Ito, M. (1988). ‘‘A study on the effectiveness of TMD to suppress a coupled flutter of bridge deck.’’ *J. Struct. Mech. and Earthquake Engrg*., Tokyo, 398(10), 413–416 (in Japanese).

Ostenfeld, K., and Larsen, A. (1992). ‘‘Bridge engineering and aerodynamics.’’ *Aerodynamics of large bridges*, A. Larsen, ed., Balkema, Rotterdam, The Netherlands, 3–22.

Pedrammehr, S., Farrokhi, H., Rajab, A., Pakzad, S., Mahboubkhah, M., Ettefagh, M. M., & Sadeghi, M. H. (2012, February). Modal analysis of the milling machine structure through FEM and experimental test. In *Advanced Materials Research* (Vol. 383, pp. 6717-6721).

Ramsey, K. (1983). Experimental modal analysis, structural modifications and FEM analysis on a desktop computer. *SOUND AND VIBRAT.*, *17*(2), 19-27.

Reddy, J. N., & Gartling, D. K. (2010). *The finite element method in heat transfer and fluid dynamics*. CRC press.

Ren, W. X., Zhao, T., & Harik, I. E. (2004). Experimental and analytical modal analysis of steel arch bridge. *Journal of Structural Engineering*, *130*(7), 1022-1031.

Thoft-Christensen, P. (2000). *Active control of suspension bridges*. Dept. of Building Technology and Structural Engineering.

Wang, H., Hu, R., Xie, J., Tong, T., & Li, A. (2012). Comparative study on buffeting performance of Sutong Bridge based on design and measured spectrum. *Journal of Bridge Engineering*, *18*(7), 587-600.

Wei, L., Cheng, H., & Li, J. (2012). Modal analysis of a cable-stayed bridge.*Procedia engineering*, *31*, 481-486.

Wikipedia, Roman bridge. (n.d). Retrieved November 9th, 2014, from http://en.wikipedia.org/wiki/Roman_bridge

Wikipedia, Russky Bridge. (n.d). Retrieved January 4th, 2015, from http://en.wikipedia.org/wiki/Russky_Bridge#cite_ref-6

Wikipedia, Akashi Kaikyō Bridge. (n.d). Retrieved March 18th, 2015, from http://en.wikipedia.org/wiki/Akashi_Kaiky%C5%8D_Bridge

Wikipedia, List of Longest Bridges in the world. Retrieved March 4th, 2015, from http://en.wikipedia.org/wiki/List_of_longest_bridges_in_the_world

Wilde, K., Omenzetter, P., & Fujino, Y. (2001). Suppression of bridge flutter by active deck-flaps control system. *Journal of engineering mechanics*, *127*(1), 80-89.

Wilson, A. (2009). A critical analysis of Tatara Bridge, Japan. In *Proceedings of Bridge Engineering Conference*.

Xu, Y. L., Ko, J. M., & Zhang, W. S. (1997). Vibration studies of Tsing Ma suspension bridge. *Journal of Bridge Engineering*, *2*(4), 149-156.

Xu, Y. L. (2013). *Wind effects on cable-supported bridges*. John Wiley & Sons

Yabuno, M., Fujiwara, T., Sumi, K., Nose, T., & Suzuki, M. (2003). Design of Tatara bridge. *IHI engineering review*, *36*(2), 40-56.

Zhang, Y. L., Xu, C., Chen, X. C., & Xia, X. S. (2011). The Influence of Traveling Wave Effect on Seismic Response of Railway Cable-stayed Bridge.*Journal of Lanzhou Jiaotong University*, *1*, 017.